INFN/AExxx, LAL-xxx, SLAC-R-xxx

Super$B$ Detector Technical Design Report

Abstract

This report describes the technical design detector for Super$B$.

Contents

1 Introduction **1**
- 1.1 The Physics Motivation . . . 1
- 1.2 The Super$B$ Project Elements . . . 1
- 1.3 The Detector Technical Design Report . . . 2

2 Accelerator Overview **7**

3 Detector Overview **9**
- 3.1 Physics Performance . . . 9
- 3.2 Challenges on Detector Design . . . 12
- 3.3 Open Issues . . . 14
- 3.4 Detector R&D . . . 14

4 Physics with SuperB **19**
- 4.1 Introduction . . . 19
- 4.2 B and D decays . . . 19
  - 4.2.1 Rare B decays . . . 19
  - 4.2.2 Rare D decays . . . 21
  - 4.2.3 CKM matrix and unitarity triangle . . . 22
  - 4.2.4 CP violation in B decays . . . 23
  - 4.2.5 CP violation in D decays . . . 23
  - 4.2.6 Other symmetry tests . . . 24
  - 4.2.7 Charm mixing . . . 24
  - 4.2.8 B physics at the $\Upsilon(5S)$ . . . 25
- 4.3 τ physics at Super$B$ . . . 26
  - 4.3.1 Lepton flavor violation in τ decay . . . 26
  - 4.3.2 CP violation in τ decay . . . 27
  - 4.3.3 Measurement of the τ $g-2$ and EDM form factors . . . 27
- 4.4 Super$B$ Neutral Current Electroweak Physics Programme . . . 28
- 4.5 Exotic Spectroscopy in Super$B$ . . . 29
- 4.6 Direct searches . . . 31
- 4.7 Executive Summary . . . 31

5 Machine Detector Interface and Backgrounds **37**
- 5.1 Overview M.Sullivan, M. Boscolo E.Paoloni, - 1 page . . . 37
- 5.2 Backgrounds sources. M.Sullivan, M.Boscolo, E.Paoloni, - 2 pages . . . 37
- 5.3 Radiative Bhabha . . . 37
  - 5.3.1 Simulation tools . . . 37
  - 5.3.2 Losses at the beam-pipe . . . 38
  - 5.3.3 Shield System . . . 39
- 5.4 Pairs Production C.Rimbault - 2 pages . . . 40

5.5 Touscheck bacgkround. M.Boscolo - 2 pages 40
5.6 Beam gas background. M.Boscolo - 2 pages 40
5.7 Synchrotron radiation background. M.Sullivan - 2 pages 40
5.8 SVT background overview 40
5.9 DCH background overview R.Cenci D.Lindemann - 2 pages 42
5.10 FTOF background overview L.Burmistrov - 2 pages 42
5.11 FDIRC background overview 42
5.11.1 Shielding the FDIRC 43
5.11.2 Background rates in the FDIRC 43
5.11.3 Integrated charges and doses 43
5.12 EMC background overview. S.Germani - 2 pages 43
5.13 IFR background overview V.Santoro - 2 pages 45
5.14 ETD background overview R.Cenci - 2 pages 45
5.15 SVT radiation monitor. A.Di Ciaccio- 3 pages 45
5.16 Quick demounting. M.Sullivan, F.Bosi, E.Paoloni - 4 pages 45

6 Silicon Vertex Tracker 49
6.1 Overview G.Rizzo - 12 pages 49
6.1.1 SVT and Layer0 49
6.2 SVT Requirements 51
6.2.1 Resolution 51
6.2.2 Acceptance 51
6.2.3 Efficiency 53
6.2.4 Background & Radiation Tolerance 53
6.2.5 Reliability 54
6.3 Baseline Detector Concept 54
6.3.1 Technology 54
6.3.2 Layout 54
6.3.3 Electronic Readout 58
6.3.4 Module design and Mechanical Support 58
6.4 Layer0 Pixel Upgrade 59
6.4.1 Motivations 59
6.4.1.1 Technology Options for Layer0 pixel upgrade 61
6.4.1.2 Pixel Module & Material Budget 62
6.5 R&D Main Activities 63
6.6 Backgrounds R.Cenci - 4 pages 63
6.6.1 Pair production 64
6.6.2 Radiative Bhabha 64
6.6.3 Touschek 64
6.6.4 Beam Gas 64
6.6.5 Other sources 64
6.7 Detector Performance Studies N.Neri - 6 pages 64
6.7.1 Introduction 64
6.7.2 The SVT layout 65
6.7.3 Impact of Layer0 on detector performance 65
6.7.4 Tracking performance 68
6.7.5 Impact of machine background on tracking performance 69

6.7.6 Sensitivity studies for time-dependent analyses 70
6.7.7 Performance with Layer0 pixel detectors 71
6.7.8 Particle identification with dE/dx 72
6.8 Silicon Sensors L. Bosisio - 8 pages 72
6.8.1 Requirements 73
6.8.2 Sensor design and technology 73
6.8.3 Wafer layout and quantities 76
6.8.4 Prototyping and tests 76
6.8.5 z-side strip connection options 76
6.9 Fanout Circuits L.Vitale - M.Prest2+2 pages 77
6.9.1 Fanouts for layer0 78
6.9.1.1 Requirements 78
6.9.1.2 Technology 78
6.9.1.3 Design 78
6.9.1.4 Prototyping and tests 78
6.9.2 Fanouts for outer layers 78
6.9.2.1 Requirements 78
6.9.2.2 Material and production technique 78
6.9.2.3 Design 78
6.9.2.4 Tests and prototyping 78
6.10 Electronics Readout 28 pages 80
6.10.1 Readout chips V.Re - 10 80
6.10.1.1 Electronic Readout for Strip and Striplet Detectors 80
6.10.2 Readout chips requirements 80
6.10.3 Readout Chip Implementation 83
6.10.4 R&D for strip readout chips 85
6.10.5 Hybrid Design M.Citterio - 10 85
6.10.6 Data Transmission M.Citterio - 10 85
6.10.7 Power Supply - 2 85
6.11 Mechanical Support and Assembly S.Bettarini/F.Bosi - 14 pages 85
6.11.1 I.R. Constraint 85
6.11.2 Module Assembly 87
6.11.3 Detector Assembly and Installation 88
6.11.3.1 SVT Half Detector Assembly 88
6.11.3.2 Mount L0 on the Be-pipe and L 1-5 on the W Shielding 89
6.11.3.3 Installation of Complete Assembly into the SuperB Detector 89
6.11.3.4 Quick Demounting 89
6.11.4 Detector Placement and Survey 91
6.11.4.1 Placement accuracy 91
6.11.4.2 Survey with tracks 91
6.11.5 Detector Monitoring 91
6.11.5.1 Position Monitoring System 91
6.11.5.2 Radiation Monitoring 91
6.11.6 R&D Program 91
6.11.6.1 Cables 91
6.11.6.2 hybrid 91
6.11.6.3 Inner layer sextant 91

6.11.6.4 Arch modules . . . 91
6.11.6.5 Cones and space frame . . . 91
6.11.6.6 Full-scale model of IR . . . 91
6.12 Layer0 Upgrade Options G.Rizzo/L.Ratti - 10 pages . . . 91
6.12.1 Technology options . . . 91
6.12.1.1 Hybrid pixels . . . 91
6.12.1.2 Deep N-well CMOS monolithic sensors . . . 93
6.12.1.3 Monolithic pixels in CMOS quadruple well technology . . . 94
6.12.2 Overview of the R&D activity . . . 95
6.12.2.1 Front-end electronics for hybrid pixels in planar and 3D CMOS technology . . . 95
6.12.2.2 The Apsel DNW MAPS series . . . 96
6.12.2.3 The Apsel4well quadruple well monolithic sensor . . . 100
6.12.3 Radiation tolerance . . . 101
6.13 Services, Utilities and E.S. & H issues - 4 pages . . . 104
6.13.1 Service and Utilities . . . 104
6.13.2 ES&H Issue . . . 104

7 Drift Chamber 49 pages **109**
7.1 Overview - Finocchiaro, Roney 10 pages . . . 109
7.1.1 Physics Requirements - 3 pages . . . 109
7.1.2 Geometrical Constraints . . . 109
7.1.3 Machine Background Considerations - Cenci 3 pages . . . 109
7.1.4 DCH Design Overview - 2 pages . . . 109
7.1.5 Expected Performance - 2 pages . . . 109
7.2 Design Optimization - Finocchiaro, Hearty, Piccolo, Roney 9 pages . . . 110
7.2.1 Cluster Counting . . . 110
7.2.2 Cell Design and Layer Arrangement . . . 110
7.2.3 Gas Mixture . . . 112
7.2.4 R&D and Prototype Studies . . . 113
7.2.4.1 Prototype 1 . . . 113
7.2.4.2 Prototype 2 . . . 113
7.2.4.3 Single Cell Prototype(s) . . . 117
7.2.4.4 Aging studies: fields, gas gain . . . 117
7.2.5 R&D Future Developments . . . 117
7.3 Mechanical Design . . . 117
7.3.1 Endplates . . . 118
7.3.2 Inner cylinder . . . 118
7.3.3 Outer Cylinder . . . 118
7.3.4 Choice of wire and electrostatic stability . . . 119
7.3.5 Feed-through design . . . 119
7.3.6 Endplate system . . . 119
7.3.6.1 Supports for on-detector boards . . . 119
7.3.6.2 Cooling . . . 119
7.3.6.3 Shielding . . . 119
7.3.7 Stringing . . . 119

7.4 Electronics - Felici, Martin 1 page 119
7.4.1 Design Goals 119
7.4.2 Standard Readout - charge measurements specifications 119
7.4.2.1 Resolution 119
7.4.2.2 Dynamic range 119
7.4.2.3 Linearity 119
7.4.3 Standard Readout - time measurements specifications 119
7.4.3.1 Resolution 120
7.4.3.2 Dynamic Range 121
7.4.3.3 Linearity 121
7.4.4 Standard Readout - DCH Front-end system (block diagram) 121
7.4.5 Standard Readout - ON-DETECTOR electronics 121
7.4.5.1 Very Front End Boards 121
7.4.6 Sampled Waveforms - specifications 121
7.4.6.1 Resolution 122
7.4.6.2 Dynamic range 122
7.4.6.3 Linearity 123
7.4.7 Sampled Waveforms - DCH front-end system (block diagram) 123
7.4.8 Sampled Waveforms - ON DETECTOR electronics 123
7.4.8.1 Very Front End Boards 123
7.4.9 Grounding 123
7.5 High Voltage system - Martin 1 page 123
7.5.1 HV distribution boards - Standard ReadOut 123
7.5.2 HV distribution boards - Sampled Waveforms 123
7.6 Gas system - Roney 2 pages 123
7.7 Calibration and monitoring - Roney 3 pages 124
7.7.0.1 Slow control systems 124
7.7.0.2 Calibration 124
7.7.0.3 Gas monitoring system 124
7.7.0.4 On-line monitor 124
7.8 Integration - Hearty, Lauciani 6 pages 124
7.8.1 Overall geometry and mechanical support 124
7.8.2 Cable supports and routing 124
7.8.3 Access 124
7.8.4 Gas system 124
7.8.5 Off-detector electronics crates 124
7.8.6 High voltage crates 124
7.8.7 Installation and alignment 124

8 Particle Identification 127
8.1 Summary of Physics Requirements and Detector Performance goals 127
8.1.1 Physics requirements 127
8.1.2 Detector concept 127
8.1.3 Charged Particle Identification 129
8.2 Particle Identification Overview 129
8.2.1 Experience of *BABAR* DIRC 129
8.2.2 Barrel PID: Focusing DIRC (FDIRC) 129

8.3 Projected Performance of FDIRC 2-3 pages . . . 133
8.3.1 Reconstruction Arnaud, Roberts . . . 133
8.3.2 MC Simulation . . . 133
8.3.3 Effect of Background on performance Roberts . . . 134
8.4 The Barrel FDIRC Detector Overview . . . 134
8.4.1 Impact on other systems Benettoni, Simi, Vavra . . . 134
8.4.2 Photodetectors . . . 134
8.4.3 Laser calibration system . . . 143
8.4.4 FDIRC Mechanical Design . . . 145
8.4.5 Electronics readout, High and Low voltage . . . 155
8.4.6 Integration issues . . . 160
8.4.7 FDIRC R&D Results until now . . . 161
8.4.8 Ongoing FDIRC R&D . . . 164
8.4.9 System Responsibilities and Management . . . 164
8.4.10 Cost, Schedule and Funding Profile . . . 166
8.5 A possible PID detector on the Super*B* forward side . . . 166
8.5.1 Physics motivation and detector requirements . . . 166
8.5.2 Forward PID R&D activities . . . 169
8.5.3 The Forward task force . . . 171
8.5.4 The DIRC-like forward time-of-flight detector (FTOF) . . . 173

9 Electromagnetic Calorimeter **185**
9.1 Overview . . . 185
9.1.1 Background and radiation issues . . . 185
9.1.2 Simulation tools . . . 187
9.1.2.1 Fastsim . . . 187
9.1.2.2 FullSim . . . 188
9.2 Barrel Calorimeter . . . 188
9.2.1 Requirements Relevant to the Super*B* Environment . . . 189
9.2.1.1 Crystal Aging at *BABAR* . . . 189
9.2.1.2 Backgrounds . . . 189
9.2.2 Description of *BABAR* Barrel Calorimeter . . . 191
9.2.2.1 Mechanical design . . . 191
9.2.2.2 Readout . . . 193
9.2.2.3 Low-energy Source Calibration . . . 193
9.2.2.4 Light Pulser . . . 196
9.2.3 Performance of *BABAR* barrel . . . 196
9.2.3.1 Energy and position resolution . . . 196
9.2.3.2 Gamma-gamma mass resolution . . . 196
9.2.3.3 Radiation Damage Effects on Resolution . . . 198
9.2.3.4 Expected Changes in Performance at Super*B* . . . 198
9.2.4 Electronics changes . . . 199
9.2.4.1 Rationale for changes . . . 199
9.2.4.2 Electronics design . . . 200
9.2.5 SLAC De-installation, Transport and Local Storage . . . 200
9.2.6 Electronics refurbishment . . . 200
9.2.7 Re-installation at Tor Vergata . . . 200

9.3 Forward Calorimeter . . . 200
9.3.1 LYSO Crystals . . . 201
9.3.1.1 Introduction . . . 201
9.3.1.2 Optical and Scintillation Properties . . . 201
9.3.1.3 Radiation Hardness . . . 207
9.3.1.4 Specifications, Production and Testing . . . 209
9.3.2 Readout and Electronics[VB] . . . 209
9.3.2.1 APD Readout[DH] . . . 209
9.3.2.2 Electronics Block diagram . . . 210
9.3.2.3 Preamplifier . . . 210
9.3.2.4 Shaper . . . 210
9.3.2.5 Digitization . . . 210
9.3.2.6 Requirements on mechanics . . . 210
9.3.3 Calibrations[DH] . . . 210
9.3.3.1 Initial calibration with source . . . 210
9.3.3.2 Electronics calibration . . . 211
9.3.3.3 Temperature monitoring and correction . . . 211
9.3.4 Mechanical Structure[TZ/FP/VP] . . . 211
9.3.4.1 Crystals . . . 211
9.3.4.2 Modules . . . 212
9.3.4.3 Installation . . . 213
9.3.4.4 Refurbishment of the BaBar structure . . . 213
9.3.4.5 Spare FWD modules survey and tests . . . 213
9.3.5 Performance in simulations[Ch-Ch] . . . 214
9.3.6 Tests on Beam[CC] . . . 214
9.3.6.1 Description of apparatus . . . 214
9.3.6.2 Description of the beams . . . 215
9.3.6.3 Description of data and calibration . . . 216
9.3.6.4 Electronics noise measurements . . . 217
9.3.6.5 Temperature corrections . . . 218
9.3.6.6 Algorithms and results . . . 218
9.3.7 Alternatives . . . 219
9.3.7.1 Full LYSO calorimeter . . . 219
9.3.7.2 Pure CsI . . . 228
9.3.7.3 BGO . . . 228
9.3.7.4 Comparison among options . . . 231
9.4 Backward Calorimeter . . . 233
9.4.1 Requirements . . . 234
9.4.1.1 Energy and angular resolution . . . 234
9.4.1.2 Background rates . . . 235
9.4.1.3 Radiation hardness . . . 235
9.4.1.4 Solid angle, transition to barrel . . . 236
9.4.2 Mechanical design . . . 236
9.4.2.1 Calorimeter construction . . . 237
9.4.2.2 Support and services . . . 238
9.4.3 SiPM/MPPC readout . . . 238
9.4.4 Electronics . . . 239

9.4.5 Calibration . . . 239
9.4.6 Backward simulation . . . 240
9.4.7 Performance in simulations . . . 240
9.4.8 Impact on physics results . . . 240
9.4.9 Use for particle identification . . . 242
9.4.10 Discussion of task force conclusions . . . 245
9.5 Trigger . . . 245
9.5.1 Calorimeter readout trigger . . . 246
9.5.1.1 Normal mode . . . 246
9.5.1.2 Calibration mode . . . 246
9.5.2 Calorimeter trigger primitives . . . 246
9.6 Detector protection . . . 246
9.6.1 Thermal shock . . . 246
9.6.2 Mechanical shock, including earthquakes . . . 246
9.6.3 Fluid spills . . . 246
9.6.4 Electrical surges, outages . . . 246
9.6.5 Radiation damage . . . 246
9.7 Cost & Schedule . . . 246
9.7.1 WBS structure . . . 246
9.7.2 Gantt chart . . . 246
9.7.3 Basis of estimates . . . 246
9.7.4 Cost and schedule risks . . . 246

10 Instrumented Flux Return 253
10.1 Physics Requirements and Performance Goals . . . 253
10.2 Detector Overview . . . 253
10.2.1 The Absorber Structure . . . 253
10.2.2 The Active Detector Choice . . . 255
10.3 Backgrounds . . . 255
10.3.1 Main background sources . . . 255
10.3.1.1 Neutron Background . . . 255
10.3.1.2 Charged Particles . . . 256
10.3.1.3 Photon background . . . 257
10.3.2 Background remediation . . . 257
10.3.3 Radiation doses on the IFR detector . . . 258
10.4 Identification Performances . . . 258
10.4.1 Muon Detection . . . 258
10.4.2 K_L Detection . . . 260
10.5 Detector R&D . . . 260
10.5.1 Module Tests and Results . . . 261
10.5.1.1 Scintillators . . . 261
10.5.1.2 Fibers . . . 261
10.5.1.3 Photodetectors . . . 262
10.5.1.4 Other related studies . . . 263
10.5.1.5 New R&D studies... . . . 263
10.5.1.6 Radiation Damage Studies . . . 263
10.5.1.7 New Radiation Damage Studies . . . 263

10.5.2 Prototype Test and Results . . . 264
10.5.3 Design and construction of the IFR prototype . . . 264
10.5.3.1 Beam Tests . . . 265
10.5.3.2 Tests Results . . . 265
10.6 Baseline Detector Design . . . 267
10.6.1 System Layout . . . 267
10.6.2 Chamber Construction and Assembly . . . 268
10.7 Front-End Electronics . . . 268
10.7.1 General Overview . . . 268
10.7.2 Photodetectors and PCBs . . . 268
10.7.2.1 Photodetector PCB and optical coupling to fibers . . . 268
10.7.2.2 Optical coupling to fibers . . . 269
10.7.2.3 Photodetector location . . . 269
10.7.2.4 Photodetector choice . . . 270
10.7.2.5 Temperature requirements . . . 271
10.8 Final assembly and installation . . . 271
10.9 ES&H issues . . . 272
10.10Structure of the IFR group . . . 272
10.11Cost and schedule . . . 272

11 Magnet and Flux Return 275

12 Electronics, Trigger, Data Acquisition and Online 277
12.1 Architecture Overview . . . 277
12.1.1 Trigger Strategy . . . 277
12.1.2 Trigger Rate and Event Size Estimation . . . 278
12.1.3 Dead Time and Buffer Queue Depth Considerations . . . 279
12.2 Electronics in the SuperB Radiation Environment . . . 280
12.3 Trigger and Event Data Chain . . . 281
12.3.1 Level-1 Trigger . . . 281
12.3.2 Fast Control and Timing System . . . 285
12.3.3 Control and Data Links . . . 288
12.3.4 Common Front-End Electronics . . . 293
12.3.5 Read-Out Modules . . . 294
12.3.6 Network Event Builder . . . 295
12.3.7 High-Level Trigger Farm . . . 296
12.3.8 Data Logging . . . 296
12.4 System Integration and Error Handling . . . 297
12.5 Control Systems . . . 297
12.5.1 Electronics Control System . . . 298
12.5.2 Detector Control System . . . 298
12.5.3 Farm Control System . . . 299
12.6 Other Systems . . . 299
12.6.1 Data Quality Monitoring System . . . 299
12.6.2 Other Components . . . 299
12.6.3 Software Infrastructure . . . 300
12.7 R&D for Electronics, Trigger and Data Acquisition and Online . . . 300
12.8 Organizational Structure of Electronics, Trigger, Data Acquisition and Online . . . 300

12.9 Conclusions . . . 300

13 Subdetector Electronics and Infrastructure 305

13.1 Subsystem-specific Electronics . . . 305
13.1.1 SVT Electronics . . . 305
13.1.2 DCH Electronics . . . 307
13.1.2.1 Design Goals . . . 307
13.1.2.2 Standard Readout - charge measurements specifications . . . 307
13.1.2.3 Standard Readout - time measurements specifications . . . 308
13.1.2.4 Standard Readout - DCH Front-end system (block diagram) . . . 309
13.1.2.5 Standard Readout - ON-DETECTOR electronics . . . 309
13.1.2.6 Standard Readout - OFF DETECTOR electronics . . . 310
13.1.2.7 Sampled Waveforms - specifications . . . 312
13.1.2.8 Sampled Waveforms - DCH front-end system (block diagram) . . . 313
13.1.2.9 Sampled Waveforms - ON DETECTOR electronics . . . 313
13.1.2.10 Sampled Waveforms - OFF DETECTOR electronics . . . 313
13.1.2.11 Front End Crates . . . 314
13.1.2.12 Number of crates and links . . . 314
13.1.2.13 ECS . . . 314
13.1.2.14 Cabling . . . 314
13.1.2.15 Power Requirements . . . 315
13.1.2.16 Grounding . . . 315
13.1.3 PID Electronics . . . 315
13.1.3.1 The TDC chip . . . 316
13.1.3.2 The Front-end Crate . . . 317
13.1.3.3 The Communication Backplane . . . 318
13.1.3.4 The PMT Backplane . . . 318
13.1.3.5 Cooling and power supply . . . 318
13.1.3.6 The front-end board . . . 318
13.1.3.7 The crate controller board (FBC) . . . 318
13.1.4 EMC Electronics . . . 319
13.1.5 IFR Electronics . . . 320
13.1.5.1 Introduction . . . 320
13.1.5.2 Basic features of the IFR detector . . . 320
13.1.5.3 IFR channel count estimation . . . 321
13.1.5.4 Estimations of the IFR event size and data bandwidth . . . 321
13.1.5.5 Background radiation and electronics design constraints . . . 322
13.1.5.6 The IFR readout system . . . 324
13.2 Electronics Infrastructure . . . 332
13.2.1 Power supplies, grounding and cabling . . . 332
13.2.1.1 Power Supply to the Front-end: . . . 332
13.2.1.2 High Voltage Power Supply to the Detectors: . . . 336
13.2.2 Grounding and Shielding . . . 337
13.2.3 Cable Plant . . . 337

14 Software and Computing 341

14.1 Computing Overview F.Bianchi 2 pages . . . 341

14.2 Tools to support detector studies F.Bianchi 1 pages 341
14.2.1 Full Simulation A. Di Simone - E. Paoloni - A. Perez 4 pages 341
14.2.1.1 Bruno: the SuperB full simulation software 341
14.2.1.2 Geometry description 341
14.2.1.3 Simulation input: Event generators 342
14.2.1.4 Simulation output: Hits and MonteCarlo Truth 342
14.2.1.5 Simulation optimization 342
14.2.1.6 Staged simulation 343
14.2.1.7 Interplay with fast simulation 343
14.2.1.8 Long term evolution of the full simulation software 344
14.2.2 Fast Simulation M. Rama 4 pages 344
14.2.2.1 Event generation 344
14.2.2.2 Detector description 345
14.2.2.3 Interaction of particles with matter 345
14.2.2.4 Detector response 346
14.2.2.5 Reconstruction 346
14.2.2.6 Machine backgrounds 347
14.2.2.7 Analysis tools 348
14.2.2.8 Simulation validation and detector studies 348
14.2.3 Distributed computing tools G. Donvito - A. Fella - E. Luppi - S. Pardi L. Tomassetti 10 pages 348
14.2.3.1 Distributed resources 349
14.2.3.2 Distributed systems design: a bird's-eye view 350
14.2.3.3 The production system 350
14.2.3.4 The data analysis system prototype 352
14.2.3.5 The bookkeepieng and data placement database 353
14.2.4 Collaborative tools M. Corvo - A. Gianoli - S. Longo - R. Stroili 2 pages . 354
14.2.4.1 Overview 354
14.2.4.2 Authorization 354
14.2.4.3 Portal System 354
14.2.4.4 Document repository 355
14.2.4.5 Documentation 355
14.2.4.6 Code repository 356
14.2.4.7 Code packaging and distribution 357
14.3 Computing model outline F. Bianchi - A. Fella - C. Grandi - S. Luitz - E. Luppi - S. Pardi - L. Tomassetti 6 pages 357
14.3.1 Data processing 357
14.3.2 Resource estimate F.Bianchi - S. Luitz 4 pages 358
14.3.3 Computing Infrastructure F.Bianchi - S. Luitz - S. Pardi 4 pages . . . 358
14.4 R & D program M. Corvo - G. Donvito - A. Fella - F. Giacomini - S. Longo - S. Pardi 8 pages 360
14.4.1 R& D on parallelization 360
14.4.2 GPU R& D 360
14.4.3 Framework R & D 361
14.4.4 Dirac framework evaluation 364
14.4.5 Distributed Storage R&D 367
14.4.5.1 Wan data access 368

14.4.5.2 Lib data access . . . 368
14.4.5.3 FTS Evolution . . . 369
14.4.5.4 Dynamic file catalogue technology . . . 369
14.4.5.5 Storage system evaluation . . . 369
14.4.6 Reconstruction Framework F. Bianchi 4 pages . . . 371
14.4.7 Analysis Framework F. Bianchi 4 pages . . . 371
14.5 Summary F.Bianchi 1 pages . . . 371

15 Environmental Safety and Health **375**

16 Facilities, Mechanical Integration and Assembly **377**
16.1 Introduction . . . 377
16.1.1 Magnet and Instrumented Flux Return . . . 377
16.2 Component Extraction . . . 378
16.3 Component Transport . . . 379
16.4 Detector Assembly . . . 380

17 The SuperB Collaboration and Project Management **381**
17.1 Collaboration Membership . . . 381
17.2 The Super*B* Collaboration Council . . . 382
17.3 The Super*B* Spokesperson . . . 383
17.4 The Super*B* Executive Board . . . 383
17.5 The Super*B* Management Team and Management Plan . . . 384
17.6 International Finance Review Committee . . . 384
17.7 Interaction with the Cabibbo-Lab . . . 384
17.8 Communications . . . 384
17.9 Construction Responsibilities . . . 385

18 Cost and Schedule **389**
18.1 Detector Costs . . . 390
18.2 Basis of Estimate . . . 394
18.3 Schedule . . . 395

6 Silicon Vertex Tracker

6.1 Overview G.Rizzo - 12 pages

The Silicon Vertex Tracker, as in *BABAR*, together with the drift chamber (DCH) and the solenoidal magnet provide track and vertex reconstruction capability for the Super$B$ detector. Precise vertex information, primarily extracted from precise position measurements near the IP by the SVT, is crucial to the measurement of time-dependent CP asymmetries in B^0 decays, which remains a key element of the Super$B$ physics program. In addition, charged particles with transverse momenta lower than 100 MeV/c will not reach the central tracking chamber, so for these particles the SVT must provide the complete tracking information.

6.1.1 SVT and Layer0

The above goals have been reached in the *BABAR* detector with a five-layer silicon strip detector with a low mass design, shown schematically in Fig. 6.1. The *BABAR* SVT provided excellent performance for the whole life of the experiment, thanks to a robust design that took into account the physics requirements as well as enough safety margin, to cope with the machine background, and redundancy considerations [2].

The Super$B$ SVT design, shown schematically in Fig. 6.2, is based on the *BABAR* vertex detector layout with those modifications needed to operate at a luminosity of 10^{36} or more, and with a reduced center-of-mass boost. In particular the SVT will be equipped with an innermost layer closer to the IP (Layer0) to improve vertex resolution and compensate the reduced boost at the Super$B$ accelerator, thus retaining an adequte Δt resolution for B decays for time-dependent CP asymmetries.

Physics studies and background conditions, as explained in detail in the next sections, set stringent requirements on the Layer0 design: radius of about 1.5 cm; resolution of 10-15 μm in both coordinates; low material budget (about 1% X_0); and adequate radiation resistance.

Several options are under study for the Layer0 technology, with different levels of maturity, expected performance and safety margin against background conditions. These include striplets modules based on high resistivity double-sided silicon detector with short strips (tilted with respect to detector's edge), hybrid pixels and other thin pixel sensors based on CMOS Monolithic Active Pixel Sensor (MAPS).

The current baseline configuration of the SVT Layer0 is based on the striplets technology, which has been shown to provide the better physics performance, as detailed in the next sections. However, options based on pixel sensors, which are more robust in high background conditions, are still being developed with specific R&D programs in order to meet the Layer0 requirements, which include low pitch and material budget, high readout speed and radiation hardness. If successful, this will allow the replacement of the Layer0 striplets modules in a "second phase" of the experiment. For this purpose the Super$B$ interaction region and the SVT mechanics will be designed to ensure a relative rapid access to the detector for a replacement of Layer0.

The external SVT layers (1-5), with a radius between 3 and 15 cm, will be built with the same technology used for the *BABAR* SVT (double sided silicon strip sensor), which is adequate for the machine background conditions expected in the Super$B$ accelerator scheme (*i.e.*with low beam currents). Although SVT module design for layer1 to 5 will be very similar to the *BABAR* one, with a larger coverage, a complete new readout electronics chain need to be developed to cope with the higher background rates expected in Super$B$.

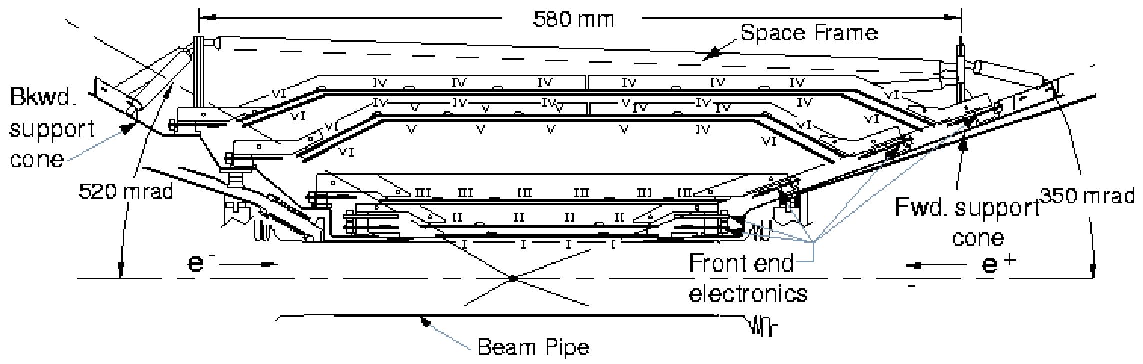

Figure 6.1: Longitudinal section of the *BABAR* SVT

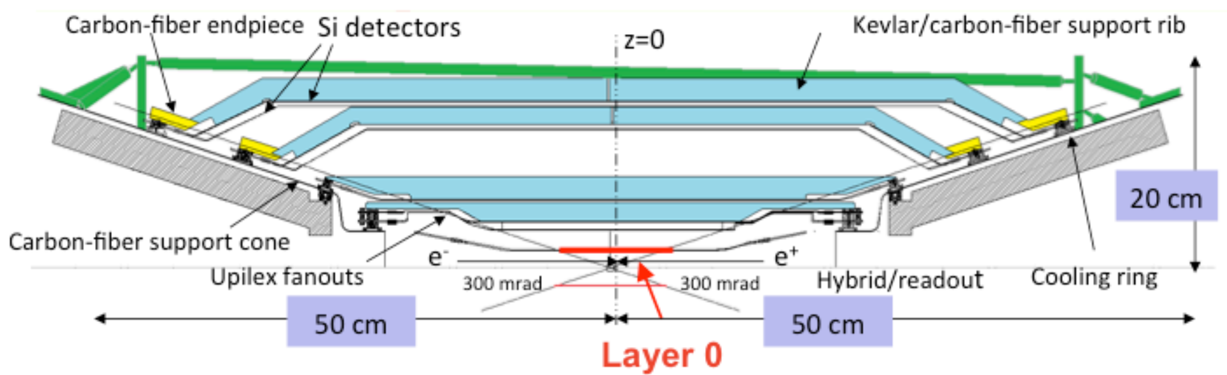

Figure 6.2: Longitudinal section of the Super*B* SVT

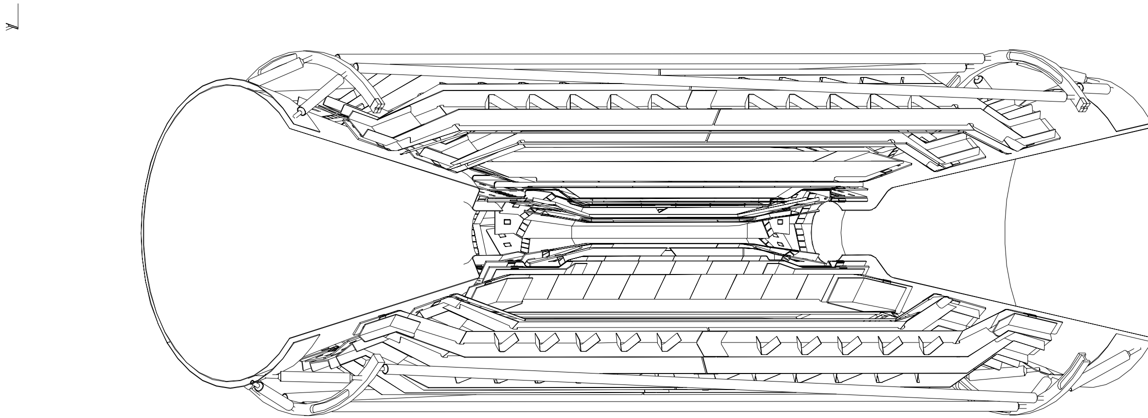

Figure 6.3: Three dimensional cutaway of the SVT.

A review of the main SVT requirements will be given in the next section followed by an overview of the general detector layout. A detailed discussion of all the specific design aspects will be covered in the rest of the chapter.

6.2 SVT Requirements

6.2.1 Resolution

Without the measurement of the B decay vertex, no useful CP asymmetries can be extracted at the $\Upsilon(4S)$. Therefore one of the main goal of the SVT is the determination of the B decay positions, especially along the beam direction (z). Measurements performed in *BABAR*, where the mean separation between B vertices is $\Delta z \simeq \beta\gamma c\tau_B = 250\,\mu$m, demonstrated that good sensitivity to time dependent measurement can be achieved with typical vertex resolution of 50-80 μm in the z coordinate for exclusively reconstructed modes, and 100-150 μm for inclusively modes (tag side in CPV measurements). The reduced Super$B$ boost ($\beta\gamma = 0.24$) with respect to PEP-II ($\beta\gamma = 0.55$) requires an improved vertex resolution, by about a factor 2, in order to mantain a suitable Δt resolution for time dependent analyses.

The *BABAR* resolution was achieved thanks to an intrinsic detector resolution of about 10-15 μm in the first measured point of the SVT, taken at a radius of about 3 cm, and keeping to the minimum the amount of material between the IP and the first measurement. The multiple scattering has in fact an important effect on impact parameter resolution for low momentum tracks and set a lower limit on the useful intrisic resolution on the various SVT layers, corresponding to a point resolution of about 10-15 μm for measurements made close to the IP and 30-40 μm for the outer layers [1].

The required improved track impact parameter and vertex resolution can be reached in Super$B$ with the same intrisic resolution used in *BABAR*, reducing the radius of the first measured SVT point by a factor of 2 (Layer0 radius at about 1.5 cm) and keeping a very low mass design for the beam pipe and the detector itself.

6.2.2 Acceptance

The coverage of the SVT must be as complete as technically feasible, given the constraints of the machine components close to the IP. The SVT angular acceptance, constrained by the Super$B$ interaction region design, will be 300 mrad in both the forward and backward directions, corresponding to a solid angle coverage of 95% in the $\Upsilon(4S)$ center-of-mass frame, thus increasing the acceptance with respect to *BABAR* SVT.

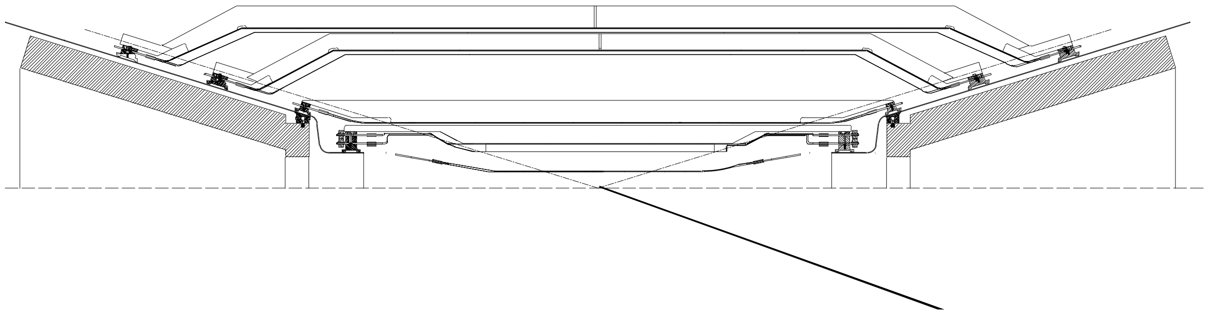

Figure 6.4: Cross section of the SVT in the plane containing the beam axis.

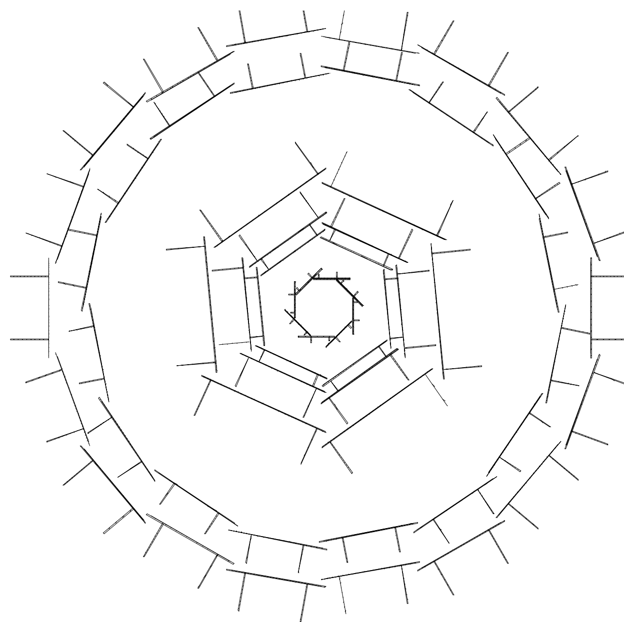

Figure 6.5: Cross section of the SVT in the plane perpendicular to the beam axis. The lines perpendicular to the detectors represent structural support beams.

There should be as little material as possible within the active tracking volume. The minimization of the material between the IP and the first measurement is crucial to reduce the multiple scattering and preserve the impact parameter resolution. The small beam pipe (1 cm radius) in the dector acceptance requires an active cooling with liquid coolant to evacuate the large power dissipated from image beam currents. The total amount of radial material for the actual design of this new beryllium pipe is estimated to be less than 0.5% X_0. Material located beyond the inner layers does not significantly degrade the measurement of track impact parameters, but does affect the performance of the overall tracking system and leads to increased photon conversions in the active region.

6.2.3 Efficiency

Our goal is to achieve close-to-perfect track reconstruction efficiency within the active volume of the tracking detectors when information from both the drift chamber and the SVT is used. The pattern recognition capabilities of the combined tracking system must be robust enough to tolerate background levels up to 5 times nominal. *as defined in background section* Low momentum particles that do not traverse many drift chamber planes, such as many of the charged pions from D^* decays, must be reconstructed in the SVT alone. For this category of tracks, with p_T less than 100 MeV/c, we want to achieve reconstruction efficiencies of at least 80–90%. *check these number with fastsim results in high background* The SVT must also be efficient for particles such as K^0_Ss that decay within the active volume.

Together, these requirements determine the number of measurements along a track and the necessary single-hit efficiency. *do we need to quote some numbers here?.* The BABAR SVT design with 5 layers was optimized to ensure enough redundancy to keep an high tracking efficiency even in case of failure of some modules and inefficient detectors. The robustness of this choice was demonstrated with the good detector performance over the entire life of the experiment. The Super*B* SVT design with 6 layers (inserting the Layer0) is inspired to the same philosophy. Specific simulation studies [3] indicated that a reduction in the number of layers, from 6 to 5 or 4, give very modest gain in tracking performance while show a sizeble reduction in the efficiency for low momentum tracks in D* reconstruction, in case of non perfect/real detector, or related to inefficiency in high background conditions.

6.2.4 Background & Radiation Tolerance

The expected background influences several aspects of the SVT design (segmentation, shaping time, data transmission rates) and sets the requirements for the radiation resistance of all the SVT components. The design of the system has been optimized to withstand at least 5 times the total expected background rates. Whenever possible, detectors and front-end electronics are specified to be able to survive the entire life of the experiment including a safety factor of 5 on the total dose and equivalent neutron fluence: 7.5×5 yrs at nominal peak luminosity of 10^{36}.

As described in Section 6.6, the effect of background depends steeply on radius, as shown in Tab. 6.1.

With the high strip rates expected, especially in the inner layers (0-3), the front-end electronics should be fast enough to avoid pulse overlap and consequent hit inefficiency (shaping time in the range 25-150 ns). Furthermore a good Time Stamp resolution (30 MHz TS clock) is needed to get a good hit time resolution and reduce the occupancy in the offline time window to acceptable levels for reconstruction. An average 2% offline cluster occupancy is reached in each layer, considering the nominal background x5, with offline time windows of 100-150 ns in layers 0-3, while about 500 ns will be selected in layers 4-5, where the longer shaping time is dominating the hit time resolution. See Sections 6.7.5 and 6.10.2 for more details.

In Layer0 the expected integrated dose is about 3 Mrad/yr and the equivalent neutron fluence is about 5×10^{12} n_{eq}/cm^2/yr in the sensor area. In the other SVT layers radiation levels are at least one order of magnitude lower: in

Table 6.1: Summary of nominal expected background in the sensor area. The design of the SVT has been optimized with ×5 the nominal background. *Elba numbers for rates, New TID-NIEL, syncrotron radiation not included yet.*

Layer	Radius (mm)	Pitch (ϕ–z) (μm)	Total Rate/Area Track (MHz/cm^2)	Cluster	Strip (ϕ–z)	Total Strip Rate (kHz)	TID (Mrad/yr)	NIEL (n/cm^2/yr)
0	15	54–54 (u,v)	1.62	4.10	20–20 (u,v)	187–187	3	$5{\times}10^{12}$
1	33	50–100	0.217	0.540	2.9–2.4	170–134	0.3	$8{\times}10^{11}$
2	40	55–100	0.163	0.393	1.9–1.7	134–134	0.2	$5{\times}10^{11}$
3	59	50-1-00	0.079	0.208	0.54–0.71	116–79	0.1	$3{\times}10^{11}$
4	120	100–210	0.022	0.037	0.07–0.05	25–13	0.01	$2{\times}10^{11}$
5	140	100–210	0.014	0.022	0.04–0.03	16–9	0.01	$2{\times}10^{11}$

Layer1 TID $\simeq$ 0.3 Mrad/yr and an equivalent neutron fluence of about 8×10^{11} n_{eq}/cm^2/yr are expected.

With this scenario in Layer1-5 the sensors are proven to be enough radiation hard to survive the entire life of the experiment, with a safety factor of 5 included, with an acceptable degradation of the Signal to Noise performance, as shown in Section 6.10.2. *review this sentence after proper evaluation of S/N.* As an example this requirement translates for Layer1 to a TID $\simeq$ 15 Mrad and an equivalent neutron fluence of about 3×10^{13} n_{eq}/cm^2 (7.5x5 yrs equivalent).

For Layer0, where the radiation is an order of magnitude higher, a quick replacement of the entire layer is foreseen, as frequent as necessary, depending on the actual background and the radiation hardness of the technology chosen.

6.2.5 Reliability

Although the SuperB interaction region and the SVT mechanics will be designed to ensure a relative rapid access to the detector for replacement of Layer0, the acces of the SVT is not possible without a major shutdown. The reliability requirements for the SVT are therefore more stringent than usual for such a device, with implications for engineering design at all levels. The detector layout must provide redundant measurements wherever possible; the electronic readout must be very robust; and the functionality of all components must not be compromised by exposure to the expected radiation levels. The detector monitoring and interlock system must serve as a safeguard against catastrophic failure in the event of a component malfunction or a simple human error.

6.3 Baseline Detector Concept

6.3.1 Technology

The SVT baseline design is based on double-sided silicon microstrip detectors for all layers. The characteristics of this technology that make it attractive for the Super*B* detector are: high precision for measuring the location of charged particles, tolerance to high background levels, and reduction in mass made possible through double-sided readout. Double-sided silicon detectors have been employed with success already in *BABAR* and in several other large-scale applications and are able to meet the performance standards outlined above.

6.3.2 Layout

The SVT will provide six measurements, in two orthogonal directions, of the positions of all charged particles with polar angles in the region $17° < \theta < 167°$. A three-dimensional cutaway view of the SVT is shown in Figure 6.3. The Layer0 has eight detector modules while

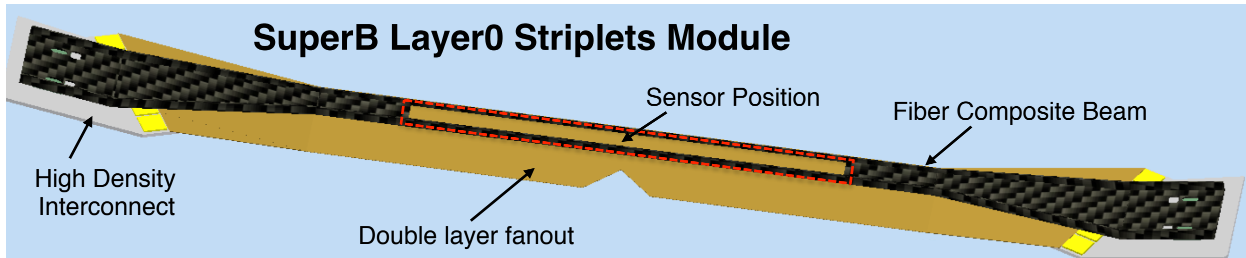

Figure 6.6: Schematic drawing of the Layer0 striplets module

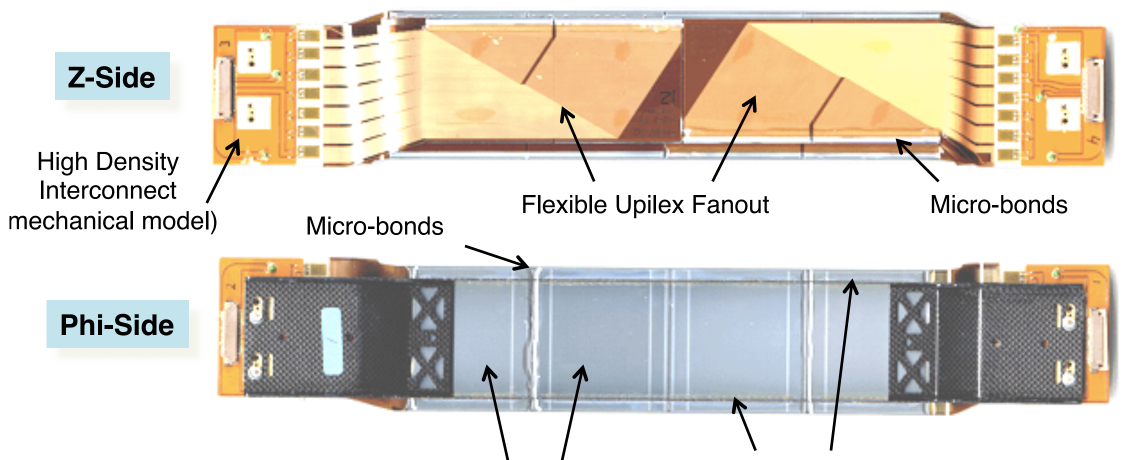

Figure 6.7: Details of the *BABAR* SVT Layer1 module.

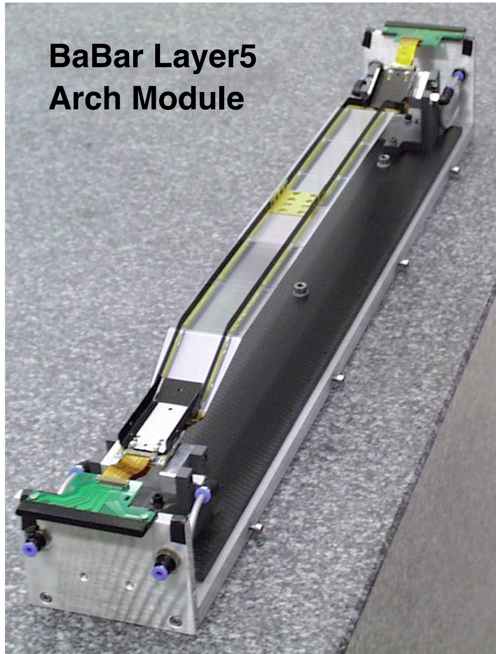

Figure 6.8: Details of the *BABAR* SVT Layer5 arch module.

the rest of the detector keep the same modules numbers as in *BABAR* : layers 1-2-3 have six detector modules, arrayed azimuthally around the beam pipe, while the outer two layers consist of 16 and 18 detector modules, respectively. A side view of the detector is shown in Figure 6.4, and an end view is shown in Figure 6.5.

The design of the Layer0 striplets module is completly new, with a quite complex shape, as shown in Fig. 6.6, to fit the very limited space available between the first layer of SVT and the beam pipe. The layout of the other five layers is very similar to the *BABAR* SVT strip modules, shown as a reference in Fig. 6.7 and Fig. 6.8.

The inner detector modules (0-3) are traditional barrel-style structures, while the outer detector modules (4-5) employ an arch structure, in which the detectors are electrically connected across an angle. The bends in the arch modules, proven to be well functional in *BABAR*, minimize the area of silicon required to cover the solid angle and also avoid very large track incident angles.

In order to satisfy the requirement of minimizing material in the detector acceptance region, one of the main features of the SVT design is the mounting of the readout electronics entirely outside the active detector volume. For this reason signals from the silicon strips are carried to the front-end chips by flexible fanout circuits.

There is a 1 cm space between the 300 mrad stay-clear in the forward and backward directions and the first element of the IR region (i.e. the tungsten shield cones) and all of the electronics are mounted here. In both directions, space is very tight, and the electronic and mechanical designs are closely coupled in the narrow region available.

The layout specifications for this six-layer design are given in Table 6.3.2 and described in more detail the text.

For Layer0 short strips, oriented at 45 degrees with respect to the detector edges (u, v strips), are adopted on both faces of the sensor in order to reduce the strip length and the related background occupancy to reasonable levels. For layers 1 to 5 the strips on the two sides of the rectangular detectors in the barrel regions are oriented parallel (ϕ strips) or perpendicular (z strips) to the beam line. In the forward and backward regions of the two outer layers, the angle between the strips on the two sides of the trapezoidal detectors is approximately 90°, and the ϕ strips are tapered. Floating strips are used to improve the position resolution for near-perpendicular angles of incidence; the capacitive coupling between the floating strip and the neighboring strips results in increased charge sharing and better interpolation. For larger incident angles with wider readout pitch minimizes the degradation in resolution that occurs because of the limited track path length associated with each strip. These issues are discussed in more detail in section 6.8.2.

The design has a total of 308 silicon detectors of nine different types. The total silicon area in the SVT is about 1.5 m ^{2}, and the number of readout channels is ∼170,000.

Table 6.2: *need to update the table* Parameters of the SVT layout.
See text for more detail on the meaning of the different quantities. The intrinsic resolution is calculated at 90° track incidence assuming $S/N = 20 : 1$. The z-ganging/pairing numbers represent the percentage of readout channels connected to the specified strip configuration.

Quantity	Layer 0	Layer 1	Layer 2	Layer 3	Layer 4a	Layer 4b	Layer 5a	Layer 5b
Radius (mm)	15	33	40	59	120	124	140	144
Wafers/Module	1	2	4	4	6	6	8	8
Modules/Layer	8	6	6	6	8	8	9	9
Silicon Area (cm^2)	127	554	787	1655	2459	2548	3502	3610
Overlap in ϕ (%)	2.0	2.4	1.8	1.8	4.0	4.0	2.0	2.0
Readout pitch (μm):								
ϕ (u for Layer 0)	54	50	55	100	82–100		82–100	
z (v for Layer 0)	54	100	100	110	210		210	
Floating Strips:								
ϕ (u for Layer 0)	—	—	—	1	1		1	
z (v for Layer 0)	—	1	1	1	1		1	
Intrinsic Resolution (μm):								
ϕ (u for Layer 0)	10	10	10	10	10–12		10–12	
z (v for Layer 0)	12	12	12	12	25		25	
R.O. Section								
ROS/Module	4	4	4	4	4		4	
ICs/ROS (ϕ-z)	6-6	7-7	7-7	6-10	4-5		4-5	
Readout Channels	24576	21504	21504	24576	36864		41472	
Strip Length Half Module (mm):								
ϕ (u for Layer 0)	20	110	130	190	293	303	369	380
z (v for Layer 0)	20	40	48	70	51–103	103–154	103–154	103–154
Fraction of z-side r.o. channels with Pairing/Ganging:								
None		77%	55%	65%	4%			
Pairing ×2		23%	45%	35%				
Ganging ×2					73%	74%	25%	16%
Gang.×2 + Pair.×2					23%	24%	41%	43%
Ganging ×3						2%	34%	41%

6.3.3 Electronic Readout

As emphasized above, all readout electronics are located outside the active volume, below 300 mrad in the forward and backward region. To accomplish this, ϕ strips on the forward or backward half of a detector module are electrically connected with wire bonds. This results in total strip lengths associated with a single readout channel of up to $\sim$19 cm in the inner layers and up to $\sim$38 cm in the outer two layers.

The signals from striplets for the Layer0 (u and v strips) and the z strips for all the other layers are brought to the readout electronics using fanout circuits consisting of conductive traces on a thin flexible insulator (for example, copper traces on Upilex as in *BABAR*). The traces on fanout are wire-bonded to the ends of the silicon strips.

On the z side of the modules the number of readout strips exceed the number of available electronic channels, constrained by the number of chips that can fit in the limited space available. To reduce the number of readout channels needed, the connection scheme for the z fanout circuits includes "pairing" and "ganging" (described in Section 6.8.2) with two or three strips bonded to a single fanout/readout channel. The length of the z strips is much shorter than ϕ strips, typically 4-7 cm in the inner layers and either 10 or 15 cm in the outer layers, where there is either $\times 2$ or $\times 3$ ganging.

Front-end signal processing is performed by ICs mounted on the High-Density Interconnect (HDI), a thick-film hybrid circuit fabricated on aluminum nitride (AlN) substrate. The HDI provides the physical support, it distributes power and signals, and thermally interfaces the ICs to the cooling system.

New front-end custom-design ICs are currently under developmemnt for the Super*B* SVT [17] since none of the existing chips is matching all the requirements 6.10.2. The signals from the readout strips, after amplification and shaping, are compared to a preset threshold. The time interval during which they exceed the threshold (time over threshold, or TOT) is an analog variable related to the charge induced on the strip. Unlike the ordinary peak-amplitude measurement at the shaper output, the TOT technique has a nonlinear input-to-output relationship which is approximately logarithmic. This is an advantage since it compresses the dynamic range and allows one to achieve good position resolution and large dynamic range with a minimum number of bits. TOT readout has been successfully employed in the front-end chip of the *BABAR* SVT (i.e. Atom chip [2]) providing sufficient analog resolution for position interpolation, time-walk correction, and background rejection.

For each channel with a signal above threshold, the TOT information together with the hit time stamp will be buffered until a trigger is received; it will be then transferred, with the strip number, to an output interface, where data will be serialized and transmitted off chip on output LVDS lines.

The readout IC is expected to be about 6x4 mm^2 and to dissipate about 4.0 mW per channel. The total power that will be generated by the SVT readout chips is $\sim$700 watt (*considering 4 mW/chan is correct including the digital power?*).

There are four readout sections per detector module, where the module is divided in half along z, and the ϕ and z strips are grouped together separately. The data from one-half of a detector module will be transmitted from the hybrid on a flexible cable to a transition card located approximately 40 cm away, where the signals are converted and transmitted to optical fibers.

6.3.4 Module design and Mechanical Support

review this section The silicon detectors and the associated readout electronics are assembled into mechanical units called detector modules. Each module contains from 1 to 8 silicon detectors, the flex circuits to bring the signal from strip to the front-end chips, and a low-mass beams constructed of carbon and Kevlar fiber-epoxy laminates (i.e. ribs) to stiffen the module structure. The ribs are attached at each end to to the HDI hybrid circuit. A Aluminum Nitride

substrate for the HDI provides precise mechanical mounting surfaces and is the heat sink for the electronics.

With this design the module material budget in the active region is very limited, and as in BABAR is about 0.45% X_0 per layer. For layers 1 to 5 this is dominated by the 300 μm of the silicon sensor, a contribution of about 0.1 % X_0 is due to the composite ribs, with about 0.05 % X_0 for the z fanout, the one that sits in the active area. In Layer0 striplets the contribution of the flex circuit is considerably higher: here each face of the sensor need a flex circuit in the active area, since both u and v strips, at 45^0 w.r.t detector edge, need to be connected to the front-end chips. Furthermore the flex on each face of the striplets module is a double layer, since the number of channels to be connected is very high and the pitch is limited to about 50μm. The total material for the two multilayer flex circuits, now uder development, is about 0.15 % X_0, while about 0.1 % X_0 are accounted for the carbon fiber support structure. With sensor thickness of the stripltes of only 200 μm the total material budget is about 0.45% X_0 also for Layer0.

Layer 0 modules are supported on cold flanges, directly coupled with Be beam-pipe *describe Layer0 mounted on beam pipe motivations: minimize radial position and quick demounting of layer 0 without touching the SVT and* The other five SVT layers are mounted on support cones coupled with the conical tungsten shields with kinematic mounts (i.e. the gimbal rings) that will allow relative motions of the forward backward shields without stress on the silicon detectors. The detector modules from Layers 1 and 2 are glued together with rigid beams, forming sextants which are then mounted from the support cones in the forward and backward directions. Each detector module of Layer 3-4-5 is mounted on the support cones independently of the other modules. In layer 4 and 5, there are two different types of modules in each layer, an inner one, labeled *a*, and an outer one, labeled *b*, occupying slightly different radial positions. Thus there are eight different types of detector modules.

The support cones are double-layered carbon-fiber structures which are mounted from the tungsten shield cones. Cooling water flows between the two carbon-fiber layers around aluminum mounts which protrude through the outer surface of the cone. Mounting pins in the hybrid structure provide the alignment between the modules and the aluminum mounts in the cone, and thermal contact is made to provide cooling for the front-end electronics located on the hybrid. The support cones are divided to allow the vertex detector to be assembled in two halves and then mounted on t he shielding cones and the beam pipe by clamshelling the pieces together. During the assembly/disassembly procedure the splitting of the support cones with the five SVT layers on, will allows an easy access of the Layer0 without the need to disassemble the entire SVT.

The stiffness of the overall SVT structure is provided by a very low mass space frame, constructed of carbon-fiber tubes, connecting the forward and backward support cones, similar to the one designed for the BABAR SVT. It consists of rings at each end held rigid by struts spanning the length of the detector. The rings are connected to the support cones by an additional series of struts at each end. All material is carbon-fiber laminate. The motivation for this space frame stems mainly from the possible relative motion of the two shielding cones during the assembly procedure or earthquake *check this and add gimbal ring description* Cooling water, power, and signal lines are routed along the support cones to points outside the active region where manifolds for the cooling water and drivers for the electronics are located.

6.4 Layer0 Pixel Upgrade

6.4.1 Motivations

With the machine operated at full luminosity, the layer 0 of SVT may benefit from upgrading to a pixellated detector that have more stable performance in case of high background

conditions, thanks to a lower background rate expected. A background rate of about 1 MHz/strip (x5 safety included) is expected with a striplets lenght of about 2 cm and 50μm pitch, while only 2.5 KHz/pixel are expected for pixels with a 50x50 μm pitch.

Possible effects of background hits on performance are: the reduction of the hit reconstruction efficiency (due to pile up), the increase of the effective hit resolution, the reduction of efficiency of the pattern recognition for charged tracks along with the increase of fake tracks. Most of these effects have been included in specific simulation studies performed to evaluate the SVT performance in the high background scenario, (i.e. full luminosity including x5 safety factor on nominal background). The results, described in more details in Sec.**??**, showed a significant degradation in the striplets performance with high background occupancy, while the pixel solutions explored showed more stable performance against background conditions. The pixel occupancy is reduced at least by a factor 200 w.r.t striplets considering the smaller electrode dimensions and even including a possible worse time resolution of the pixel w.r.t striplets.

An example of these studies is shown here. The impact of machine background on the SVT performance has been studied evaluating the per-event error on the physics parameter S, adding background hits to signal events. S is measured in time-dependent analyses (corresponds to $\sin(2\beta)$ for $B^0 \to J\psi K^0_S$ decays) and the S per-event error is defined as the error on the parameter S normalized to the number of signal events. In Fig.6.9 the impact of background on the physics parameter S is reported for striplets and pixel, for the case of nominal background and with 5 times background rates. For the striplets the reduction to the sensitivity to S w.r.t. BaBar is small with nominal background, only about 3%, but it is up to about 15% with 5 times the nominal background. On the contrary with a pixel option, beeing there the effect of background occupancy negligible, the reduction to the sensitivity to S is only 3%, even in the high background scenario, and it is related to the effect of the background in the rest of the SVT.

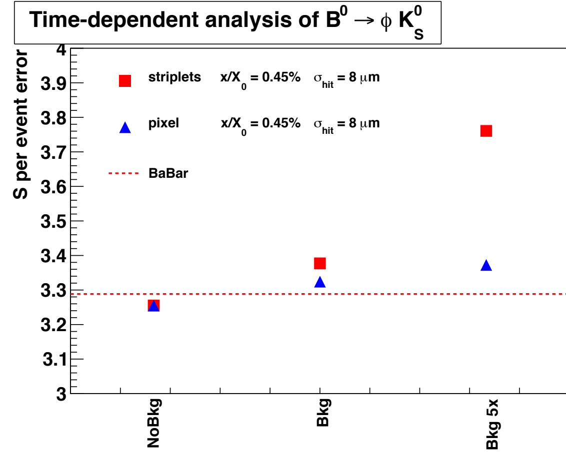

Figure 6.9: Variation of the S per event error in $B^0 \to \phi K^0_S$ time-dependent analysis in presence of background events, for a Layer0 based on striplets or pixel with the same material budget. Efficiency and resolution deterioration are both included in the simulation study.

It is important to stress that in the study reported here the pixel option has the same material budget used for striplets (about 0.45% X_0), same performance without background included. Of course the use of pixel over striplets in high background is less convenient if the material budget of pixels is significantly higher. On the contrary if one can reach a very low material budget with a thin pixel option, below the striplets target, the upgrade to pixel for Layer0 is well motivated also in nominal backround conditions. (see for example Fig.6.19).

While for strip modules most of the material budget is due to the silicon of the sensor itself, in pixel modules there are several other important contributions in the active area. Including the readout electronics, cooling, and the pixel bus for the connection of the front-end chips with the periphery of the module, one one can easily reach a total material budget for pixel above

1% X_0. A discussions on the material for the various pixel options for the Layer0 is presented in the next sections.

6.4.1.1 Technology Options for Layer0 pixel upgrade

Two main technologies are under evaluation for the upgrade of Layer0: hybrid pixel and thinner CMOS Monolithic Active Pixel Sensor (MAPS). Specific R&D programs are ongoing on these options to meet all Layer0 requirements, such as low pitch and material budget, high readout speed and radiation hardness.

A short summary of the current status of the R&D on the different pixel options is given below, while a more detailed review is presented in Sec.6.12.

Hybrid Pixel technology represents a mature and viable solution but reduction in the front-end pitch and in the total material budget, with respect to pixel systems developed for LHC experiments, is required for application in Layer0.

The spatial resolution constraints of 10-15 μm set a limit to the area of the elementary readout cell and, as a consequence, to the amount of functionalities that can be included in the front-end electronics. For a pixel cell 50×50 μm^2 a planar 130 nm CMOS technology may guarantee the required density to implement in-pixel data sparsification and fast time stamping ($< 1 \mu s$), as required for the high target hit rate in Layer0 of 100 MHz/cm^2 in order to keep the module bandwidth to acceptable level (<5 Gbit/s).

Denser CMOS technologies, as the 65 nm technology, can be used to increase the functional density in the readout electronics and include such functions as local threshold adjustment and amplitude measurement and storage. In this case, costs for R&D and production would increase significantly. Vertical integration (or 3D) CMOS technologies may represent a lower cost alternative to sub-100 nm CMOS processes to increase the functional density in the pixel cell [27, 28].

A front-end chip for high resistivity pixel sensors with 50×50 μm^2 pitch is under development for the application in Super*B* A first prototype chip with 4k pixels has been produced with the ST Microelectronics 130 nm process adopting the same readout architecture, with in-pixel sparsification and timestamping, developed within the SLIM5 Collaboration [35] for CMOS Deep NWell MAPS [36, 37]. The chip bump bonded to a high resistivity sensor matrix has been fully characterized, with beams, with good results [23].

In this first prototype only basic functionalities have been implemented. The readout architecture has been recently optimized to sustain efficiently the target Layer0 hit rate of 100 MHz/cm^2 on matrices larger than 50k pixels. The new architecture, that requires a more complex in-pixel logic, implement a data push and a triggered version of the readout [22].

The design of a 3D front-end chip for hybrid pixel with this new readout architecture, and some improved features, is now in progress with the vertical integration CMOS technology offered by the 130 nm Chartered/Tezzaron process.

CMOS MAPS are very appealing for application where the material budget is critical: in this technology the sensor and readout electronics share the same substrate that can be thinned down to several tens of microns. Since a fast readout is another crucial aspect for Layer0 a new Deep NWell MAPS design approach has been developed by the SLIM5 Collaboration[35]) to improve readout speed in CMOS MAPS sensors. This approach allowed for the first time the implementation of thin CMOS sensors with similar functionalities as in hybrid pixels, such as pixel-level sparsification and fast time stamping [36, 22]

Thanks to an intense R&D program the development of DNW CMOS MAPS (with the ST Microelectronics 130 nm process) has reached a good level of maturity. A limiting factor in this design is the presence of competitive N-Wells, inside the pixel cell, that can subtract charge to the main collecting electrode. The last prototype realized, the APSEL4D chip, a 4k pixel matrix with $50 \times 50 \mu$m^2 pitch has been tested with beams [18] reporting a hit efficiency

of 92%, related to the pixel cell fill factor (ratio of the DNW area to the total area of N-wells) which is about 90% in the APSEL design. Another critical issue for the application of CMOS MAPS in the Layer0 is their radiation hardness expecially related to bulk damage effect. A significant degradation of the charge collected (about 50%) has been measured after irradiation with neutron up to a fluence of about 7x10^{12} n/cm^2, corresponding to about 1.5 years of operation in the Layer0 [26].

Further MAPS performance improvements are currently under investigation with two different approaches: the use of INMAPS CMOS process, featuring a quadruple well and an high resistivity substrate, and 3D CMOS MAPS, realized with vertical integration technology.

In order to increase the charge collection efficiency the INMAPS 180 nm CMOS process is being explored: a deep P-well implant, deposited beneath the competitive N-Wells, can prevent them from stealing charge to the main collecting electrode. Moreover the use of high resistivity substrate, also available in this process, can further improve charge collection and radiation resistance with respect to standard CMOS devices. First prototype INMAPS matrix, with the improved readout architecture suitable for the application in the SuperB Layer0, are currently under test with promizing results. Radiation hardness of these devices at the level required for a safe operation in Layer0 for at least a couple of years ($> 10^{13}$ n/cm^2) is currently under investigation.

The realization of 3D MAPS, using two CMOS layers interconnected with vertical integration technology, also offer several advantages with respect to standard 2D MAPS. In these devices one CMOS tier is hosting the sensor with the analog front-end and the second tier is dedicated to the in-pixel digital front-end and the peripheral readout logic. With this splitting of functionalities the collection efficiency can be improved, significantly reducing the N-Well competitve area in the sensor layer. Having more room for the in-pixel logic allows the implementation of a more performant readout architecture. Finally in 3D MAPS the cross-talk between analog and digital blocks can be minimized.

The characterization of first 3D MAPS prototypes, realized with the 130 nm Chartered/Tezzaron 3D process is under way and first beamtest results on the MAPS layer implementing the sensor and the analog front end showed a very good hit efficiency (above 98%).

The status of the R&D on the different pixel options under development for the Layer0 upgrade is reviewed in the following documents [16, 23, 26]

6.4.1.2 Pixel Module & Material Budget

The schematic drawing of the full Layer0 made of 8 pixel modules mounted around the beam pipe is shown in Fig. 6.10.

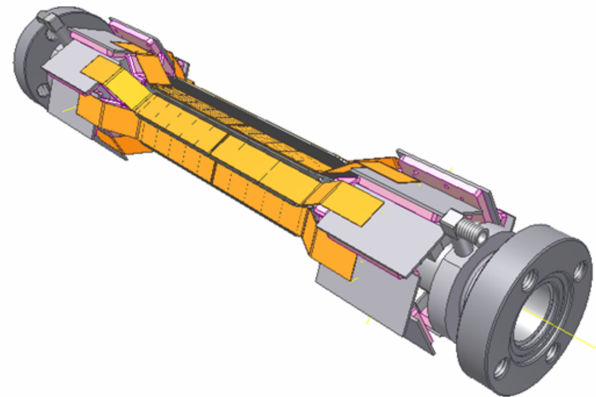

Figure 6.10: Schematic drawing of the full Layer0 made of 8 pixel modules mounted around the beam pipe with a pinwheel arrangement.

In all the pixel options under evaluation, sharing the same multichip module structure, the material budget of all the components must be kept under control to minimize the detrimental effect of multiple scattering.

The main contributions to the material budget for pixel modules with different technologies are discussed in this section and summarized in table 6.3 with a comparison with the striplets option.

Layer0 Module Material Budget (X_0)			
	Striplets	Hybrid Pixel	CMOS MAPS
Sensor	0.21%	0.11-0.21%	0.05%
FE-chip+bump bonding		0.14-0.19%	
Multilayer bus or fanout	0.15%	0.15-0.30%	0.15-0.30%
Module Support & ground plane (include cooling for pixels)	0.09%	0.15%	0.15%
Total Material Budget (X_0)	0.45%	0.55-0.85%	0.35-0.50%

Table 6.3: Layer0 module material budget for the different technologies under evaluation.

In the hybrid pixel solution the contribution of the silicon from the sensor (100-200 μm) and the front-end chip (100-150 μm) can be in the range of 0.25-0.4% X_0. In the CMOS MAPS option the sensor and the front-end electronics are integrated in the same CMOS chip that could be thinned down to 50 μm reducing this contribution down to only 0.05% X_0.

Another important contribution to the material is due to the pixel bus needed for the connection of front-end chips to the periphery of the module. This connection will be realized with an Al/kapton multilayer bus, now under development. With our present requirements on speed (high bandwidth due to a hit rate of 100 MHz/cm2) and power consumption (about 1.5W/cm^2) the estimated material budget for the pixel bus is about 0.15-0.3% X_0, depending on the achievements of present R&D on this item.

The pixel module support structure needs to include a cooling system to evacuate the power dissipated by the front-end electronics, about 1.5W/cm^2, present in the active area. In order to minimize the material budget a light carbon fiber support structure with integrated active cooling, based on microchannel technology [30] and forced liquid convection, has been developed. The support with integrated cooling is build with carbon fiber micro-tubes, with a hydraulic diameter of about 200μm, obtained by a poltrusion process. Measurements on the support prototypes, with a total material budget as low as 0.11% X_0, indicate that such approach is a viable solution to the thermal and structural problem of Layer0 [31] An innovative idea is also under development to integrate into the silicon itself the cooling system based on microchannels made by DRIE technology. The embedded microchannels, with diameters even below 100μm, feature a peculiar geometry, and in the final step a thin oxide layer is deposited to seal the channels, resulting reliable under the operating high-pressure conditions. This technique permits the integration of the cooling system within the detector with obvious advantages on the optimization of thermal bridges and transparency to the incident particles [32].

6.5 R&D Main Activities

6.6 Backgrounds R.Cenci - 4 pages

A detailed analysis of background effects is fundamental to have a reliable estimation of performances and expected lifetime of the tracker. As already described in Chap. 5, in addition to well-known background sources as Touschek and beam-gas, we have a significant contribution from physics processes that happens in the interaction point. The very high luminosity of the machine produces an unprecedented rate for additional pairs and radiative Bhabha processes that, in some areas, is similar or larger than

other traditional background sources. The effect of those physics processes cannot be mitigated optimizing the machine optics, because they scale with the luminosity and the machine goal is always to get the luminosity as highest as possible. In addition, if the particles produced by those physics processes are within the detector acceptance, they cannot be easily shielded, because particles from the interesting physics processes would be stopped as well.

The different sources of background have been simulated with a detailed Geant4-based detector model and beamline description (see Sec. 14.2.1). The detailed simulation is needed because not only the detectors themselves, but also the supporting parts (also referred to as "dead material") play an important role in stopping or creating background particles. Then, the raw output of the simulation has to be processed to obtain useful information that can be used for additional specific simulation of the readout electronics and for test with real particle. Simulated background events can also be sampled and added to relevant physics events to estimate the tracking perfomances in real running conditions, as detailed in Sec. 6.7. Background results can have a significant influence on several aspects of the SVT design, like readout segmentation, electronics shaping time, data transmission rate, and radiation hardness (particularly severe for Layer0).

Add a description of the detector model in Bruno ed insert reference to the main Background sections

Crossing multiplicity, deposited energy distruibution, bandwith, crossing with high number of tracks

Describe main feature of each source

6.6.1 Pair production

6.6.2 Radiative Bhabha

6.6.3 Touschek

6.6.4 Beam Gas

6.6.5 Other sources

Include summary tables with rates, doses, equivalent fluences for various layers

6.7 Detector Performance Studies N.Neri - 6 pages

6.7.1 Introduction

The Super$B$ vertex detector can be considered as the evolution of the BABAR one. It is capable of maintaining adequate performance for time-dependent measurements in presence of a lower boost of the center-of-mass frame (CM) ($\beta\gamma = 0.24$ compared to $\beta\gamma = 0.55$ of BABAR) and much higher background, mainly related to the increased istantaneous luminosity of about a factor 100 higher with respect to BABAR.

The beampipe features a reduced radius of about 1.0 cm which allows the positioning of the innermost layer of the SVT (Layer0) at an average radius of about 1.6 cm. The additional Layer0 measurement along with the low radial material budget of the beampipe (0.42% X_0) and of Layer0 (0.45% X_0), is crucial for improving the decay vertex reconstruction of the B mesons and obtaining adequate proper-time resolution for time-dependent CP violation measurements. In addition, the small size of the luminous region, about $(1\times 1)\,\mu\text{m}^2$ in the transverse plane, also contributes to the improvement of the decay vertex reconstruction when imposing the constraint that the particles are originated from the interaction point. The baseline solution for the Layer0 is based on short strip technology and an upgrade to pixel is foreseen.

In the following we discuss the layout of the SVT and how the design has been optimized in Section 6.7.2, the impact of the Layer0 on detector performance in Section 6.7.3, and the tracking performance in Section 6.7.4. The impact of the machine background on SVT performance is discussed in Sections 6.7.5, 6.7.6 and the performance with a Layer0 pixel detector is presented in Section 6.7.7. In Section 6.7.8 it is described the performance for particle identification based on ionization $\mathrm{d}E/\mathrm{d}x$ in the SVT sensors.

Table 6.4: Reconstrucion efficiencies for $B^0 \to D^{*-}K^+$ decays for different SVT layout (4, 5 ,6 layers) and running conditions (A, B, C). Case A correspond to ideal running conditions, B represents SVT with a damaged module in Layer3 with z hit efficiency of 70%. Case C introduces additional inefficiency with respect to case B in Layer0: 60% hit efficiency for z and ϕ views.

	A eff. (%)	B eff. (%)	C eff. (%)
6 layers	66.0 ± 0.3	65.0 ± 0.3	64.0 ± 0.3
5 layers	64.0 ± 0.3	62.0 ± 0.3	60.0 ± 0.3
4 layers	60.0 ± 0.3	56.0 ± 0.3	53.0 ± 0.3

6.7.2 The SVT layout

The Super*B* SVT is composed by 6 layers of double-sided silicon strip detectors and has a symmetric coverage in the laboratory frame down to 300 mrad (17.2°) with respect to the forward and backward direction, corresponding to 95% angular coverage in the CM. The inner three layers perform the track impact parameter measurements, while the outer layers are necessary for pattern recognition and low transverse momentum (p_t) tracking.

The Layer0 strips are short ('striplets') and oriented at ±45° with respect to the beam direction. The Layer1 to Layer5 silicon strip detectors are very similar to the *BABAR* ones in terms of radial position and strip pitches. The optimization of the strip z and ϕ pitches for the strip detectors is discussed in Section 6.8.2. A dedicated study to optimize the SVT layout as a function of number of silicon sensors and radial positions was performed [3]. Several figures of merit were studied: the track parameters resolution, the reconstruction efficiency and kinematic variable resolutions of B decays with low momentum tracks as $B^0 \to D^{*-}K^+$. Since low momentum tracks do no reach the DCH, they are reconstructed using only SVT information. The *BABAR* experiment has shown that at least 4 hits in the ϕ view and 3 hits in the z view are necessary for robust track reconstruction [2, 5]. The main result is that the 6-layer design is superior and more robust compared to the alternatives investigated, *i.e.* 4- and 5-layer layout where intermediate layers are removed. Indeed, when accounting for possible inefficiencies in hit reconstruction, due to damaged modules or high background, the 6-layer design insures higher reconstruction efficiencies for low momentum tracks compared to the other solutions where intermediate layers are removed.

In Table 6.4 the reconstruction efficiencies are reported for the decay $B^0 \to D^{*-}K^+$ for the 4-, 5- and 6-layer configuration in different running conditions: ideal conditions (A), with a damaged module in Layer3 (B) and with additional hit inefficiency in Layer0 with respect to case B (C). The outer radius of the SVT was ultimately constrained to about 20 cm by the DCH inner radius. It was demonstrated that there is no real advantage in increasing the outer layer of the SVT with respect to the *BABAR* design (14.4 cm) [6, 7, 8]. Moreover, construction cost and technical difficulties would increase. Radial positions of the Layer1 to Layer4 have very little impact on track resolution when comparing a layout with detectors equally separated and the *BABAR*-like layout.

6.7.3 Impact of Layer0 on detector performance

The additional Layer0 measurement is crucial for maintaining adequate resolution on the B^0 meson proper-time difference $\Delta t \simeq \Delta z/(\beta\gamma c)$ in presence of a relatively low CM boost value $\beta\gamma = 0.24$. The average separation Δz between the decay vertex positions of the two B mesons along the z axis is $\Delta z \simeq \beta\gamma c\tau_B = 110$ μm, where τ_B is the B^0 lifetime of about 1.5 ps. Hence, in order to be able to separate the B mesons in Super*B*, their decay positions have to be determined with a significantly better precision than the average separation Δz. In addition in Super*B*, the B vertex separation in the transverse plane, of about 25 μm, is not completely negligible with respect to the average

Δz separation of about 110 μm. It therefore also contributes to the determination of Δt. The reference value for the Δt resolution, $\sigma(\Delta t)$, was determined by the resolution obtained in the *BABAR* experiment according to the Fast Simulation, see Table 6.5. Fig. 6.11 shows the dependence of the per-event error on the physics parameter S as a function of $\sigma(\Delta t)$, with the sensitivity obtained in *BABAR* superimposed. In this simplified model $\sigma(\Delta t)$ corresponds to the width of the core Gaussian of the Δt resolution function. The S per-event error is defined as the error on the parameter S normalized to the number of signal events. S is measured in time-dependent analyses and corresponds to $\sin(2\beta)$ for $B^0 \to J/\psi K^0_S$ decays. The resolution σ_z on

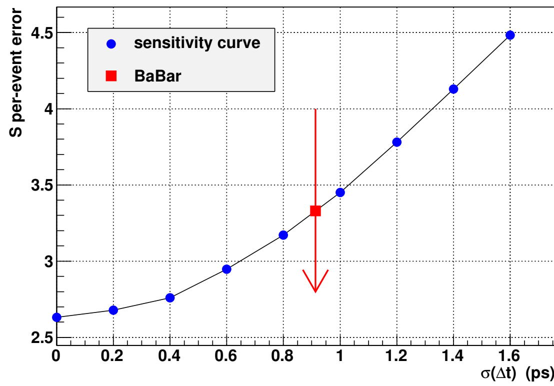

Figure 6.11: The curve represents the dependence of the error on the physics parameter S (*e.g.* $\sin(2\beta)$) as a function of $\sigma(\Delta t)$. The arrow indicates the $\sigma(\Delta t)$ value obtained in *BABAR* according to the Fast Simulation and the square point is the relative value on the sensitivity curve.

the z coordinate of the track depends on the geometry of the vertex detector and the hit resolution. In a simplified model with two hits measured at radii r_0 and r_1 ($r_1 > r_0$) with z hit resolution σ_0 and σ_1 respectively, σ_z can be approximated as:

$$\sigma_z = \frac{\sigma_0^2 + (\sigma_1 r_0/r_1)^2}{1-(r_0/r_1)^2}. \tag{6.1}$$

In addition, the tracks are deflected due to multiple scattering interactions with the material in the tracking volume. The scattering angle distribution can be approximated by a Gaussian with a width given by [33]:

$$\theta_{\mathrm{m.s.}} = \frac{13.6\,\mathrm{MeV}/c}{p_t\beta}\sqrt{\frac{x}{X_0}}\left[1+0.0038\ln\left(\frac{x}{X_0}\right)\right] \tag{6.2}$$

where p_t is the transverse momentum, x is the thickness of the material and X_0 is the interaction length. In order to minimize the uncertainty on σ_z it is important to measure the first hit at r_0 as small as possible with a good hit resolution σ_0. Minimizing the material close to the interaction, *e.g.* the beampipe and Layer0 material budget is also important.

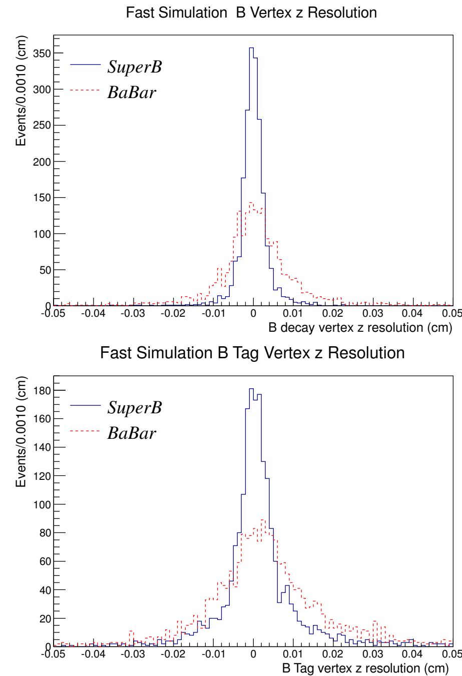

Figure 6.12: B decay vertex z position (top) and B tag z position (bottom) residual distributions in Super$B$ with Layer0 striplets (continuous line) compared with *BABAR* (dashed line) according to Fast Simulation studies.

Table 6.5: RMS of the residual distributions for decay vertex z position for exclusively reconstructed $B^0 \to \phi K^0_S$ decays ($B_{\rm reco}$), inclusively reconstructed B decays ($B_{\rm tag}$), Δz and Δt at Super$B$ and compared with *BABAR* results, according to Fast Simulation studies.

	Super$B$	*BABAR*
$B_{\rm reco}$ (μm)	40 ± 1	105 ± 1
$B_{\rm tag}$ (μm)	100 ± 2	145 ± 2
Δz (μm)	105 ± 2	165 ± 2
Δt (ps)	1.40 ± 0.02	1.45 ± 0.02

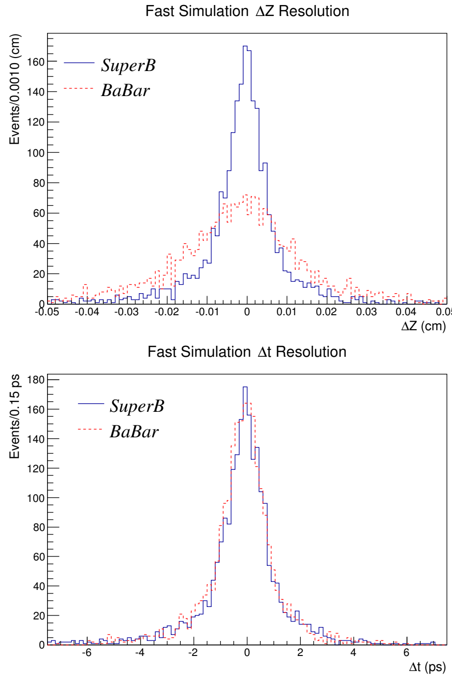

Figure 6.13: Δz (top) and Δt (bottom) residual distributions in Super$B$ with Layer0 striplets (continuous line) compared with *BABAR* (dashed line) according to Fast Simulation studies.

Fig. 6.12 shows the residual distributions of B decay vertex z positions for exclusively (top) and inclusively (bottom) reconstructed B decays. Fig. 6.13 shows the Δz (top) and Δt (bottom) residual distributions. One B is exclusively reconstructed in the $B^0 \to \phi K^0_S$ mode ($B_{\rm reco}$), while the other B is inclusively reconstructed using the remaining tracks of the event and is used also for flavor tagging ($B_{\rm tag}$). The Fast Simulation results for Super$B$ with Layer0 striplets are compared with the *BABAR* ones and summarized in Table 6.5. In Super$B$ we assume $\sigma_0 = 8\,\mu$m for both u and v hits, $r_0 = 1.60\,$cm and $x/X_0 \simeq 0.9\%$ including the beampipe and Layer0 striplets material budget. For striplets detectors, u and v coordinates are oriented at $\pm 45°$ with respect to the z axis and are perpendicular to each other. In *BABAR* we have $\sigma_0 = 14\,\mu$m for the z hits and $10\,\mu$m resolution for the ϕ hits, with $r_0 = 3.32\,$cm and $x/X_0 \simeq 1.6\%$. In Super$B$, the improved Δz resolution is compensated by the reduced boost value, yielding a Δt resolution very similar to *BABAR*. In Fig. 6.14 is shown the Δt resolution obtainable with different Layer0 radii (r_0= 1.4 and 1.6 cm) and material budgets (x/X_0 ranging from 0.1 to 1.0%). The dashed line represents the reference value of *BABAR*.

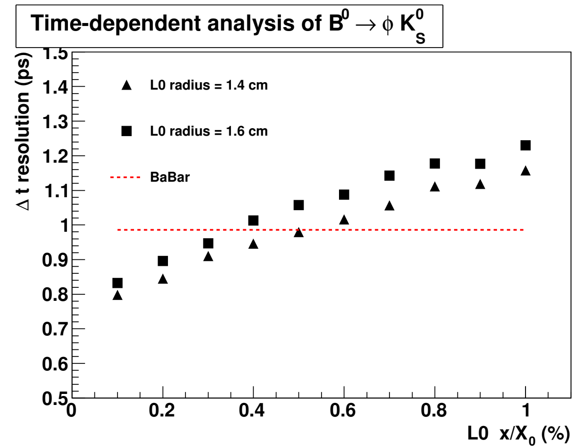

Figure 6.14: Resolution on Δt for different Layer0 configurations in terms of radius (r_0 = 1.4 and 1.6 cm) and material budget ($x/X_0 = 0.1 - 1.0\%$) compared with the reference value of *BABAR* (dashed line).

The impact of the hit resolution on the decay vertex reconstruction has also been studied. With 8 μm hit resolution in both views of Layer0, the error on the vertex position due to multiple scattering interactions with the material dominates the overall vertex uncertainty. Even for high momentum tracks from $B^0 \to \pi^+\pi^-$ decays. Hence, without further reduction of the material budget, there is no real advantage in improving the hit resolution with respect to this value. The hit resolution from Layer1 to Layer5 has been chosen according to the *BABAR* SVT design which was optimized for low momentum track reconstruction. The intrinsic detector hit resolution and hit efficiency values used in the Fast Simulation are reported in Table 6.6 for the different SVT layers.

Table 6.6: Intrinsic detector hit resolution and hit efficiency for the z and ϕ sides (Layer0 u and v sides) for the different layers.

	res. u (μm)	res. v (μm)	eff. u (%)	eff. v (%)
Layer0	8	8	99	99
	res. z (μm)	res. ϕ (μm)	eff. z (%)	eff. ϕ (%)
Layer1	14	10	98	98
Layer2	14	10	98	98
Layer3	14	15	98	96
Layer4	25	15	99	98
Layer5	25	15	99	98

6.7.4 Tracking performance

The tracking performance at Super*B* has been studied considering alternative solutions for the SVT and DCH layout [3, 6, 7]. In particular we have studied alternative SVT configurations: with different values of the SVT outer radius (from about 14 to 22 cm), without Layer2 detector, different radial positions of the layers (*e.g.* uniform distance between layers), different hit resolutions accounting for variations of about 50% with respect to the nominal ones reported in Table 6.6. The main result was that the *BABAR*-like layout for Layer1-Layer5 was very close to be the optimal choice in terms of resolution for track parameters. Small improvements in track parameter resolution would have been possible by removing Layer2. On the other hand, the 6-layer layout has been proved to be more robust against possible problems that might cause loss of efficiency in some layers of the detector [3] and was preferred for this reason. Optimization of the strip pitches for the z and ϕ sides of the different layers are discussed in Section 6.8.2. Fig. 6.15 shows the resolution on the impact parameter d_0, as a function of p_t with the *BABAR* and Super*B* detectors. The d_0 is defined as the distances of the point of closest approach of the track to the z-axis from the origin of the coordinate system in the xy plane. Results for alternative configurations of the SVT layout, with extended outer radius, with DCH lower radius, and without Layer2, are also shown. A significant improvement in the d_0 resolution of about a factor 2 is achieved with the Super*B* detector with respect to the *BABAR* one. The alternative SVT layout options investigated give consistent results with the nominal Super*B* solution.

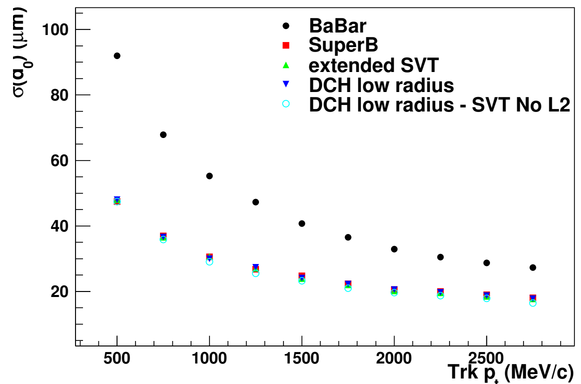

Figure 6.15: Resolution $\sigma(d_0)$ on the impact parameter d_0 as a function of p_t in *BABAR* and for various Super*B* tracking detector configurations.

Table 6.7: Resolutions on the time of arrival of the hit for the z and ϕ sides (Layer0 u and v sides) for the different layers with selected peaking times. The "old" detector correspongs to the same detector after 7.5 years of running and includes a safety factor of 5 times the level of radiation with respect to the nominal one.

	shaper peak. time (ns)	time res. "fresh" det. (ns, ns)	time res. "old" det. (ns, ns)
Layer0	25	(9.7, 9.7)	(9.7, 9.7)
Layer1	75	(10.7,10.2)	(11.0,10.8)
Layer2	100	(11.4,12.4)	(12.0,11.5)
Layer3	150	(12.4,11.7)	(15.1,14.1)
Layer4	500	(28.8,24.2)	(49.4,41.6)
Layer5	750	(42.6,34.3)	(54.6,46.7)
Layer4	250	(17.8,15.9)	(18.7,16.6)
Layer5	375	(24.9,20.5)	(25.5,21.2)

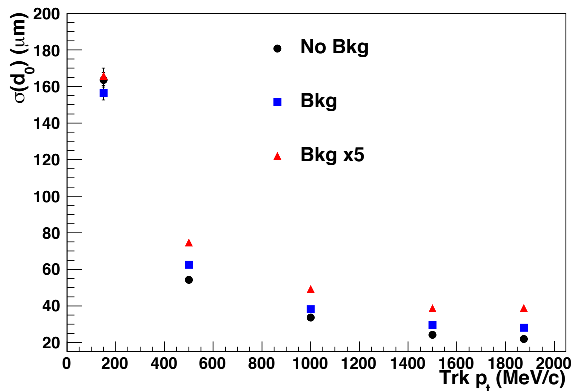

Figure 6.16: Resolution on the impact parameter of the track d_0 as a function of p_t for the Super$B$ detector with Layer0 striplets. The results shown assume no background (points), nominal background (squares) and 5 times the nominal background (triangles).

6.7.5 Impact of machine background on tracking performance

The background conditions will be more severe in Super$B$ than in *BABAR*, as described in Section 6.6. The fast front-end electronics of the SVT provides very good resolution on the time of passage of the particle or time of arrival of the hit. The Time over Threshold (ToT) of the shaper output is used to correct for the time between the time of arrival of the hit and the time the shaper exceeds threshold. The resolution on the time of arrival of the hit depends on the SVT layer due to the different shaper peaking times of the front-end electronics, and has been estimated using 'ad hoc' simulations. Several peaking times will be available on the strip readout chips, as summarized in Table 6.13. The resolution for all layers and sides is reported in Table 6.7 for the nominal peaking-time configuration and for the shortest peaking times in Layer4 and Layer5. It ranges from about 10 ns for Layer0 up to 50 ns for Layer5. In our studies, hits outside a $\pm 5\sigma$ acceptance time window from the event time (determined by the DCH) are discarded. A similar procedure was used in the reconstruction program of the *BABAR* experiment.

The Fast Simulation tool does not apply any pattern recognition algorithm. Tracking performance is based on parameterizations tuned on *BABAR* measured performance. Hits from neighboring tracks may be merged or associated to wrong tracks, but all generated tracks are reconstructed and no fake tracks are added. This fast simulation tool allows to study track parameter resolution, but not the tracking efficiency. The impact of the background on the resolution of the track impact parameters is shown in Fig. 6.16. In order to address the issue of the pattern recognition capability to reconstruct tracks in the high background environment of Super$B$, SVT detector occupancies estimated in Super$B$ have been compared to those observed in *BABAR*. In particular we compared the cluster occupancy, defined as the detector hit occupancy after applying the time window cut, divided by the hit multiplicity in a cluster. The average cluster occupancy over all layers and sides is estimated to be about 0.3% with

nominal background in Super$B$. This cluster occupancy in Super$B$ is smaller than the maximal value of about 0.7% reached at high luminosity in BABAR, thanks to the improved hit time resolution. When considering a scenario with an additional $\times 5$ safety factor on background predictions for Super$B$, the estimated average cluster occupancy is about 1.8% with nominal peaking-time configuration and about 1.5% with the shortest peaking times in Layer4 and Layer5. BABAR studies [10] of SVT performance in high background conditions have been used to estimate the efficiency to assign a hit to a track as a function of the cluster occupancy, that was found to be greater than 95% up to a 3% occupancy [11]. These studies indicate that the pattern recognition should be able to work without major problems also in presence of 5 times the nominal background. Moreover, for low momentum tracks not reaching the DCH, the additional Layer0 measurements should help the pattern recognition when using SVT hits only. Improvements in the pattern recognition algorithm may also be foreseen with respect to what has been used in BABAR.

6.7.6 Sensitivity studies for time-dependent analyses

The sensitivity to the physics parameter S has been considered as figure of merit for time-dependent analyses of B^0 decays. Several decay modes have been studied: $B^0 \to \phi K^0_S$, $B^0 \to \pi^+\pi^-$, $B^0 \to J/\psi K^0_S$, $B^0 \to D^+D^-$, but also decay modes such as $B^0 \to K^0_S K^0_S$, $B^0 \to K^0_S \pi^0$ where the impact of the additional Layer0 measurement is less effective due to the presence of neutral and long-lived particles in the final state. The per-event error on the S parameter estimated in Super$B$ with the Fast Simulation is consistent with what is observed with the BABAR detector for all decay modes but for $B^0 \to K^0_S K^0_S$ and $B^0 \to K^0_S \pi^0$ decays, where a reduction in sensitivity of about 15% is observed [6, 8]. Only the impact of the Δt resolution on the measurements has been included in the Fast Simulation studies. In particular, possible improvements on the reconstruction efficiency, 95% angular coverage in the CM frame with respect to 91% in BABAR, and better flavor tagging performance due to improved particle identification, have not been considered in these studies.

In the case of time-dependent analyses for mixing and CP violation in the neutral D meson system, the determination of the proper time t relies on the measurement of the 3-dimensional flight length ($\vec{L}$) and the momentum $\vec{p}$ of the D^0 according to $t = \frac{\vec{L}\cdot\hat{p}\ M}{|\vec{p}|}$ where M is the D^0 nominal mass. D^0 mesons produced in $e^+e^- \to c\bar{c}$ events gain a natural boost in the reaction. Even though the CM boost is reduced with respect to BABAR, the resolution on the D^0 proper time in Super$B$ is about 2 times better [9]. In Fig. 6.17 is reported the distribution of the D^0 proper-time error in Super$B$ and compared with BABAR. The average proper-time error is about 0.16 ps in Super$B$ and 0.30 ps in BABAR for $D^0 \to K^0_S \pi^+\pi^-$ decays, to be compared with the D^0 lifetime of about 0.41 ps.

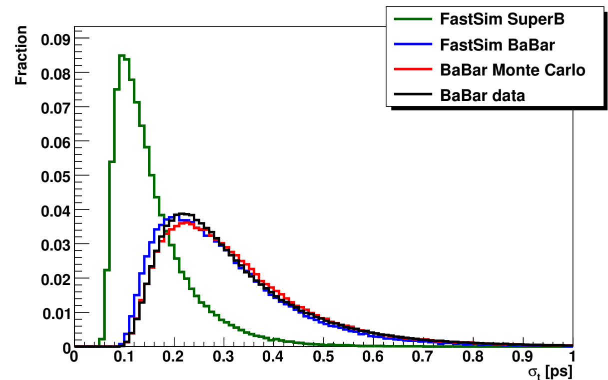

Figure 6.17: D^0 proper-time error distributions obtained with the Super$B$ (green line) and the BABAR (blue line) detectors according to Fast Simulation studies. Distributions from BABAR Monte Carlo (red line) and data (black line) are also reported in the plot.

The impact of machine background events on the SVT performance has been studied by adding background hits to signal events accord-

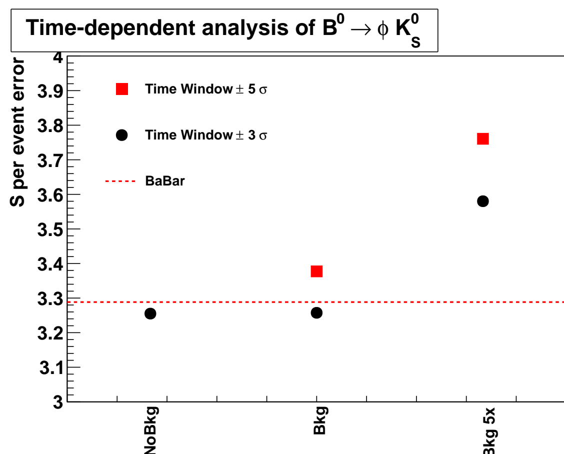

Figure 6.18: Variation of the S per-event error in $B^0 \to \phi K^0_S$ time-dependent analysis in presence of nominal background events and with 5 times the nominal background. A cut on the time of arrival of the hits has been applied at $\pm 3\sigma$ and $\pm 5\sigma$ with respect to the time of the event.

ing to the rates estimated using Full Simulation. Details on the estimates of the machine background events can be found in Section 6.6. Background hits may reduce the hit reconstruction efficiency, increase the effective hit resolution, and reduce the efficiency of pattern recognition for charged tracks, along with the increase of fake tracks. Most of the above effects have been included in our Fast Simulation assuming that the charged track pattern recognition algorithm will work with similar performance to the *BABAR* one, but fake tracks are not simulated. Hit efficiency of the readout chips used in the Fast Simulation studies can be found in Table 6.13 for the case of nominal background and with 5 times the nominal background. In Fig. 6.18 is reported the impact of the machine background events on the physics parameter S for the case of nominal background and with 5 times the nominal background rates. Background hits are rejected if they are not within a time window of $\pm 3\sigma$ ($\pm 5\sigma$) with respect to the time of the event. The reduction of the sensitivity to S is quite limited with nominal background ($< 3\%$) and is about 9% (14%) with 5 times the nominal background conditions when applying a $\pm 3\sigma$ ($\pm 5\sigma$) time window cut.

6.7.7 Performance with Layer0 pixel detectors

A Layer0 technology based on a high granularity silicon pixel sensor, *e.g.* with $50 \times 50\ \mu m^2$ cell, is considered for an upgrade of the baseline striplets solution. The different Layer0 technology options are described in Sec. 6.12 and are based on hybrid pixels, deep N-well CMOS monolithic sensors and monolothic pixels with CMOS quadruple well. All these solutions adopt a digital sparsified readout with the area of the pixel cell of about $2500 - 3000\,\mu m^2$. The shape of the pixel can be optimized in such a way to reduce the sensor pitch in the z direction and to improve the relative hit resolution while keeping the pixel area constant.

As already discussed in Sec. 6.7.3, the determination of the decay vertex position is driven by the performance of Layer0. The advantage of the Layer0 pixel solution is to guarantee good detector performance also in presence of relatively high background. The detector occupancy, defined as the probability of having a noise hit in the sensitive time window, is about two orders of magnitude lower with respect to the striplets case, taking into account the different detector granularity and resolution on the time of arrival of the hits. Occupancies at the level of $10^{-4} - 10^{-3}$ in a Layer0 pixel detector would correspond to occupancies of $10^{-2} - 10^{-1}$ with the striplets solution, which are about the highest achievable values in the Layer0 striplets at Super$B$. Therefore, the impact of the the background hits on the determination of the decay vertex and of the track impact parameters can be safely assumed to be negligible at Super$B$ with a Layer0 pixel solution.

Fig. 6.19 shows the sensitivity to the S parameter in time-dependent CP violation analysis of $B \to \phi K^0_S$ decays as a function of the Layer0 radius (r_0 =1.4 and 1.6 cm) and of its

material budget ($x/X_0 = 0.1-1.0\%$), in case of nominal background and $\times 5$ the nominal background. The dashed line represents the reference value obtained in BABAR. Material budget in the range $x/X_0 = 0.35-0.50\%$ ($x/X_0 = 0.55-0.85\%$) is achievable for a Layer0 pixel solution based on CMOS monolithic active pixel sensors (hybrid pixels) depending on the results of the ongoing R&D activities. The S sensitivity is very similar to the one obtained in BABAR. The maximal difference is about 6% (10%) in the worst case considered (including 5 times the nominal background).

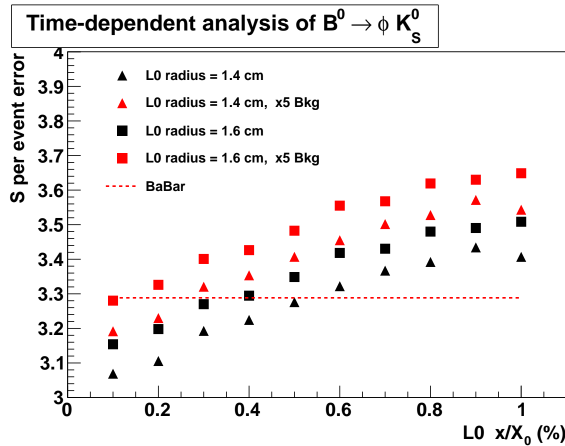

Figure 6.19: S per event error in $B^0 \rightarrow \phi K_S^0$ time-dependent analysis for different Layer0 radii ($r_0 = 1.4$ and 1.6 cm) and material budget ($x/X_0 = 0.1-1.0\%$) compared with the reference value of BABAR (dashed line). Results in presence of 5 times the nominal background are also reported in the plot.

6.7.8 Particle identification with dE/dx

The measurement of the ToT value by the front-end electronics enables one to obtain the pulse height, and hence the ionization dE/dx in the SVT sensors. The dynamic range of the analog readout is about 10-15 times the value corresponding to minimum ionizing particles, which is sufficient to take advantage of the dE/dx capability of the SVT [12].

Each sensor will provide 2 measurements of dE/dx, one for each sensor side, for a total of 12 dE/dx measurements in the SVT. In BABAR, where a total of 10 dE/dx measurements (5 layers) were available, for every track with signals from at least four sensors in the SVT, a 60% truncated mean dE/dx was calculated. The cluster with the smallest dE/dx energy was also removed to reduce sensitivity to electronics noise. For MIPs, it was abtained a resolution on the truncated mean dE/dx of approximately 14%.

The intrinsic smearing from the distribution of the energy deposition in the silicon sensors and from the atomic binding effects in the silicon will dominate the uncertainty on the measured dE/dx [12]. The contribution to the dE/dx uncertainty from the electronic noise should be relatively small. Therefore the resolution on dE/dx for MIPs is expected to be similar to the one achieved in BABAR. However, the dE/dx precision is inversely proportional to the square root of the number of dE/dx samples used for the truncated dE/dx mean calculation [13]. Two additional measurements in the Layer0 should improve the average resolution of a factor $\sqrt{5/6} = 0.9$, where 5 is the average number of dE/dx samples used in BABAR and 6 is the expected average number in Super$B$. The e/π separation is expected to be larger than 3σ for momenta lower than 150 MeV/c and will be very useful for rejecting low momentum electrons from background QED processes.

6.8 Silicon Sensors L. Bosisio - 8 pages

Layers 1 to 5 of the SVT will be based on 300 μm thick double-sided silicon strip detectors, with integrated AC-coupling capacitors and polysilicon bias resistors. These devices are a technically mature and conservative solution to the requirements the SVT must meet to provide precise, highly segmented tracking near the interaction point. For the new Layer0, the baseline

option also foresees double-sided silicon strip detectors, with short strips ('striplets'), 20 mm long, oriented at ± 45 degrees from the beam direction, fabricated on 200 μm thick substrates. The detailed requirements which the detectors must meet are discussed below.

6.8.1 Requirements

Material budget. To achieve good vertex resolution, it is especially important to minimize the material up to and including the first measurement. This requirement, and the need to provide precise vertexing in both z and ϕ, leads to the choice of double-sided detectors. Given the increased module length with respect to the *BABAR* SVT, in order to minimize the number of sensors required, the complexity of the assembly and the insensitive area between adjacent sensors – and to ease the alignment task – we foresee to have the sensors fabricated on 150 mm diameter wafers, which is by now an available option from several sensor suppliers. For Layers 1 to 5 we plan to use 300 μm thick silicon wafers, which are a standard choice and present acceptable handling properties. For Layer0, given the very stringent limitations on the amount of material, we will be forced to go to 200 μm thick substrates. Processing double sided sensors on thin, 150 mm diameter wafers is a significant challenge, which very few manufacturers are willing to tackle. Unfortunately, while the other layers could also be assembled from smaller sensors, fabricated on 100 mm wafers, Layer0 sensors do not fit inside 100 mm wafers. This is due to the requirement to have only one sensor per Layer0 module, which in turn is dictated by the need to avoid insensitive regions and mechanical support structures, and also by limitations on the available number of readout channels. These difficulties are mitigated by the very small number of Layer0 sensors required and the fact that five of them can comfortably fit into a single 150 mm wafer. Because of this, a low fabrication and assembly yield can be tolerated for Layer0 sensors.

Efficiency. The silicon detectors must maintain high single-point efficiency in order to achieve the requirements given in Section ?? for high overall track reconstruction efficiency. Loss of efficiency can occur from defective sensor strips, from bad interconnections, or from faulty electronics channels. Sensor related inefficiencies can be due to fabrication defects or handling damage, which can result in strips with high leakage currents, poor insulation or broken AC-coupling capacitor. Our goal is to achieve an overall single-detector strip failure rate of less than 1%. The experience gained from from a large production of double-sided AC-coupled detectors for the ALICE Inner Tracking System indicates that a total rate of defective strips below 1% can be achieved with reasonable yield ($> 70\%$).

Resolution. As described in Section xxx, we have determined from Monte Carlo simulations [xxx] that the intrinsic point resolution should be 15 μm or better in both z and ϕ for the inner layers. These are the point resolutions for tracks at near-normal incidence. As the angle between the track and the plane normal to the strip increases, the resolution degrades. We require the resolution to degrade by no more than a factor of approximately 3 for angles up to 75° ($\lambda \sim 1.3$) from normal.

Radiation hardness. A further requirement is that the sensor values hold up to an integrated dose of $\sim$2 Mrad of ionizing radiation (electromagnetic in origin). This requirement leads to the use of AC-coupled detectors in order to avoid the problems associated with direct coupling of the large leakage currents which can occur at such large doses. It also has implications in the choice of the strip biasing scheme and on .

6.8.2 Sensor design and technology

From the above requirements and from the discussion in Sections xxx, we have arrived at the detector specifications and design parameters which are described in this section.

Substrate and implant type. The wafers will be n-type, with a resistivity in the range 4–8 kΩ cm, corresponding to a depletion voltage of 40 to 80 V. These values seem to be a reason-

Table 6.8: Physical dimensions, number of strips and pitches for the nine different sensor models. Model VI has a trapezoidal shape.

Sensor Type	0	I	II	III	IVa	IVb	Va	Vb	VI
Dimensions (mm)									
z Length (L)	105.2	111.7	66.4	96.4	114.6	119.8	102.2	106.0	68.0
ϕ Width (W)	15.1	41.3	49.4	71.5	52.8	52.8	52.8	52.8	52.8-43.3
Thickness	0.20	0.30	0.30	0.30	0.30	0.30	0.30	0.30	0.30
PN junction side reads	u	z	z	ϕ	ϕ	ϕ	ϕ	ϕ	ϕ
Strip Pitch (μm)									
z (u for Layer0)	54	50	50	55	105	105	105	105	105
ϕ (v for Layer0)	54	50	55	50	50	50	50	50	$50 \rightarrow 41$
Readout Pitch (μm)									
z (u for Layer0)	54	100	100	110	210	210	210	210	
ϕ (v for Layer0)	54	50	55	100	100	100	100	100	$100 \rightarrow 82$
Number of Readout Strips									
z (u for Layer0)	1536	1104	651	865	540	565	481	499	318
ϕ (v for Layer0)	1536	799	874	701	512	512	512	512	512

able compromise between the need to limit the depletion voltage and the peak electric fields on one hand and on the other hand the desirability of delaying type inversion in the presence of radiation damage.

We will employ p^+ strips on the junction side and n^+ strips on the ohmic side, with p^+-blocking implants in between; see Figure xxx for a cross-sectional view. This choice has proven to be a mature, reliable technology xxx], requiring no R&D.

Coupling to preamplifier. The strips are connected to the preamplifiers through a decoupling capacitor, integrated on the detector by interposing a dielectric layer between the p or n-doped strip and the metal strip. AC coupling prevents the amplifier from integrating the leakage current with the signal; handling high leakage currents due to radiation damage imposes an additional burden on the preamplifier design and has other undesirable operational implications. On each sensor, the value of the decoupling capacitance must be much larger than the total strip capacitance on the same sensor, a requirement which is rather easily met by the fabrication technologies in use.

Bias resistors. We plan to use polysilicon bias resistors, because the alternative biasing method by exploiting the punch-through effect does not offer adequate radiation tolerance. The bias resistors values will range between 4 and 15 MΩ, depending on the layer. The choice of the R_B value is constrained by two requirements. A lower limit is determined by the need to limit the noise contribution, which has a $\sqrt{\tau/R_B}$ dependence, and if several strips are ganged together the effective resistance is correspondingly decreased. The requirement that, for floating strips, the product $R_B \cdot C_{TOT}$ must be much larger than the amplifier peaking time in order to allow for capacitive charge partition is fulfilled with ample margin for any reasonable values of R_B. An upper limit to R_B is dictated by the allowable potential drop due to the strip leakage current, which depends mainly on the irradiation level and decreases going from inner to outer layers. The maximum resistance value is also limited in practice by the need to limit the area occupied on the wafer. Values of 40 kΩ/square for the sheet resistance of polysilicon can be achieved. Thus, it is possible to

Table 6.9: Number of the different sensor types per module, area of the installed sensors, number of installed sensors and number of sensors including spares. Spare sensors include one spare module per module type (two for Layer0), plus additional sensors accounting for possible losses during the whole SVT assembly process.

Sensor Type	0	I	II	III	IVa	IVb	Va	Vb	VI	All
Layer0	1	-	-	-	-	-	-	-	-	1
Layer1	-	2	-	-	-	-	-	-	-	2
Layer2	-	-	4	-	-	-	-	-	-	4
Layer3	-	-	-	4	-	-	-	-		4
Layer4a	-	-	-	-	4	-	-	-	2	6
Layer4b	-	-	-	-	-	4	-	-	2	6
Layer5a	-	-	-	-	-	-	6	-	2	8
Layer5b	-	-	-	-	-	-	-	6	2	8
Silicon Area (m^2)	0.013	0.055	0.079	0.167	0.194	0.203	0.291	0.302	0.222	1.52
Nr. of Sensors	8	12	24	24	32	32	54	54	68	308
Nr. Including Spares	20	20	40	35	44	44	72	72	92	439

fabricate a 10 MΩ resistor with a 6 μm-wide, 1500 μm-long polysilicon resistor. With a suitable shaping of the polysilicon line, the space required by the resistor will be less than 200 μm at 100 μm pitch (corresponding to strips at 50 μm pitch with resistors placed at alternate ends). A final requirement is that the bias resistor be quite stable for the expected radiation doses.

Considering the space needed to accommodate the biasing resistors and to gracefully degrade the electric field close to the edge with a guard ring structure, we specify the active region of the detectors to be 1.4 mm smaller than the physical dimensions, that is, the dead region along each edge has to be no more than 700 μm wide. This is the same specification chosen for the *BABAR* strip detectors and, although stricter than adopted by most silicon sensor designs, has proven to be feasible without difficulty, thanks to the choice of placing the polysilicon resistors in the edge region outside the guard ring. For Layer0 sensors, which have a reduced thickness of 200 μm and smaller value, shorter bias resistors, we specify a 600 μm wide inactive edge region.

Optimization of z and ϕ readout strips. *(This paragraph still needs to be rewritten.)* A major issue is which side of the detector (junction or ohmic) should read which coordinate (z or ϕ). The capacitance, and consequently, the noise is somewhat smaller on the junction side than on the ohmic side, and the strip pitch on the junction side can be 25 μm, while on the ohmic side, it is limited to about 50 μm because of the presence of the p-stop implant. For these reasons and because the z vertex measurement is more important from the point of view of physics, we use the junction side for the z strips on the inner layers. The better performance of the junction side also helps compensate for the additional resistance and capacitance imposed by the longer z fanout circuit.

In order to maintain acceptable signal-to-noise ratios for tracks at large dip angles, we employ a 100 μm readout pitch for these z strips with one floating strip in between every two readout strips. We have considered using a wider readout pitch, for example, 200 μm for the very forward and backward regions in order to increase the signal at large dip angles. However, this would involve yet another detector design, and based on our present estimates of achievable electronic noise, it does not appear to be necessary.

Table 6.10: List of different mask sets for 150 mm wafers, specifying the content of each wafer layout, the minimum value of the distance between the sensors and the wafer edge, the number of wafers required for each design and the total number of wafers. The numbers quoted include the spare sensors, but not the fabrication yield.

Mask Design	Wafer content	Min. Clearance to Wafer Edge (mm)	Number of Wafers
A	5×Mod 0	10.2	5
B	Mod I + Mod VI	8.2	20
C	Mod III	15.0	35
D	Mod IVa	11.9	44
E	Mod IVb	9.5	44
F	Mod Va + Mod VI	9.8	72
G	Mod Vb + Mod II	6.9	72
Total			287

Acceptable resolution can be obtained for the ϕ strips on the inner layers using the ohmic side. Two solutions are possible; either a 50 μm readout pitch without floating strips, since there is no room for them on the ohmic side, or a 100 μm readout pitch with one floating strip. Either solution is feasible, and they should give roughly equivalent position resolution for single tracks. Double-track resolution is better for the first solution, and the noise contribution due to detector leakage currents is doubled in the latter solution. Therefore, preference goes to a 50 μm readout pitch without floating strips. Although this choice has twice as many readout channels, the cost implications are not very important because the electronics cost is dominated by the development effort and consequently the per channel incremental cost is not significant.

The physical dimensions, strip numbers and pitches for the various sensor models are listed in Table 6.8.

6.8.3 Wafer layout and quantities

Table 6.9 reports the sensor composition of the different detector modules, the number of installed sensors of each type, with the corresponding silicon areas, and the total numbers of sensors including spares. Spare sensors account for one spare module of each type (two for Layer0), plus an additional 20% to compensate for possible losses during the assembly process. We see that the current design employs nine different types of sensors, for a total of 308 installed sensors covering 1.52 m^2. Using 150 mm diameter wafers and a dedicated sensor model for each module type allows to cover the $\sim$ 1.5 times larger area with a smaller number of sensors with respect to BABAR, at the expense of having nine different models of sensors. However, through optimized usage of the wafer area it is possible to accommodate all nine sensor types in seven different wafer layouts, i.e. seven mask sets, and to fabricate all 439 sensors (spares included) on 287 wafers. This is illustrated in Table 6.10.

6.8.4 Prototyping and tests

(This paragraph still needs to be written.) ... for the electrical parameters one can see Table 6.11

6.8.5 z-side strip connection options

On z-side, the readout pitch is set to 100 μm in Layers 1 and 2, 110 μm in Layer3 and 210 μm in Layers 4 and 5, with a ‘floating’ strip in between, to improve spatial resolution for particle tracks with large incidence angles. Since the number of readout strips exceeds the number of available electronic channels, it is necessary to ‘gang’ together up to three (depending on the

Table 6.11: Electrical parameters for the different detector models *(Numbers to be updated)*.

Detector Model	z (u for model 0) readout Side			ϕ (v for model 0) readout Side		
	C_{strip} (pF/cm)	C_{AC} (pF/cm)	R_{series} (Ω/cm)	C_{strip} (pF/cm)	C_{AC} (pF/cm)	R_{series} (Ω/cm)
0	2.5	40	4	2.5	30	8.5
I	1.7	40	5	2.5	30	9
II	1.7	40	4	2.5	30	7
III	1.7	30	7	1.7	40	4
IVa	1.7	60	3	1.7	40	4
IVb	1.7	60	3	1.7	40	4
Va	1.7	60	3	1.7	40	4
Vb	1.7	60	3	1.7	40	4
VI	1.7	60	3	1.7	30	4.5

SVT layer) strips. This 'ganging' scheme connects two or three far apart strips to the same readout channel (Fig. 6.20), thus preserving the strip pitch at the expense of a higher capacitance and series resistance (resulting in higher noise), plus ambiguities in the hit position. For tracks at small θ angles with respect to the beam direction (that is, large incidence angles on the sensor), the signal-to-noise ratio is further degraded by the fact that a track traverses several z-strips (up to nine in the inner layers) and the signal becomes approximately proportional to the strip readout pitch (only 1/3 the wafer thickness in Layers 1 to 3). This suggest adopting an alternative connection scheme, in which two (or more, at large incidence angles) *adjacent* strips are bonded to a single fanout trace, effectively increasing the strip pitch and the signal into a readout channel, with a less than proportional increase in capacitance, and no increase in series resistance. We call this connection scheme 'pairing'.

At small θ angles, this gives better S/N and, consequently, higher detection efficiency when compared to individually connected strips. The improvement is even more important in comparison to the 'ganging' scheme, where the strip capacitance is proportional to the number of strips ganged together, but the signal remains that of a single strip. Moreover, for paired strips also the fanout capacitance and resistance can be made lower, because of the larger trace pitch.

Due to the lower noise, at small θ angles pairing is also expected to give better spatial resolution with respect to ganging. In order to avoid a significant increase of the input capacitance, pairing will be made between the 'readout' strips (at 100 μm pitch) so that a 'floating' strip is always present *between* two adjacent groups of paired strips. However, we are evaluating the option of connecting also the intermediate (otherwise floating) strips *within* a group of paired strips, as shown by the 'upper' bonds in Fig.xxx.

Strip capacitance measurements performed on test sensors (Ref. xxx) confirm that pairing yields significantly lower capacitance with respect to ganging the same number of strips; the advantage in capacitance of pairing with respect to ganging increases for higher pairing/ganging multiplicity. The additional increase in total capacitance when connecting also the intermediate strips is 4−5% on p-side, $\sim$ 6% on n-side. In front of this, a better signal collection efficiency is expected.

6.9 Fanout Circuits L.Vitale - M.Prest2+2 pages

(Layer0 will be treated separately from the other ones)

6.9.1 Fanouts for layer0

6.9.1.1 Requirements

6.9.1.2 Technology

6.9.1.3 Design

6.9.1.4 Prototyping and tests

6.9.2 Fanouts for outer layers

6.9.2.1 Requirements

The requirements will be fixed by the detector designs. From the production point of view, the minimum line width is 15 μm with a space between the lines of 15 μm. With the present technology, it is not possible to go below these numbers. No constraints are present on the fanout length given the same machines used for the micropattern gas detector production will be used.

6.9.2.2 Material and production technique

The BaBar fanouts were produced on 50 μm Upilex (by UBE) with a deposit of 150 nm of Cr, 4.5 μm of copper followed by a layer of 150 nm of Cr and 1.5 μm of amorphous gold. The SuperB SVT fanouts will be produced on a similar material by UBE (50 μm of polyamide with 5 μm of copper directly deposited on the base material) which should ensure less defects and thus a better yield. This material will be tested in the prototype phase. The old Upilex is anyway still available if the new material would prove not adequate.

A new technique for the production will be implemented in order to reduce the production times. In the BaBar production line, the photoresist was impressed through a mask after its being deposited on the Upilex requiring to work in a clean room. For SuperB, the idea is to impress the photoresist directly with a laser; this means the photoresist is solid and allows to complete the procedure in a much faster way. This technique has already been tested on the same pitches foreseen for the SVT fanouts.

The increase in the production speed allows to repeat the production of pieces with defects without delaying the SVT assembly. All the pieces will be gold plated with 1.5 μm of amorphous gold for the bonding.

6.9.2.3 Design

The design will follow the same rules of the BaBar fanouts adapting it to the different length of the modules. Differently from the BaBar pieces, no test-tree is foreseen (see next section). To allow the gold plating, all the lines will be shorted. A suitable cutting device will be developed to cut the shorting line after the visual inspection.

Table 6.12 summarizes the geometrical parameters as well as the number of readout strips and channels, the typical pitch and the total number of required circuits per layer and type.

Fig. 6.20 presents a sketch of the ganging principle proposed for the design of layers z 3-4-5.

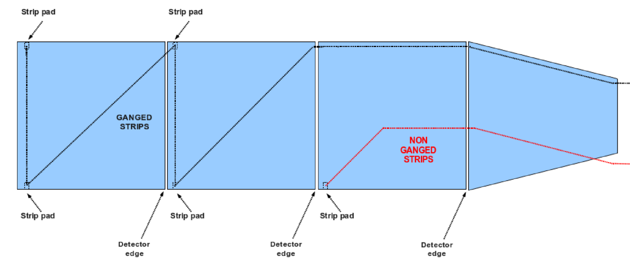

Figure 6.20: Schematic view of two z strips ganged through the fanout circuit.

6.9.2.4 Tests and prototyping

All the fanouts will be automatically optically checked by a dedicated machine which will use the gerber files of the fanouts to find shorts or open lines. The machine can work with 25 μm lines. The region with smaller lines (15 μm with a 15 μm space) corresponding to the bonding area (1.5 mm long and around 6 mm wide) will have to be controlled manually.

Given the much shorter time needed for the production, no correction is foreseen for shorts or open lines; the damaged pieces will be produced again. On the other hand, if a short is

Table 6.12: Summary of fanout circuit characteristics.

Layer	Fanout Type	Length (mm)		Number of Readout		Typical Pitch at (μm)		Number of Circuits
		Left	Right	Strips	Channels	Input	Output	
1	z	200.5	196.5	1104	896	100	45	12
	ϕ	93.82	89.82	799	896	50	45	12
2	z	196.501	200.501	1302	896	100	45	12
	ϕ	68.611	72.611	874	896	55	45	12
3	z	242.485	242.485	1730	1280	110	45	12
	ϕ	54.635	54.635	701	1280	100	45	12
4a	z	326.538	322.538	1398	640	210	45	16
	ϕ	34.563	30.563	512	640	82	45	16
4b	z	326.536	322.536	1448	640	210	45	16
	ϕ	23.826	19.826	512	640	82	45	16
5a	z	401.267	405.266	1761	640	210	45	18
	ϕ	31.747	35.746	512	640	82	45	18
5b	z	401.266	405.266	1815	640	210	45	18
	ϕ	20.346	24.346	512	640	82	45	18

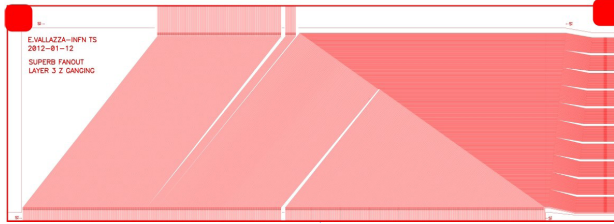

Figure 6.21: Design of a z fanout prototype of layer 3.

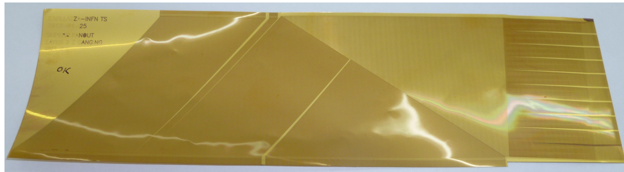

Figure 6.22: Picture of the prototype of the layer 3 z.

present in the larger pitch region, the same correction procedure used for BaBar (involving the use of a microprobe) can be implemented.

As far as the tests are concerned, a batch of fanouts will be produced starting from the BaBar design to check the whole production and test chain. These fanouts in principle can be used with working detectors to test also the assembly procedures.

Figure 6.21 shows the design of a z fanout prototype of layer 3. These prototypes were also used to measure the typical capacitance and resistance.

Figures 6.22 and 6.23 show a picture of the prototype of the layer 3 z and a step of the cutting procedure.

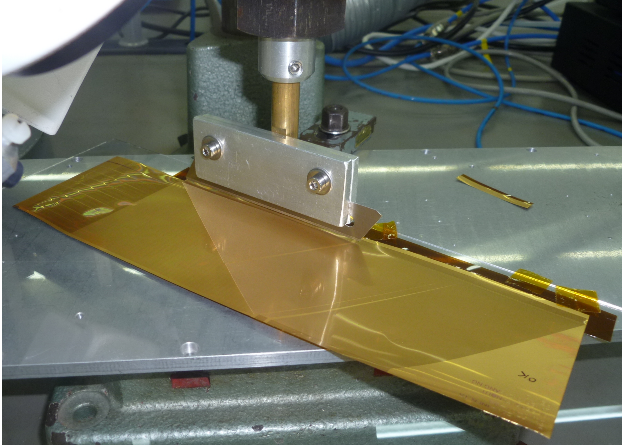

Figure 6.23: Picture of the prototype of the layer 3 z during the cutting procedure.

6.10 Electronics Readout 28 pages

6.10.1 Readout chips V.Re - 10

6.10.1.1 Electronic Readout for Strip and Striplet Detectors

The front-end processing of the signals from the silicon strip detectors will be performed by custom-designed ICs mounted on hybrid circuits that distribute power and signals, and thermally interface the ICs to the cooling system. As discussed below, the very different features of inner (Layer 0-3) and outer layers (4 and 5) of the SVT set divergent requirements to the readout chip, which makes it necessary to include programmable features in the readout ICs, in order to adjust operating parameters over a wide range. This obviously holds also in the case a different technology (pixels) is adopted for Layer 0 instead of short strips (striplets). Generally speaking, the ICs will consist of 128 channels, each connected to a detector strip. The signals from the strips, after amplification and shaping will be compared to a preset threshold. If a signal exceeding the threshold is detected, a 3-4 bit analog information about the signal amplitude will be provided by an ADC: this will mostly serve for calibration and monitoring purposes in the innermost layers, whereas in outer layers it will be essential for dE/dx measurements. The dimensions of the readout IC are expected to be about 6×4 mm^2. As discussed in the SVT HDI subsection of this TDR, the dimensions of the HDI set a 6 mm upper limit on the side of the chip with the bonding pads for the interconnection with the strip sensors. The power dissipation will be below 4 mW/channel including both analog and digital sections. For each channel with a signal above threshold, the strip number, the amplitude information, the chip identification number and the related time stamp will be stored inside the chip waiting for a trigger signal for a time corresponding to the trigger latency (about 7 μs, corresponding to a 150 kHz trigger rate). When a trigger is received, data will be read out and transmitted off chip, otherwise they will be discarded. The data output from the microstrip detector will be sparsified, i.e. will consist only of those channels generating a hit. The readout integrated circuits must remain functional up to 5 times nominal background.

The option of operating in a data push fashion could be preserved for the external layers, where this will be allowed by the low strip hit rate. This will give the possibility to feed data from these layers to the trigger system.

6.10.2 Readout chips requirements

The microstrip electronics must ensure that the detector system operates with adequate efficiency, but also must be robust and easy to test, and must facilitate testing and monitoring of the microstrip sensors. AC coupling is assumed between the strips and the readout electronics.

- **Mechanical Requirements:**
  Number of channels per chip: 128
  Chip size: width ≤6 mm, length ≤4 mm
  Pitch of input bonding pads: <45 μm

- **Operational Requirements:** Operating temperature: <40 °C

Radiation tolerance: >4 Mrad/year, >$6 \cdot 10^{12}$ n_{eq}/cm^2/year (these are the expected values in Layer 0; in outer layers, radiation levels are at least on order of magnitude lower)
Power dissipation: <4 mW/channel
Detector and fanout capacitance: 10 pF $\leq C_D \leq$ 70 pF (the chip must be stable when sensor strips are disconnected from the input pads of the analog channels)

- **Dynamic range:** The front-end chips must accept signals from either P and N-side of the strip detectors. A linear response of the analog processing section is required from a minimum input charge corresponding to 0.2 MIP up to a full dynamic range of 10-15 MIP charge for dE/dx measurements.

- **Analog Resolution:** The front-end chips have to provide an analog information about the charge collected in the detector, which will be also used for calibrating and monitoring the system. A resolution of 0.2 MIP charge is required for dE/dx measurements. In case of a compression-type ADC, based on the time-over-threshold technique (ToT), this may translate in 3-4 bits of information.

- **Efficiency:** At design luminosity, the microstrip readout must have a hit efficiency of at least 95% during its entire operational lifetime. This includes any loss of data by readout electronics or readout dead time.

- **Readout bandwidth:** Data coming out of the chip will be substantially reduced by operating in a triggered mode. The chips can use up to 4 output LVDS lines, as it is needed to handle the higher data throughput in inner SVT layers.

- **Radiation Tolerance:** All the components of the microstrip readout system must remain operational up to 10 years of SuperB running at the nominal luminosity.

- **Peaking Time:** The constraints for the peaking time of the signal at the shaper output are dictated by different needs in inner and outer layers. In Layer 0, the high occupancy due to background and the need to avoid pulse overlap and consequent hit inefficiencies set the required peaking time in the range of t_p=25-50 ns, which also allow for a high timing resolution (see below). In the external layers 4 and 5, where background hit frequency is much smaller and where strips are longer and have a larger capacitance, the peaking time will be mostly determined by the need of reducing series noise contributions and has to be in the range of 0.5-1.0 μs.

- **Signal-to-Noise Ratio:** Concerning the signal, this requirement has to take into account the different thickness of silicon detectors in inner (200 μm) and outer (300 μm) layers, as well the signal spread among various strips that depends on the track angle inside detectors and that, again, may vary in different SVT layers. Noise-related parameters (strip capacitance and distributed resistance) also sizably vary across the SVT. A signal-to noise ratio of 20 has to be ensured across the whole SVT and should not decrease significantly after irradiation. Here are the two extreme cases (where the equivalent noise charge ENC includes the thermal noise contribution from the distributed resistance of the strips):

  - Layer 0 striplets: ENC ≈700 e- at C_D=10 pF and at t_p=25 ns

- Layer 5 strips: ENC ≈1000 e- at C_D=70 pF and at t_p=1 μs

- **Threshold and Dispersion:** Each microstrip channel will be read out by comparing its signal to a settable threshold around 0.2 MIP. Threshold dispersion must be low enough that the noise hit rate and the efficiency are degraded to a negligible extent. Typically, this should be 300 rms electrons at most and should be stable during its entire operational lifetime.

- **Comparator Time Resolution:** The comparator must be fast enough to guarantee that the output can be latched in the right time stamp period.

- **Time Stamp:** 30 ns time stamp resolution is required for inner layers to get a good hit time resolution in order to reduce the occupancy in the offline time window (50-100 ns). In the outer layers the time stamp resolution is less critical since the hit time resolution will be dominated by the long pulse shaping time. A single 30 ns time stamp clock in all layers will be used.

- **Chip clock frequency:** Two main clocks will be used inside the readout chip, the time stamp clock (about 30 MHz) and the readout clock (120 MHz or 180 MHz). These clocks will be synchronized with the 60 MHz SuperB system clock. In case the analog-to-digital conversion is based on the Time-Over-Threshold method, a ToT clock has to be generated inside the chip. The ToT clock period should at least match the pulse shaping time to get a good analog resolution. A faster ToT clock could slightly improve the analog resolution but an upper limit (≈3.5) on the ratio between ToT clock frequency and the shaping time frequency is imposed by the required dynamic range needed for low momentum particle dE/dx measurements (≈10-15 MIP) and the number of bits available for ToT. With the experience of the BaBar Atom chip a ToT clock frequency 3 times higher than the pulse shaping frequency could be used: 120 MHz for L0, 60 MHz for L1-2, 15 MHz for Layer3 and 6-3 MHz for L4-5.

- **Mask, Kill and Inject:** Each micro-strip channel must be testable by charge injection to the front-end amplifier. By digital control, it shall be possible to turn off any micro-strip element from the readout chain.

- **Maximum data rate:** Simulations show that machine-related backgrounds dominate the overall rates. At nominal background levels (including a safety factor of 5), the maximum hit rate per strip goes from about 1 MHz/strip in Layer 0 to about 50 kHz/strip in Layer 5, z-side.

- **Deadtime limits:** The maximum total deadtime of the system must not exceed 10 % at a 150 kHz trigger rate and background 5 times the nominal expected rate.

- **Trigger specifications:** The trigger has a nominal latency of about 7 μs, a maximum jitter of 0.1 μs, and the minimum time between triggers is 70 ns. The maximum Level 1 Trigger rate is 150 kHz.

- **Cross-talk:** Must be less than 2 %.

- **Control of Analog Circuitry on Power-Up:** Upon power-up, the readout chip shall be operational at default settings.

- **Memory of Downloaded Control of Analog Circuitry:** Changes to default settings shall be downloadable via the

readout chip control circuitry, and stored by the readout chip until a new power-up cycle or additional change to default settings.

- **Read-back of Downloadable Information:** All the data that can be downloaded also shall be readable. This includes data that has been modified from the default values and the default values as applied on each chip when not modified.

- **Data Sparsification:** The data output from the microstrip detector shall be only of those channels that are above the settable threshold.

- **Microstrip output data content:** The microstrip hit data must include the time stamp and the microstrip hits (strip number and relevant signal amplitude) for that time stamp. The output data word for each strip hit should contain 16 bits (7 strip address, 4 ToT, 1 type (Hit or Time Stamp) 4 bits to be defined). A 10-bit time stamp information (with 6 additional bits: 1 type, 5 bits to be defined) will be attached to each group of hits associated to a given time stamp (hit readout will be time-ordered).

6.10.3 Readout Chip Implementation

The SuperB SVT readout chips are mixed-signal integrated circuits in a 130 nm CMOS technology and are being designed to comply with the requirements discussed above. Each chip comprises 128 analog channels, each consisting of a charge-sensitive preamplifier, a unipolar semi-Gaussian shaper and a hit discriminator. A polarity selection stage will allow the chip to operate with signals delivered both from n- and p-sides of the SVT double-sided strip detectors. A symmetric baseline restorer may be included to achieve baseline shift suppression. When a hit is detected, a 3-4 bit analog-to-digital conversion will be performed by means of a Time-Over-Threshold (ToT) detection. The hit information will be buffered until a trigger is received; together with the hit time stamp, it will be then transferred to an output interface, where data will be serialized and transmitted off chip on output LVDS lines. An n-bit data output word will be generated for each hit on a strip. A programming interface accepts commands and data from a serial input bus and programmable registers are used to hold input values for DACs that provide currents and voltages required by the analog section. These registers have other functions, such as controlling data output speed and selecting the pattern for charge injection tests.

Given the very different requirements of inner and outer layers, in terms both of detector parameters and hit frequency, several programmable features will be included in the chips such as the peaking time, the gain and the size of the input device. The block diagram of the analog channel is shown in Fig. 6.24.

The digital readout of the matrix will exploit the architecture that was originally devised for a high-rate, high-efficiency readout of a large CMOS pixel sensor matrix. Each strip has a dedicated array of pre-trigger buffers, which can be filled by hits with different time stamps. The size of this buffer array is determined by the maximum strip hit rate (inner layers) and by the trigger latency. After arrival of a trigger, only hits with the same time stamp as the one provided by the triggering system send their information to the back-end. The array of 128 strips is divided in four sections, each with a dedicated sparsifier encoding the hits in a single clock cycle. The storage element next to each sparsifier (barrel level-2) acts like a FIFO memory conveying data to a barrel-L1 by a concentrator which merges the flux of data and preserves the time order of the hits. This barrel-L1 will drive the output data bus which will use up to four output lines depending on the data throughput and will be synchronous to a 120 MHz clock.

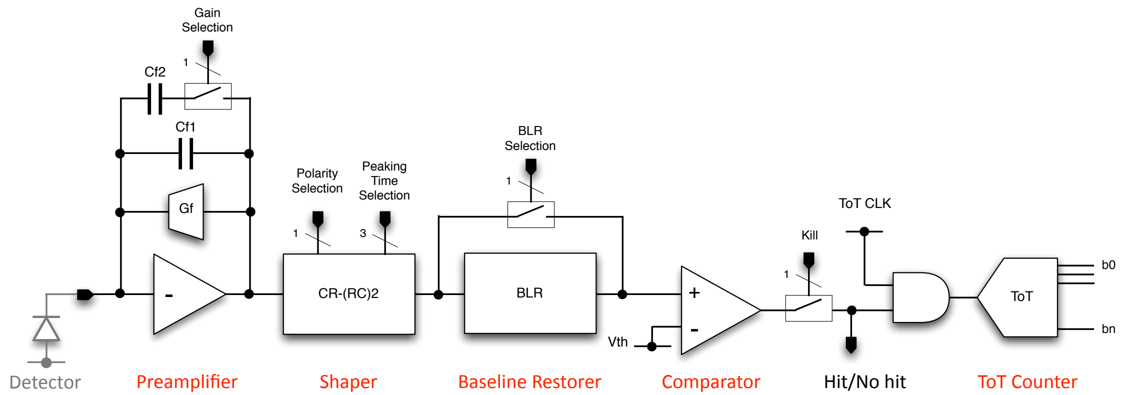

Figure 6.24: Analog channel block diagram.

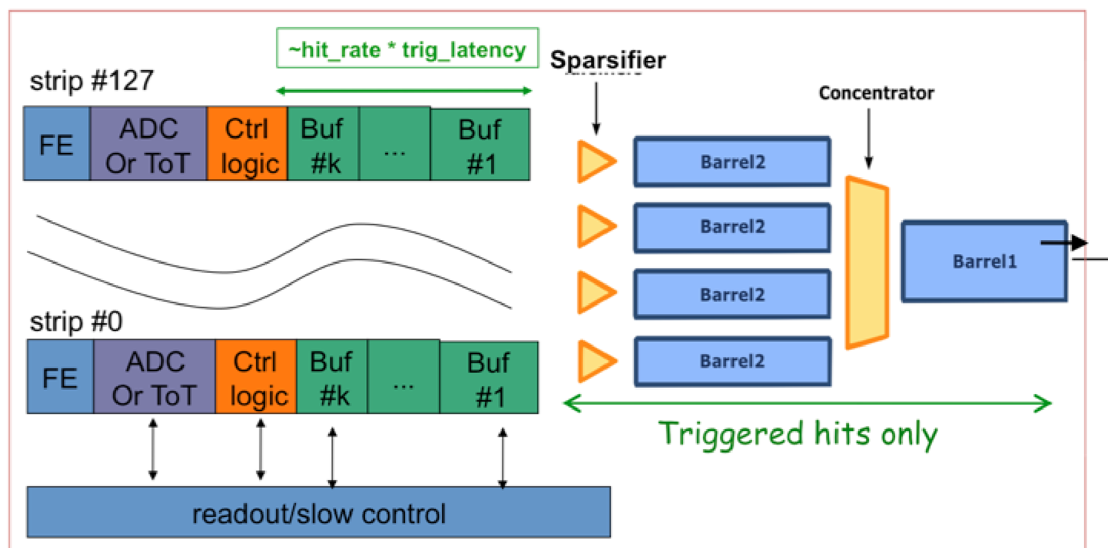

Figure 6.25: Readout architecture of the SVT strip readout chips.

6.10.4 R&D for strip readout chips

The R&D to support the development of the SuperB strip readout chips has begun in 2011. The chosen technology for integration is a 130 nm CMOS process: this has an intrinsically high degree of radiation resistance, which can be enhanced with some proper layout prescriptions such as enclosed NMOS transistors and guard rings. There is a large degree of experience with mixed-signal design in this CMOS node that was gained in the last few years inside the HEP community.

The readout architecture is being tested with realistic data created by Monte Carlo analysis of the interaction region. Verilog simulations demonstrate that the chip will be able to operate with a 99 % readout efficiency in the worst case condition, which includes the safety factor of 5 in the background levels.

The analog section of the chip is being optimized from the standpoint of noise, comparator threshold dispersion and sensitivity to variations of process parameters. It will be possible to select the peaking time of the signal at the shaper output (25-200 ns for inner layers, 350-750 μs for outer layers) by changing the value of capacitors in the shaper. In this way the noise performances of the chip can be optimized according to the signal occupancy, preserving the required efficiency. Table 6.13 shows the main parameters of the analog section, according to simulation estimates for realistic values of detector parameters and strip hit rates. The loss in efficiency is determined by the limits in the double pulse resolution of the analog section, which depends on the signal peaking time. An acceptable compromise will be found here with the noise performance.

In 2012, the submission of a chip prototype including 64 analog channels and a reduced-scale version of the readout architecture is foreseen.

The submission of the full-scale, 128-channels chip prototypes is then scheduled in late 2013. This version will have the full functionality of the final production chip.

6.10.5 Hybrid Design M.Citterio - 10

6.10.6 Data Transmission M.Citterio - 10

6.10.7 Power Supply - 2

6.11 Mechanical Support and Assembly S.Bettarini/F.Bosi - 14 pages

---

An overview of the mechanical support and assembly is provided in section 6.1. In this section we provide a more detailed account of the constraints of the mechanical design due to the accelerator components near the IP and describe the details of the detector assembly, installation, survey, and monitoring.

6.11.1 I.R. Constraint

The support structure design and configuration of the SVT is dictated by the configuration and assembly procedure of the machine components near the interaction point, as well as by the SVT geometry. The background condition dictates the need for a pair of Tungsten conical shield located about 25 cm from the IP on either side. There are two further Tungsten shields of cylindrical shape that are located symmetrically with respect to the I.P., starting just at the end of the conical ones and that are fixed at the calorimeter structure.
These conical shields and the final focus permanent magnets occupy most of the region below 17.2 (300 mrad) on both side of the I.P. . In order to minimize the mass inside the active tracking volume , it is desirable to mount all of the electronics below the 300 mrad cone. This requires that in backward and forward directions electronics, cooling, cabling and supports must be confined in a volume of about one centimeter thick around the conical shields. The use of this small space below the 300 mrad must be carefully arranged with the needs of the accelerator. The solid angle coverage of the SVT is therefore restricted to a region $17.2° < \theta < 162.8°$. The radial position the SVT fiducial volume is imposed by the inner radius of DCH at about 25 cm.

Table 6.13: Main parameters of the analog section of the SVT strip readout chips.

Layer	C_D [pF] including fanout (with ganging)	t_p [ns] Available	t_p [ns] Selected	Total ENC [e rms]	Total ENC [e rms] after 7.5 years	Total ENC [e rms] after 7.5 years with ×5 safety factor	Hit rate/strip [kHz] nominal	Efficiency 1-N nominal	Efficiency 1-N with ×5 safety factor
0-side u	11.2		25	936	952	1016	187	0.99	095
0-side v	4.0		25	939	956	1019	187	0.99	0.97
1 phi	33.4		75	1122	1197	1457	170	0.98	0.92
1 z	27.6	25-200	75	748	899	1342	134	0.98	0.91
2 phi	37.2		100	1085	1174	1476	134	0.98	0.90
2 z	30.3		100	711	876	1346	134	0.98	0.88
3 phi	35.7		150	897	1125	1763	116	0.96	0.82
3 z	40.8		150	707	935	1540	79	0.98	0.90
4 phi	52.5		500	1075	1265	1805	25	0.98	0.92
4 z	47.2	375, 500	500	895	1115	1715	13.4	0.99	0.95
5 phi	65.5	750	750	1085	1205	1530	16.2	0.98	0.93
5 z	52.2		750	855	965	1280	8.8	0.99	0.95

The Berillium beam-pipe, about 2 cm in diameter and 40 cm long, is positioned symmetrically respect to the I.P. and it supports directly the L0 detector. The eight striplet modules, arranged in a pin wheel geometry, are mounted on the two cooled flanges. The L0 is mechanically decoupled by the other layers of the SVT. They are supported on the backward and forward side on the W conical shields by two gimbal rings, allowing the necessary degree of freedom preventing SVT over-constraints during the mounting operations. The Be beam-pipe is connected at each side through a bellow and a CF flange to the cryostat beam-pipe, splitted in the two arms. The LER and HER pipelines represent the warm internal vessel of the cryostat in the superconducting final focus magnet system. The forward and backward cryostats are symmetrically positioned around the I.P. and as extreme components of the I.R. , with the cryostat beam-pipe terminal CF flanges placed at about 2.2 m far from I.P. The cryostat is rigidly connected to the W conical shield flanges and through the terminal back flange, at a very rigid coaxial external tube, allowing a free space of about 2 cm in radius along its extension, for the SVT-L0 cables way-out. A longitudinal section of the I.R. system showing all the components is reported in Fig. 6.11.1.

Since the SVT and the L0 must be installed with all the components of I.R. system in place, they must be splitted in two halves and them clam-shelled around the beam-pipe. The assembly and alignment of the whole I.R. system, consisting of the Be beam-pipe, the SVT detectors, the forward and backward final focus permanent magnets, the W conical shields and cryostats, will take place in a staging area away from interaction hall. The entire assembly will then transported and installed in the experimental hall during the detector-commissioning phase . From the mechanical point of view, the I.R. system is comparable at two very rigid systems (W conical shield + cryostat + external tube) joint by a very weak system (the Be beam-pipe, L0 and SVT) that could be damaged during the transportation and mounting in the experiment location. On the other hand no stiffening struc-

ture (i.e. a support tube) can be mounted on the L0 and the SVT detectors to connect this two rigid systems. Any further passive material between SVT and DCH in the active region must be avoided. Moreover, there is a strong requirement for a rapid replacement of the L0 detector in the experiment, avoiding a long period of inactivity. Therefore it is necessary to foresee the design of a removable structural support, in the following called temporary cage. It must connect rigidly the backward and forward conical shields and absorb the mechanical stress present at the moment of the first transportation to the experimental hall and during the accesses to demount of the L0. This structure has to be removable at the beginning of the running phase and remounted in the occasion of the shut-down. The operation that allows the access to L0-SVT detector is called quick demounting.

6.11.2 Module Assembly

The SVT is built with detector modules, each mechanically and electrically independent. Each module consists of silicon wafers glued to fiber composite ribs, with an high density interconnect (HDI) electronic hybrid at each end. The HDIs are electrically connected to the silicon strips by means of flexible circuits and are mechanically supported by the fiber composite beam. The entire module assembly is a rigid structure that can be tested and transported in its case. A drawing of a detector module from layer 3 is shown in Fig. 6.11.2.

The assembly of a detector module begins with the preparation of the necessary parts. The silicon detectors must be fully tested, including a long-term (burn-in) test under full bias voltage. The fanout circuits will be optically inspected and single trace tested for spotting short or opens. The readout hybrid must be assembled and tested, starting with the HDI circuit, the front-end chips, additional passive components, and the hybrid support. Finally, the completed rib, which provide mechanical stiffness, must be inspected to ensure they meet specifications. These individual parts will be fabricated by different SVT Institutions from which they can be shipped to the institutions where the module assembly is carried out. The hybrids will be tested again after shipment.

The assembly of the inner barrel-shaped modules and the outer arch-shaped modules is necessarily different. However, there are common steps. Generally the procedure is as follows:

1. each silicon detector is precisely aligned respect to the reference cross and head to head glued to the adjacent to form the module;

2. the z and ϕ fanouts are glued to the detectors and wire-bonded to the strips. The ganging bonds between ϕ strips are then performed;

3. the silicon detectors and the readout hybrid are held on a suitable fixture and aligned. The fanouts are glued to the hybrids and wire bonded to the input channels of the readout ICs. Electrical tests, including an infrared laser strip scan, are performed to assess the quality of the detector-fanout assembly (DFAs). An optical survey is foreseen;

4. the final assembly stage is different for different layers. The module of the layers 1 and 2 are then joined together by gluing the beams on the top of layer 1 to the bottom of layer 2 to give a combined structure called the "sextant". For the layer 3, the DFA is bonded flat to the fiber composite beams. For the modules of layer 4 and 5 , the DFA is held in a suitable fixture and bent on a very precise mask at the corners of the arch and at the connection to the HDI. The fiber composite beams are glued to the module with fixtures assuring alignment between the silicon detectors and the mounting surfaces on the HDI. This procedure has been already successfully adopted for the external modules of the SVT of the BaBar experiment;

5. once completed, these detector modules are extremely rigid ladders that can be stored and submitted to the final electrical characterization. They are then shipped to the

location for the final installation on the detector.

The assembly procedures for the L0 module detector follow in general which we reported for the other SVT layers, although the smaller sensor dimensions and two fanout layers represent a greater difficulty in the handling. Other differences can be outlined. No detector alignment is requested because there is only one detector; the final assembly stage for layer 0 module is more simple respect to the Layer 4 and 5 because there are not bent detectors. But the shape of the L0 module needs a very precise mask able to put the HDI in a in very precise position on to a plane inclined of 10° respect to the detector. The DFA is held in a suitable fixture and bent on a mask at the connection to the HDI. The module is then tested. The fiber composite beams are glued to the module with fixtures assuring alignment between the silicon detectors and the mounting surfaces on the HDI. A drawing of a detector module of the layer 0 is shown in Fig. 6.11.2.

6.11.3 Detector Assembly and Installation

6.11.3.1 SVT Half Detector Assembly

The L1-L5 detector is assembled in halves in order to allow the device to be clam-shelled around the beam pipe. The detector module are supported at each end by cooling/support rings in brass material that are fixed on the support cones realized in laminated carbon-fiber. Cooling water circulates at the internal of the cooling rings and to cool the mounting protrude pieces (buttons) supporting the HDI and in thermal contact with them. The cones are divided along a vertical plane and have alignment pins and latches that allow them to be connected together around the W conical shielding. The two carbon fiber support cones are mechanically connected by a low mass carbon fiber space frame. For a drawing of the cooling cones see Fig. 6.11.3.1.

During the half detector-assembly, the two half-cones will be held in a fixture which holds them in precise relative alignment. The detector modules are then mounted to the half-cones to each end. A fixture holds the detectors module during this operation and allow for well-controlled positioning of the module relative to the half-cones. Pins located in the buttons provide precise positioning of the modules, which are then fixed with screws. Accurate alignment with respect to the silicon wafers is achieved by a pair of mating fixtures . One is a dummy module (Mistress mask) and the other simulate the mating surface of the cone (Master Mask). These fixtures are constructed together and mate perfectly. One is used to verify the right machining of the mounting of the cooling ring on the cones. The other is used to position the mounting point on the HDI during the assembly of the module as mentioned in the module assembly description.
The connection between the module and the cone (called foot) provides for accurate and reproducible alignment of the module and conduction of heat from the HDI heath sink to the water cooled ring.
A detail of the foot region, which contains the readout electronics and the cooling ring with the mounting button pieces is shown in Fig. 6.11.3.1.

After verification of the alignment, the connection between the HDI and the support beam is permanently glued. The glue joint allow for the correction of small errors in the construction of either the cones or the module. After the the beam is glued, the module may be removed and remounted on the cone as necessary. The design of the foot allow this glue joint to be cleaved and remade should major repair of the module be required. After each detector module mounted, it is electrically tested using a laser scan to verify its functionality. As each layer is completed, it is optically surveyed and the data are entered in a database. Finally, the two half cones are connected together with the space frame, resulting in a completed half-detector assembly.

6.11.3.2 Mount L0 on the Be-pipe and L 1-5 on the W Shielding

When the two L1-L5 half-detector assemblies are completed, they are brought to the staging area where both W conical shield and the Final Focus superconductor Magnet Cryostat and L0 have been assembled on the Be beam-pipe . Fixtures are employed to hold the cones as they are brought together and clam-shelled around the L0 and Be beam-pipe. The two half detector assemblies are mated and the latches between them are closed. The cable from HDIs are connected to the transition card, which are mounted in cooling support flanges at the end of W conical shield. The entire detector is then thoroughly tested and an optical survey is performed. After the survey is completed the Temporary Cage Sectors are mounted on the W Conical Shield flanges and rigidly fixed on to the W Conical Shield flanges . At this point the assembly is relatively rigid and can be transported to the interaction hall and installed.

The detector assembly as described above forms a rigid structure as long as the cones and space frame are connected together. This structure is supported on the W conical shields . During transport of the I.R. Assembly to the interaction hall, it is possible to have for the forward side of I.R. Assembly as much as 1mm relative motion respect to the backward side. This motion is reversible, and they will return to their original alignment when installed in normal condition in the accelerator. In addition, differential thermal expansion may affect the relative alignment of the magnets during periods in which the temperature is not controlled, and relative motion of the magnet and the beam-pipe may occur in case of seismic activity.

The support of the detector from the W conical shield must allow for this motion without placing stress on the silicon wafers. In addition, the position relative to the I.R. must be reproducible when installed in the accelerator. These constrains are met by mounting the support cones on a pairs of Gimbal Rings. One gimbal ring connects the forward cone to the W Conical Shield so as to constrain its center in x, y, and z, while allowing rotation about the x and y axes. A second set of Gimbal Ring supports the cone in the backward direction in a similar manner, with an additional sleeve that allows both for motion along z and rotation about the z axis, relative to the W Conical Shields .

6.11.3.3 Installation of Complete Assembly into the SuperB Detector

The clearance between the SVT, the L0 and beam tube are on the order of 1 to 2 mm. During the transportation of the I.R. Assembly, the critical clearances must be monitored in real time to ensure that no accidental damage to the detectors occours. In its final position, the I.R.Assembly will be supported along the External Tube on to the W cylinder Shield. Thus it is necessary that is always supported only on this region during installation. One possible installation scenario employs a crane that handle a long stiff beam that support rigidly the entire I.R. Assembly trough the forward and backward external tube and it is able to lay carefully this system on to that is aligned respect to the W Cylinder Shield and positioned in front of the FCAL region. In a similar way to the Quick Demounting operation procedure, it will be possible to move the I.R. Assembly through the DCH using the translation system existing on the W Cylinder Shield which has been previously aligned with respect to the SuperB detector. Once the I.R. assembly is in the final position the External Mechanical Cradle is removed.

6.11.3.4 Quick Demounting

The quick demounting is the operation required in case the L0 has been damaged and it has to be repaired or replaced with a new detector in a short amount of time. It allows to slide the SVT detector out of the SuperB experiment, leave that just close to the forward door to perform the work and then slide that back inside the whole detector staying always in the experimental hall. It is crucial that the time needed to perform this operation has to be much shorter with respect to the Babar experiment . Due to the impossibility to operate on the SVT de-

tector at the internal of the experiment, in a forward end plug open conditions, the quick demounting operation plans to move rigidly all the I.R. assembly components along Z axis in the forward direction up to a position that allows the SVT detector to be completely out to of the FCAL wall, at Z=+2650 , where it is possible to operate on the L0 detector around the Be beam-pipe. In this hypothesis it is assumed that W cylindrical backward and forward shields are rigidly fixed onto the calorimeter structure and perfectly aligned along the Z axis direction, having a supporting function in the I.R. translation. The stroke necessary for the SVT demounting position is about 3200 mm. The total weight of the I.R. assembly components is of about 1.65 Tons. A longitudinal section of the I.R. system assembly showing the initial and final positions in the quick demounting operation is reported in Fig. 6.11.3.4. A beam profile infrastructure of about 3x4x3 m^3 volume will be mounted on the FCAL wall and it will be equipped with the appropriate filters and fans to maintain ISO 8 cleanness conditions for a four-person team working to the SVT L0 demounting. From a mechanical point of view the SuperB I.R. is configured such that there are two very rigid systems positioned in both sides respect to the I.P. Each system consists of the Final Focus Superconductive Magnet Cryostat (FFSCM), the Conical shield and the External Tube, joined trough the gimbal ring. The SVT system represents the weak ring of the this mechanical chain. The Be-beam pipe is joined to the Cryostat beam-pipe trough a system of flexible bellow flanges. In a different way from Babar experiment, where the SVT region was stiffened by the C.F. support tube, in the SuperB experiment for physics reasons it is not possible to insert any stiffening structure to overlay with passive material the DCH. Therefore it is necessary to design a temporary and removable structural support. Thus, this temporary cage fixes rigidly the forward and backward W conical shields around the SVT region; it is able to absorb all the mechanical stress that could be present during the quick demounting operations; it can be removable by operating from the FCAL region, once the SVT is in running position, leaving free the space between SVT and DCH.

When the temporary cage is mounted and rigidly connects the two opposite conical shields, we can consider the whole I.R. assembly (forward side + backward sides + SVT) as a rigid body supported by several recirculating spheres embedded in the W cylinder shields, acting on the three rails positioned at 120 ° that are formed on the external tube profile. This translation system is able to guide the entire I.R. assembly and prevent any rotation during the quick demounting movement . The cylinder shields include also a mechanical system (the Radial Blocking Device) able to rigidly block the I.R. assembly at the correct position with respect to the I.P. This blocking is acted by longitudinal bars that push on a mechanical conical device embedded in the W cylinder shield, able to block radially the external tube respect to the W cylinder shield. This blocking system is also useful at the moment of the temporary cage mounting/demounting on the W conical shield flange operations, in order not to transfer any mechanical stress on the SVT detector and the Be beam-pipe.

Due to the translation rails on the external tube the temporary cage is cylindrically shaped in three independent separate sector, confined in a radial space between the external tube and W cylinder shield. The temporary cage sectors are made in a metal sandwich structure with very high flexional resistance. Each temporary cage sector is moved towards the I.P. position supported by two removable beam-rails expressly mounted and embedded in the W cylinder shield for the quick demounting operations. The beam-rails has a length such to arrive and to be fixed on to the opposite W cylinder shields in order to support the temporary cage sector when is located over the SVT region. The temporary cage sector has a special mechanical connection on the front side in order to perform a coupling in a secure conical way on the backward W conical shield flange. Instead on to the backward side it has special radial bushing device able to be fixed to the forward W coni-

cal flange avoiding any mechanical stress to the SVT detector. The temporary cage sector fixing screws are tighten with a long special screw driver by acting at the working area in front of FCAL (forward side) and the Horse Shoes region (backward side) . Once mounted to the Beam Profile Infrastructure and aligned to the beam line it is also needed a Mechanical Support Cradle Facility having the function of rails prolongation and support for the I.R. Assembly when it is in a position out of FCAL . An artistic view of the I.R. System Assembly showing some components of the Quick Demounting operation is represented in Fig. 6.11.3.4. To enable the Quick Demounting operation, the SVT cables are disconnected at the level of the patch-panel. Also for the for the cryogenic service to the Cryostat Final Focus Superconductor Magnet it has to be foreseen an extra-length and flexible pipe connection. Monitoring position devices are planned to be installed on the W Cilinder backward and forward Shields in order to control all the positions of the components during the mounting-demounting operations. Also a strain-gage set is planned to be mounted on the Temporary Cage Sectors to monitor the mechanical stress on the sectors in the different positions of the in /out translation.

6.11.4 Detector Placement and Survey

6.11.4.1 Placement accuracy

6.11.4.2 Survey with tracks

6.11.5 Detector Monitoring

6.11.5.1 Position Monitoring System

6.11.5.2 Radiation Monitoring

6.11.6 R&D Program

6.11.6.1 Cables

6.11.6.2 hybrid

6.11.6.3 Inner layer sextant

6.11.6.4 Arch modules

6.11.6.5 Cones and space frame

6.11.6.6 Full-scale model of IR

6.12 Layer0 Upgrade Options G.Rizzo/L.Ratti - 10 pages

With the machine operated at full luminosity, the layer 0 of the silicon vertex tracker may benefit from upgrading to a pixellated detector. This solution can actually provide some significant advantages with respect to the baseline striplet option. In particular

- the occupancy per detector element from machine background is expected to fall to a few kHz, with a major impact on the speed specifications for the front-end electronics, mainly set by the background hit rate in the case of the striplet readout chip;
- better accuracy in vertex reconstruction can be achieved with a detector pitch of 50 μm or smaller; the shape of the pixel can be optimized in such a way to reduce the sensor pitch in the z direction while keeping the area in the range of 2500-3000 μm^2, which guarantees enough room for sparse readout functionalities.

A few technology alternatives for pixel detector fabrication are being investigated and R&D activities are in progress to understand advantages and potential issues of the different options.

6.12.1 Technology options

Following is a description of the technology options that are being considered for the upgrade of the SuperB SVT innermost layer.

6.12.1.1 Hybrid pixels

Hybrid pixel technology has reached quite a mature stage of development. Hybrid pixel detectors are currently used in the LHC experiments [40, 41, 42, 43], with pitch in the range from 100 μm to a few hundred μm, and miniaturization is being further pushed forward in view of the upgrade of the same experiments at the High Luminosity LHC (HL-LHC) [62, 45, 46]. Hybrid pixel systems are based on the interconnection between a sensor matrix fabricated in a high resistivity substrate

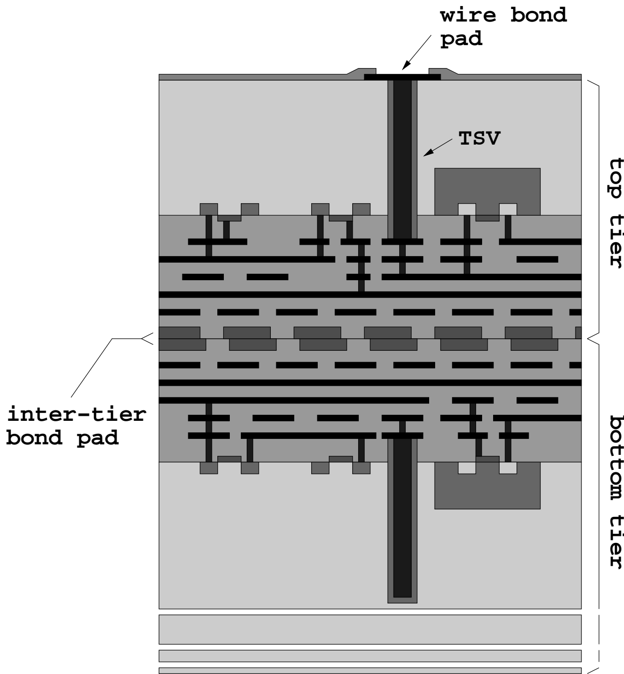

Figure 6.26: cross-sectional view of a double-layer 3D process.

and a readout chip. Bump-bonding with indium or indium-tin or tin-lead alloys is the mainstream technology for readout chip-to-sensor interconnection. The design of a hybrid pixel detector for the SVT innermost layer has to meet some challenging specifications in terms of material budget and spatial resolution. Since the readout chip and the sensor are laid one upon the other, hybrid pixels are intrinsically thicker detectors than microstrips. Interconnect material may further degrade the performance, significantly increasing the radiation length equivalent thickness of the detector. As far as the readout and sensor chips are concerned, substrate thinning to 100-150 μm and subsequent interconnection are within present technology reach. Further thinning may pose some issues in terms of mechanical stability and, as the detector thickness is reduced, of signal-to-noise ratio and/or front-end chip power dissipation. Concerning interconnection, the vertical integration processes currently under investigation in the high energy physics community might help reduce the amount of material. Among the commercially available technologies, the ones provided by the Japanese T-Micro (formerly known as ZyCube), based on so called micro-bumps, and by the US based company Ziptronix, denoted as direct bonding technique, seem the most promising [47]. The Fraunhofer EMFT has developed a bonding technique called SLID and based on a very thin eutectic Cu-Sn alloy to interconnect the chips [48]. The spatial resolution constraints set a limit to the area of the elementary readout cell and, as a consequence, to the amount of functionalities that can be included in the front-end electronics. A planar, 130 nm CMOS technology may guarantee the required density for data sparsification and in-pixel time stamping in a 50 μm×50 μm pixel area (as already observed, a different aspect ratio might be preferred to improve the resolution performance in one particular direction). The above mentioned interconnection techniques can fully comply with the detector pitch requirements (in the case of the T-Micro technology, pitches as small as 8 μm can be achieved). A fine pitch (30 μm minimum), more standard bump-bonding technology is also provided by IZM. This technology has actually been successfully used to bond the SuperPIX0 front-end chip (to be described later on in this section) to a 200 μm thick pixel detector.
Denser CMOS technologies (belonging to the 90 or 65 nm technology) can be used to increase the functional density in the readout electronics and include such functions as gain calibration, local threshold adjustment and amplitude measurement and storage. In this case, costs for R&D (and, eventually, production) would increase significantly. Vertical integration (or 3D) CMOS technologies may represent a lower cost alternative to sub-100 nm CMOS processes. The technology cross section shown in Fig. 6.26, in particular, points to the main features of the extremely cost-effective process provided by Tezzaron Semiconductor [49] which was used for the design of the SDR1 chip. The Tezzaron process can be used to vertically integrate two (or more) layers, specifically fabricated and processed for this purpose by Chartered Semicon-

ductor (now Globalfoundry) in a 130 nm CMOS technology. In the Tezzaron/Chartered process, wafers are face-to-face bonded by means of thermo-compression techniques. Bond pads on each wafer are laid out on the copper top metal layer and provide the electrical contacts between devices integrated in the two layers. The top tier is thinned down to about 12 μm to expose the through silicon vias (TSV), therefore making connection to the buried circuits possible. Among the options available in the Chartered technology, the low power (1.5 V supply voltage) transistor option is considered the most suitable for detector front-end applications. The technology also provides 6 metal layers (including two top, thick metals), dual gate option (3.3 V I/O transistors) and N- and P-channel devices with multiple threshold voltages. The main advantages deriving from a vertical integration approach to the design of a hybrid pixel front-end chip can be summarized as follows:

- since the effective area is twice the area of a planar technology from the same CMOS node, a better trade-off can be found between the amount of integrated functionalities and the detector pitch;
- separating the digital from the analog section of the front-end electronics can effectively prevent digital blocks from interfering with the analog section and from capacitively coupling to the sensor through the bump bond pad.

The design of a 3D front-end chip for pixel detectors is in progress in the framework of the VIPIX experiment funded by INFN.

6.12.1.2 Deep N-well CMOS monolithic sensors

Deep N-well (DNW) CMOS monolithic active pixel sensors (MAPS) are based on an original design approach proposed a few years ago and developed in the framework of the SLIM5 INFN experiment [35]. The DNW MAPS approach takes advantage of the properties of triple well structures to lay out a sensor with relatively large area (as compared to standard three transistor MAPS [50]) read out by a classical processing chain for capacitive detectors. As shown by the technology cross section in Fig. 6.27, the sensor, featuring a buried N-type layer with N-wells (NW) on its contour according to a typical deep N-well scheme, collects the charge released by the impinging particle and diffusing through the substrate, whose active volume is limited to the uppermost 20-30 μm thick layer below the collecting electrode. Therefore, within this extent, substrate thinning is not expected to significantly affect charge collection efficiency, while improving momentum resolution performance in charged particle tracking applications. As mentioned above, DNW MAPS have been proposed chiefly to comply with the intense data rates foreseen for tracking applications at the future high energy physics (HEP) facilities. The area taken by the deep N-well collecting electrode can actually be exploited to integrate the NMOS parts of the analog front-end inside the internal P-well. A small amount of standard N-well area can be used for PMOS devices, instrumental to the design of high performance analog and digital blocks taking full advantage of CMOS technology properties. In this way, both analog functions, such as signal shaping, and digital functions, such as time stamping and data storing, buffering and sparsification, can be included in the pixel operation. Note that the presence of N-wells other than the sensor is instead strongly discouraged in standard MAPS design, where the operation of the tiny collecting electrode would be jeopardized by the presence of any N-type diffusion in the surrounding. Based on the concept of the DNW monolithic sensor, the MAPS detectors of the Apsel series (see Section 6.12.2.2), which are among the first monolithic sensors with pixel-level data sparsification [51, 52], have been developed in a planar, 130 nm CMOS technology. In 2008, the Apsel4D, a DNW MAPS with 128×32 elements has been successfully tested at the Proton Synchrotron facility at CERN [55]. More recently, vertical integration technologies, like the ones discussed in the previous section for hybrid pixels, have been considered for the design of 3D

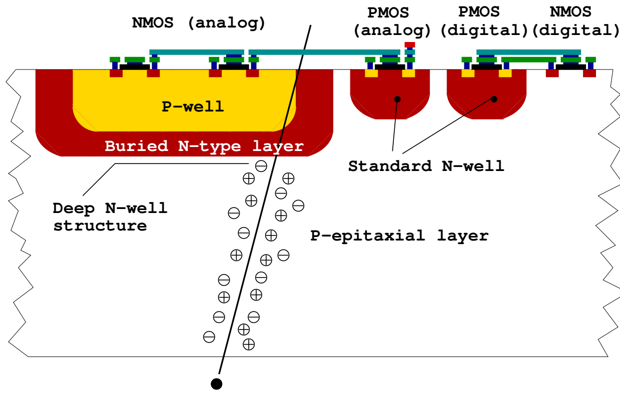

Figure 6.27: simplified cross-sectional view of a DNW MAPS. NMOS devices belonging to the analog section may be built inside the sensor, while the other transistors cover the remaining area of the elementary cell, with PMOSFETs integrated inside standard N-wells.

DNW monolithic sensors. Some specific advantages can derive from the vertical integration approach to DNW MAPS. In particular, all the PMOS devices used in digital blocks can be integrated in a different substrate from the sensor, therefore significantly reducing the amount of N-well area (with its parasitic charge collection effects) in the surroundings of the collecting electrode and improving the detector charge collection efficiency (CCE). The first prototypes of 3D DNW MAPS [57, 58] have been submitted in the framework of the 3D-IC collaboration [59]. Characterization has started in the last quarter of 2011.

6.12.1.3 Monolithic pixels in CMOS quadruple well technology

In DNW MAPS, charge collection efficiency can be negatively affected, although to a limited extent, by the presence of competitive N-wells including the PMOS transistors of the pixel readout chain, which may subtract charge from the collecting electrode. Inefficiency is related to the relative weight of N-well area with respect to the DNW collecting electrode area. A novel approach for isolating PMOS N-wells has been made available with a planar 180 nm CMOS process called INMAPS, featuring a quadruple well structure [52]. Fig. 6.28 shows a simplified cross section of a pixel fabricated with the INMAPS process. By means of an additional processing step, a high energy deep P-well implant is deposited beneath the PMOS N-well (and not under the N-well diode acting as collecting electrode). This implant creates a barrier to charge diffusing in the epitaxial layer, preventing it from being collected by the positively biased N-wells of in-pixel circuits and enabling a theoretical charge collection efficiency of 100%. The NMOS transistors are designed in heavily doped P-wells located in a P-doped epitaxial layer which has been grown upon the low resistivity substrate. Epitaxial layers with different thickness (5, 12 or 18 μm) and resistivity (standard, about 50 Ω·cm, and high resistivity, 1 kΩ·cm) are available. The epitaxial layer is obviously expected to play an important role in improving charge collection performance. Actually, carriers released in the epitaxial layer are kept there by the potential barriers at the P-well/epi-layer and epi-layer/substrate junctions. A test chip, including several different test structures to characterize both the readout electronics and the collecting electrode performance has been submitted in the third quarter of 2011. Results from the preliminary

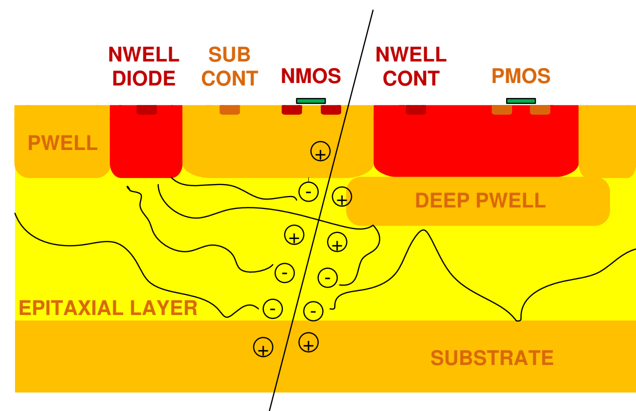

Figure 6.28: cross-sectional view of the INMAPS CMOS technology; emphasis is put on the deep P-well layer.

characterization of the prototypes are discussed in Section 6.12.2.3.

6.12.2 Overview of the R&D activity

6.12.2.1 Front-end electronics for hybrid pixels in planar and 3D CMOS technology

A prototype hybrid pixel detector named SuperPIX0 has been designed as a first iteration step aimed at the development of a device to be used for the layer0 upgrade. The main novelties of this approach are the sensor pitch size ($50\times50\mu$m) and thickness (200μm) as well as the custom front-end chip architecture providing a sparsified and data-driven readout. The SuperPIX0 pixel sensor is made of n-type, Float Zone, high-resistivity silicon wafers, with a nominal resistivity larger than 10 kΩ. The SuperPIX0 chip, fabricated in the STMicroelectronics 130nm CMOS technology, is composed of 4096 channels (50x50 μm^2) arranged into 128 columns by 32 rows. Each cell contains an analog charge processor (shown in Fig. 6.29) where the sensor charge signal is amplified and compared to a chip-wide preset threshold by a discriminator. The in-pixel digital logic, which follows the comparator, stores the hit in an edge-triggered set reset flip-flop and notifies the periphery of the hit. The charge sensitive amplifier uses a single-ended folded cascode topology, which is a common choice for low-voltage, high gain amplifiers. The 20 fF MOS feedback capacitor is discharged by a constant current which can be externally adjusted, giving an output pulse shape that is dependent upon the input charge. The peaking time increases with the collected charge and is in the order of 100 ns for 16000 electrons injected. The charge collected in the detector pixel reaches the preamplifier input via the bump bond connection. Alternatively, a calibration charge can be injected at the preamplifier input through a 10 fF internal injection capacitance so that threshold, noise and crosstalk measurements can be performed. The calibration voltage step is provided externally by a dedicated line. Channel selection is performed by means of a control section implemented in each pixel. This control block, which is a cell of a shift register, enables the injection of the charge though the calibration capacitance. Each pixel features a digital mask used to isolate single noisy channel. This mask is implemented in the readout logic. The input device (whose dimensions were chosen based on [53]) featuring an aspect ratio W/L=18/0.3 and a drain current of about 0.5 μA, is biased in the weak inversion region. A non-minimum length has been chosen to avoid short channel effects. The PMOS current source in the input branch has been sized to have a smaller transconductance than the input transistor. The analog front-end cell uses two power supplies. The analog supply (AVDD) is referenced to AGND, while the digital supply is referenced to DGND. Both supplies have a nominal operating value of 1.2 V. Since single-ended amplifiers are sensitive to voltage fluctuations on the supply lines, the charge preamplifier is connected to the AVDD. The threshold discriminator and voltage references are connected to the AVDD and AGND as well. The in-pixel digital logic is connected to the digital supply. The substrate of the transistors is connected to a separate net and merged to the analog ground at the border of the matrix. The SuperPIX0 chip has been fabricated in a six metal level technology. Special attention has been paid to layout the channel with a proper shielding scheme. Two levels of metal have been used to route the analog signals, two for the digital ones and two for distributing the analog and digital supplies. The supply lines, at the same time, shield the analog signals from the digital activity.

For nominal bias conditions the power consumption is about 1.5 μW per channel. More details on the design of the analog front-end can be found in the literature [54]. The measured threshold dispersion in the chip is around 490 e- with an average pixel noise of about 60 e- (without the sensor connected). Since the threshold dispersion is a crucial characteristic to be considered in order to meet the required specifications in terms of noise occupancy and efficiency, circuits for threshold fine-adjusting have to be implemented in the next version of the chip.

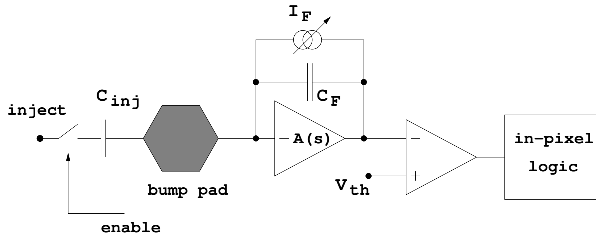

Figure 6.29: block diagram of the analog front-end electronics for the elementary cell of the SuperPIX0 readout chip.

These results have been extracted using the gain measured with an internal calibration circuit, implemented in the pixel, injecting a charge from 0 to 12 fC in each channel preamplifier. An average gain of about 40 mV/fC with a dispersion at the level of 5% has been obtained. The front-end chip has been connected by bump-bonding to a high resistivity pixel sensor matrix of 200 μm thickness. The bump-bonding process has been performed by the Fraunhofer

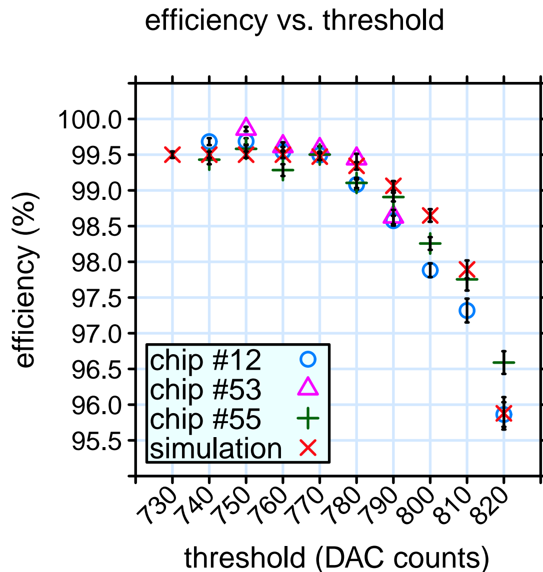

Figure 6.30: Superpix0 efficiency as a function of the voltage discriminator threshold in the case of normal incidence angle.

IZM with electroplating of SnAg solder bumps.

Measurements on the bump-bonded chip show a working sensor and a good quality of the interconnection at 50 μm pitch. The measured gain and threshold dispersion are compatible with the ones extracted from the front-end chip only. We observe an increase of the noise of around 20%, up to about 76 e-, due to the added capacitive load of the sensor connected. The Superpix0 chip, bump bonded to a high resistivity silicon pixel detector, was also tested on the beam of the Proton Synchrotron (PS) at CERN. The measured efficiency is shown in Fig. 6.30 as a function of the voltage threshold in the discriminator. Efficiencies larger than 99% were obtained for thresholds up to 1/4 of a MIP, corresponding to more than 10 times the pixel noise.

6.12.2.2 The Apsel DNW MAPS series

DNW MAPS in planar CMOS technology Deep N-well MAPS were proposed a few years ago as possible candidates for charged particle tracking applications. The Apsel4D chip is a 4096 element prototype MAPS detector with data-driven readout architecture, implementing twofold sparsification at the pixel level and at the chip periphery. In each elementary cell of the MAPS matrix integrated in the Apsel4D chip, a mixed signal circuit is used to read out and process the charge coming from a deep N-well (DNW) detector. This design approach, relying upon the properties of the triple well structures included in modern CMOS processes, has been described in Section 6.12.1.2. In the so called DNW MAPS is integrated with a relatively large (as compared to standard three transistor MAPS) collecting electrode, featuring a buried N-type layer, with a classical readout chain for time invariant charge amplification and shaping. In the Apsel4D prototype, the elementary MAPS cells feature a 50 μm pitch and a power dissipation of about 30 μW/channel. The block diagram of the pixel analog front-end electronics is shown in Fig. 6.31. The first block of the processing chain, a charge preamplifier, uses a complementary cascode scheme as its forward gain stage, and is responsible for most of the power consumption in the analog section. The feedback capacitor C_F is contin-

uously reset by an NMOS transistor, biased in the deep subthreshold region through the gate voltage V_f. The preamplifier input device, featuring an aspect ratio $W/L = 14\ \mu m/0.25\mu m$ and a drain current of 20 μA, was optimized for a DNW detector about 900 μm^2 in area and with a capacitance C_D of about 300 fF. The charge preamplifier is followed by a CR-RC, bandpass filtering stage, with open loop gain $T(s)$, featuring a programmable peaking time which can be set to 200 or 400 ns. C_1 is a differentiating capacitor at the CR-RC shaper input, while G_m and C_2 are the transconductance and the capacitance in its feedback network. A discriminator is used to compare the processed signal to a global voltage reference V_t, thereby providing hit/no-hit information to the cell digital section. More details on the design of the analog front-end can be found in the literature [56]. A dedicated readout architecture to perform on-chip data sparsification has been implemented in the Apsel4D prototype. The readout logic provides the timestamp information for the hits. The timestamp, which is necessary to identify the event to which the hit belongs, is generated by the bunch-crossing signal. The key requirements in this development are 1) to minimize logical blocks with PMOS inside the active area, thus preserving the collection efficiency, 2) to reduce to a minimum the number of digital lines crossing the sensor area, in particular its dependence on detector size to allow the readout scalability to larger matrices and to reduce the residual crosstalk effects, and 3) to minimize the pixel dead time

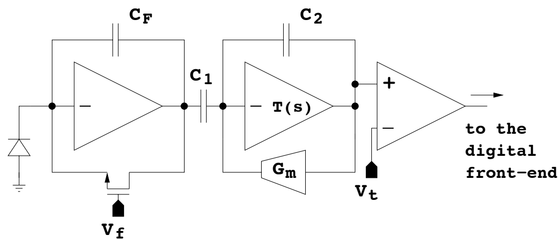

Figure 6.31: block diagram of the analog front-end electronics for the elementary cell of the Apsel4D prototype.

by reading hit pixels out of the matrix as soon as possible. With these criteria a readout logic in the periphery of the matrix has been developed, as schematically shown in Fig 6.32. To minimize the number of digital lines crossing the active area the matrix is organized in MacroPixels (MP) with 4x4 pixels. Each MP has only two private lines for point-to-point connection to the peripheral logic: one line is used to comunicate that the MP has got hits, while the second private line is used to freeze the MP until it has been read out. When the matrix has some hits, the columns containing fired MPs are enabled, one at a time, by vertical lines. Common horizontal lines are shared among pixels in the same row to bring data from the pixels to the periphery, where the association with the proper timestamp is performed before sending the formatted data word to the output bus. The chip has been designed with a mixed mode design approach. While the pixel matrix has a full custom design and layout, the periphery readout architecture has been synthesized in standard cell starting from a VHDL model; automatic place-and-route tools have been used for the layout of the readout logic [51]. The chip has been designed to run with a readout clock up to 100 MHz (20 MHz in test beam), a maximum matrix readout rate of 32 hit pixels/clock cycle and a local buffer of maximum 160 hits to minimize the matrix sweep time. Apsel4D has

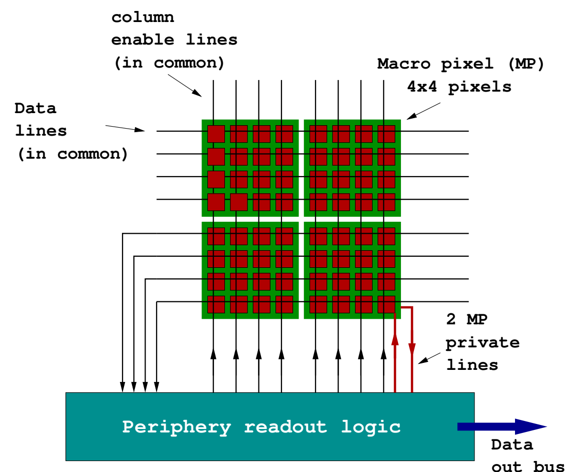

Figure 6.32: schematic concept of the architecture for MAPS matrix readout.

been successfully tested with 12 GeV/c protons at the PS-T9 beam line at CERN [55]. The efficiency of the DNW MAPS as a function of threshold for two devices with different silicon thickness (Chip 22 is 300 μm thick, while Chip 23 is 100 μm thick) has been measured. Figure 6.33 shows the measured hit efficiency, determined as described in a published work [55]. At the lowest thresholds a maximum efficiency

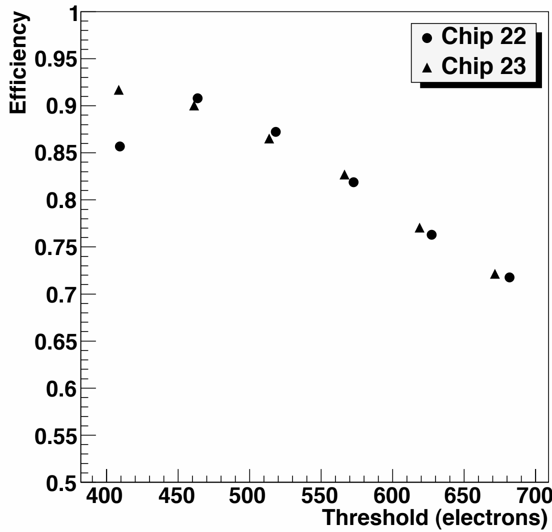

Figure 6.33: efficiency results for two MAPS detectors (the statistical uncertainty on each point is smaller than the size of the plotting symbol).

of approximately 92% and the expected general behavior of decreasing efficiency with increasing threshold can be observed. The noise occupancy for this range of thresholds was found to vary from 2.5×10^{-3} to 1×10^{-6}. The low efficiency observed for Chip 22 at the lowest threshold appears to have been caused by a readout malfunction. Investigations have shown that a small localized area on the detector had very low efficiency, while the rest of the detector behaved normally with good efficiency. Additionally, the efficiency for detecting hits as a function of the track extrapolation point *within a pixel* has been studied. Since the pixel has internal structure, with some areas less sensitive than others, we expect the efficiency to vary as a function of position within the cell. The uncertainty on the track position, including multiple scattering effects is roughly 10 microns, to be compared to the 50 μm pixel dimension. The pixel has been divided into nine square sub-cells of equal area and the hit efficiency within each sub-cell has been measured. The efficiencies thus obtained are "polluted" in some sense due to the migration of tracks among cells. We obtain the true sub-cell efficiencies by unfolding the raw results, taking into account this migration, which we characterize using a simple simulation. The result can be seen in Figure 6.34, where the efficiency measured in each sub-cell is shown. A significant variation in sensitivity within the pixel area can be observed, as expected. In particular, the central region is seen to be virtually 100% efficient, while the upper part of the pixel, especially the upper right-hand sub-cell, shows lower efficiency due to the presence of competitive n-wells. The position of this pixel map relative to the physical pixel is not fixed. This is a consequence of the alignment, which determines the absolute detector position by minimizing track-hit residuals, as described above. If the pixel area is not uniformly efficient, the pixel center as determined by the alignment will correspond to the barycenter of the pixel efficiency map. Thus, it is not possible to overlay Figure 6.34 on a drawing of the pixel layout, without adding additional information, for example a simulation of internal pixel efficiency. The efficiency as a function of position on the MAPS matrix has also been investigated, since disuniformity could indicate inefficiencies caused by the readout. Generally, a uniform efficiency across the area of the MAPS matrix was observed. The intrinsic resolution σ_{hit} for the MAPS devices was measured as already described in a published paper [55]. The expected resolution for cases where the hit consists of a single pixel is given by $50/\sqrt{12} = 14.4$ μm, where 50 microns is the pixel dimension.

DNW MAPS in 3D CMOS technology As already mentioned in Section 6.12.1.2, the DNW monolithic sensors have been designed and fabricated also in the Tezzaron/Globalfoundry

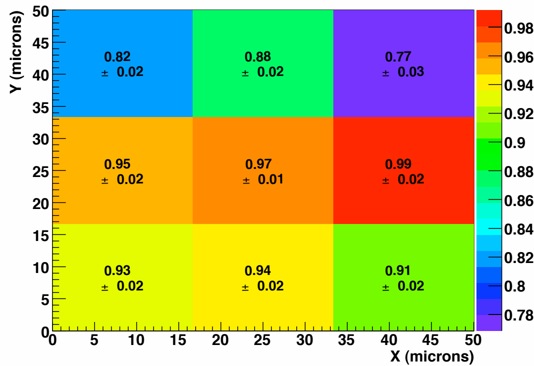

Figure 6.34: hit effiencies measured as a function of position within the pixel (the picture, which is not to scale, represents a single pixel divided into nine sub-cells).

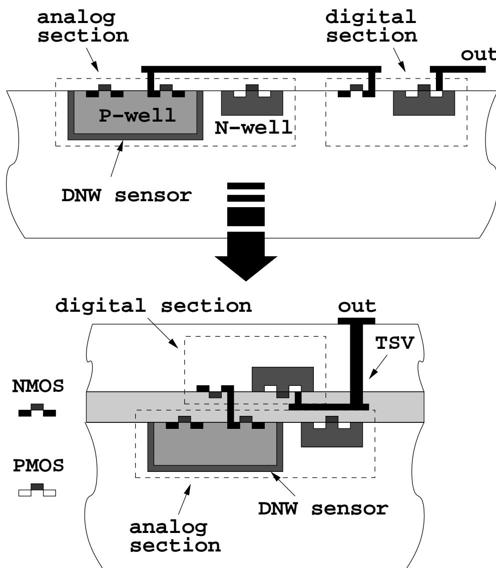

Figure 6.35: cross-sectional view of a DNW CMOS MAPS: from a planar CMOS technology to a 3D process

technology, based on the vertical integration of two 130 nm CMOS layers. The conceptual step from the DNW MAPS in a planar CMOS technology to its vertically integrated version is illustrated in Fig 6.35, showing a cross-sectional view of a 2D MAPS and of its 3D translation. The prototype include two small 3×3 matrices for analog readout and charge collection characterization and a larger one, 8×32 in size, equipped with a digital readout circuit with data sparsification and time stamping features. The pixel pitch is 40 μm. A number of different problems were encountered during fabrication of the first device batch. Among them, the misalignment between the two tiers prevented the analog and digital sections in each pixel cell to communicate to each other [60]. At the time of the TDR writing, other 3D wafers are being processed and devices from the first run are under characterization.

Fig. 6.36 shows the analog front-end channel of the 3D DNW MAPS (quite similar to the analog processor of the SuperPIX0 chip, see Fig. 6.29), simply consisting of a charge preamplifier, whose bandwidth was purposely limited to improve the signal-to-noise ratio (so called shaperless configuration). Equivalent noise charge of between 30 and 40 electrons (in good agreement with circuit simulations) and a charge sensitivity of about 300 mV/fC (a factor of 2 smaller than in simulations) were obtained from prototype characterization. Fig. 6.37 shows the ^{90}Sr spectrum detected by the cluster of 3×3 pixels in a small matrix.

The most probable value of the collected charge is about 100 electrons. Pseudo-3D DNW MAPS (here, the term pseudo-3D refers to devices consisting of just one tier but suitable for 3D integration) have been tested on the PS beam at CERN. Very promising results were

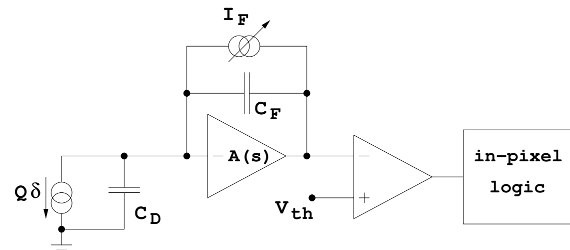

Figure 6.36: block diagram of the analog front-end electronics for the elementary cell of the 3D DNW MAPS of the apsel family.

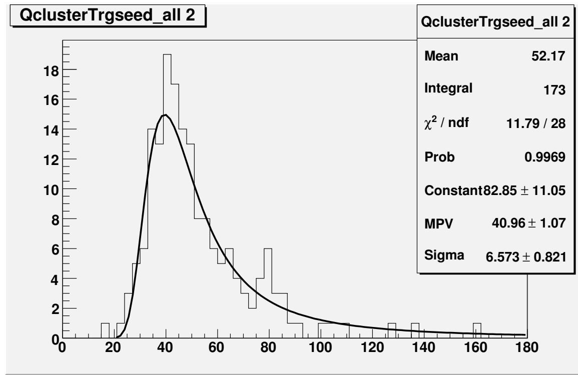

Figure 6.37: spectrum of a ^{90}Sr source detected by a 3×3 matrix of 3D DNW MAPS.

obtained in terms of detection efficiency, as displayed in Fig. 6.38.

6.12.2.3 The Apsel4well quadruple well monolithic sensor

As already mentioned in section 6.12.1.3, a test chip in the INMAPS, 180 nm CMOS technology, called Apsel4well, has been submitted in August 2011. The chip includes four 3×3 matrices

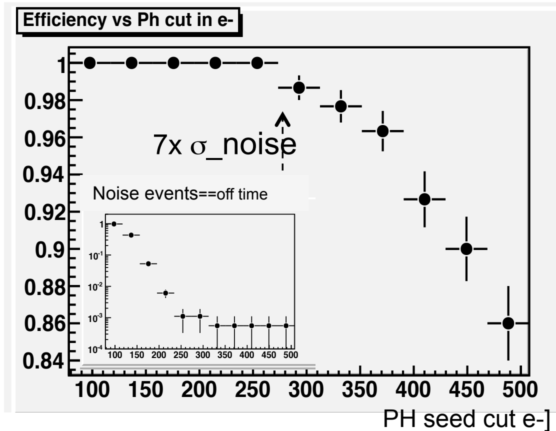

Figure 6.38: Detection efficiency of a pseudo-3D DNW MAPS as a function of the cut on the pulse height of the detected events. The efficiency is 1 up to threshold values of 7 times the pixel noise.

with different number (2 or 4) of the collecting electrodes (each consisting of a 1.5 μm×1.5 μm N-well diffusion), with or without the shielding deep P-well implant, with or without enclosed layout transistors as the input device of the charge preamplifier. The prototype also contains a 32×32 matrix with sparsified digital readout. The test of the first version of the chip, featuring a 5.5 μm thick epitaxial layer with standard resistivity, about 50 Ω·cm) was in progress during the writing of this TDR. Monolithic sensors with a thicker (12 μm) and more resistive (about 1 kΩ·cm) are expected to be out of the foundry by June 2012. Fig. 6.39 shows the analog readout channel of the Apsel4well MAPS. It includes a charge preamplifier, a shaping stage with a current mirror in the feedback network and a two-stage threshold discrim-

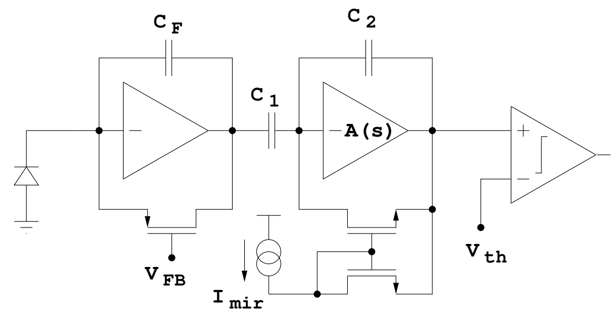

Figure 6.39: block diagram of the analog frontend electronics for the elementary cell of Apsel4well monolithic sensor.

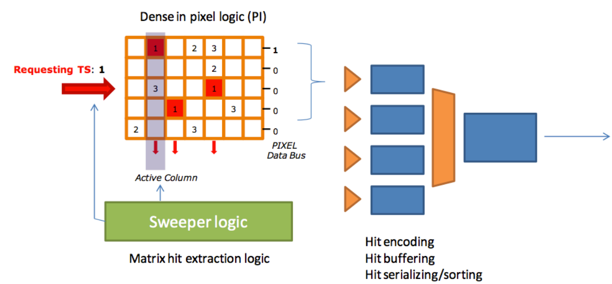

Figure 6.40: conceptual view of the digital readout architecture of the Apsel4well chip operated in the triggered mode.

inator. Several digital blocks are also integrated in each individual pixel element for data sparsification and time stamping purposes. Time from a peripheral Gray counter is distributed to each pixel in the matrix and is latched to a time stamp register upon arrival of a hit. When a timestamp request is sent to the matrix, a pixel FastOR signal activates if the latched timestamp is the same as the requestd one. The columns with an active FastOR signal are enabled and read out in a sequence; 1 clock cycle per column is needed. A conceptual view of the digital readout architecture is shown in Fig. 6.40. Readout circuits can be operated either in triggered or in data-push mode. They take care of encoding, buffering and serializing/sorting the hits retrieved from the sensor matrix. In order to achieve the remarkably high readout frequency set by the SuperB experiment, the architecture can be subdivided in a number of modules, each serving a submatrix. This choice improves the scalability features of the readout section and makes it suitable for experiment scale detectors. Efficiency well in excess of 99% have been obtained in Monte Carlo simulations with hit rates of 100 MHz/cm^2. Fig. 6.41 shows the signal at the shaper output as a response to an input charge signal with varying amplitude. Figures provided by the preliminary experimental characterization of the analog section are very close to simulation data, with a gain of about 960 mV/fC and an equivalent noise charge of about 30 electrons. The plot in Fig. 6.42 represents the collected charge in a Apsel4well pixel (5 μm epitaxial layer thickness, standard resistivity) illuminated with an infrared laser source. The position of the collecting electrodes is easily detectable.

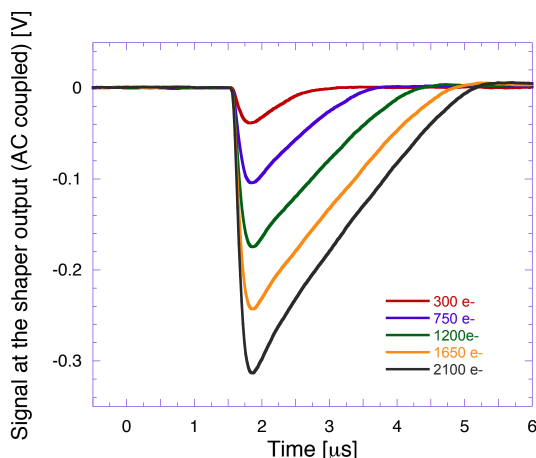

Figure 6.41: signal at the shaper output as a response to an input charge signal with varying amplitude in an Apsel4well sensor.

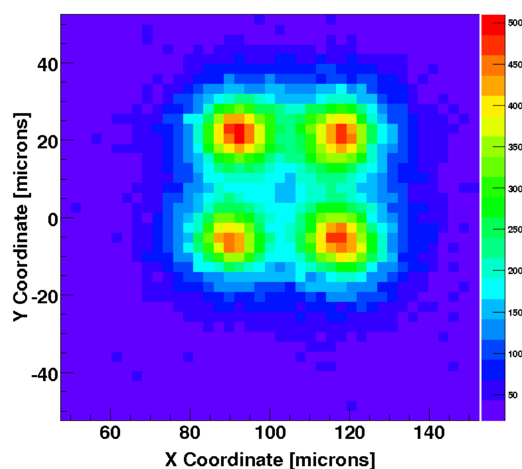

Figure 6.42: collected charge in a Apsel4well pixel illuminated with an infrared laser source.

6.12.3 Radiation tolerance

Hybrid pixels. The high degree of radiation tolerance of modern CMOS technologies, coming as a byproduct of the aggressive scaling down of device minimum feature size, is having a beneficial impact in high energy physics (HEP) applications. Beginning with the 130 nm CMOS processes, which entered the sub-3 nm gate oxide thickness regime, direct tunneling contribution to the gate current has assumed a significant role as compared to trap assisted mechanisms [61]. This may account for the very high degree of radiation hardness featured by devices belonging to the most recent technology nodes, which might benefit

from relatively fast annealing of holes trapped in the ultrathin gate oxides. Tolerance to a few hundred of Mrad(SiO_2) has been recently proven in front-end circuits for hybrid pixel detectors [62]. Charge trapping in the thicker shallow trench isolation (STI) oxides is considered as the main residual damage mechanism in 130 nm N-channel MOSFETs exposed to ionizing radiation [63, 64], especially in narrow channel transistors [65]. Ionizing radiation was found to affect also the 90 nm and 65 nm CMOS nodes, although to an ever slighter extent, likely due to a decrease in the substrate doping concentration and/or in the STI thickness. As far a as analog front-end design is concerned, ionizing radiation damage mainly results in an increase in low frequency noise, which is more significant in multifinger devices operated at a small current density. This might be a concern in the case of the front-end electronics for hybrid pixel detectors, where the input device of the charge preamplifier is operated at drain currents in the few μA range owing to low power constraints. However, at short peaking times, typically below 100 ns, the effects of the increase in low frequency noise on the readout channel performance is negligible. Also, use of enclosed layout techniques for the design of the preamplifier input transistor (and of devices in other critical parts of the front-end) minimizes the device sensitivity to radiation [66]. For this purpose, Fig. 6.43 shows the noise voltage spectrum for a 130 nm NMOS transistor with enclosed layout, featuring no significant changes after irradiation with a 100 Mrad(SiO_2) total ionizing dose. On the other hand, CMOS technologies are virtually insensitive to bulk damage, since MOSFET transistor operation is based on the drift of majority carriers in a surface channel.

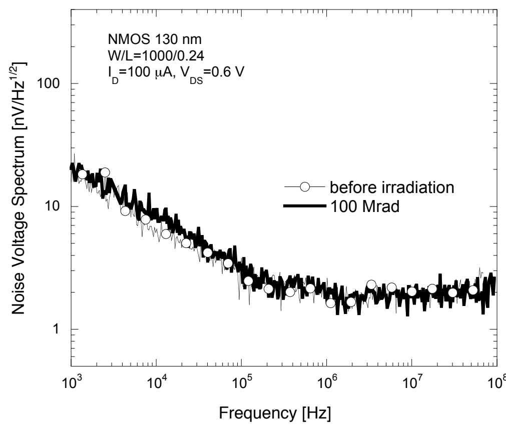

Figure 6.43: noise voltage spectrum for a 130 nm NMOS device with enclosed layout.

DNW CMOS MAPS DNW MAPS have been thoroughly characterized from the standpoint of radiation hardness to evaluate their limitations in harsh radiation environments. In particular, the effects of ionizing radiation, with total doses of about 10 Mrad(SiO_2), have been investigated by exposing DNW MAPS sensors to a ^{60}Co source [67]. In that case, some performance degradation was detected in the noise and gain of the front-end electronics and in the sensor leakage current, while no significant change was observed as far as the charge collection properties are concerned. Fig. 6.44 shows the equivalent noise charge as a function of the absorbed dose and after the annealing cycle for a DNW monolithic sensor. The significant change can be ascribed to the increase in the flicker noise of the preamplifier input device as a consequence of parasitic lateral transistors being turned on by positive charge buildup in the shallow trench isolation oxides and contributing to the overall noise. Use of an enclosed layout approach is expected to significantly reduce the effect of ionizing radiation. Fig. 6.45 shows event count rate for a DNW monolithic sensor exposed to a ^{55}Fe source before irradiation, after exposure to γ-rays and after the annealing cycle. As the absorbed dose increases, the 5.9 keV peak gets broader as a consequence of the noise increase (in fair agreement with data in Fig. 6.44. At the same time, the peak is shifted towards lower amplitude values, as a result of a decrease in the front-end charge sensitivity also due to charge build up in the STI of some critical devices. DNW MAPS of the same kind have also been irradiated with neutrons from a Triga MARK II nuclear reactor to test bulk damage effects [68]. The final fluence, 6.7×10^{12} 1

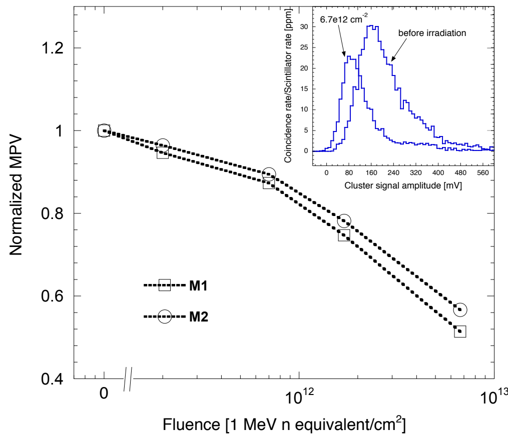

Figure 6.46: most probable value (MPV) of the ^{90}Sr spectra (shown in the inset for one of the tested chips before irradiation and after exposure to a 6.7×10^{12} cm^{-2} neutron fluence) normalized to the pre-irradiation value as a function of the fluence for DNW MAPS with different sensor layout.

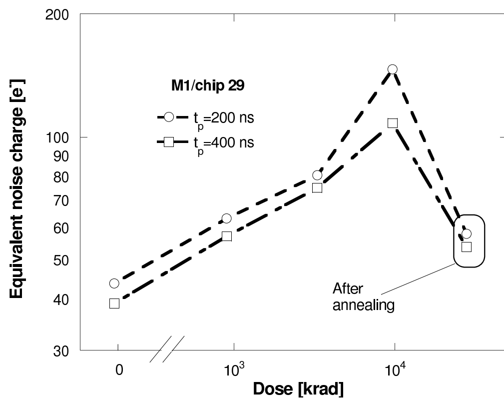

Figure 6.44: equivalent noise charge as a function of the absorbed dose and after the annealing cycle for DNW monolithic sensor. ENC is plotted for the two available peaking times.

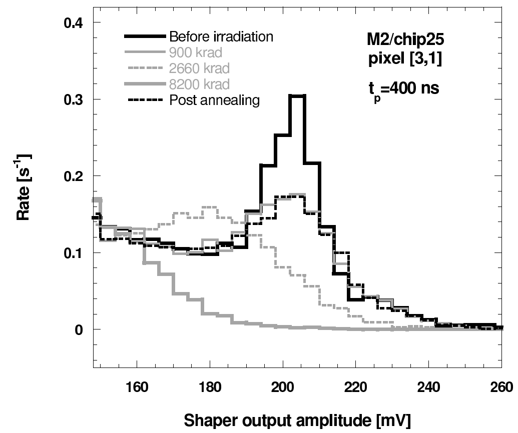

Figure 6.45: event count rate for a DNW monolithic sensor exposed to a ^{55}Fe source before irradiation, after exposure to γ-rays and after the annealing cycle.

MeV neutron equivalent/cm^2, was reached after a few, intermediate steps. The devices under test (DUT) were characterized by means of several different techniques, including charge injection at the front-end input through an external pulser, sensor stimulation with an infrared laser and spectral measurements with ^{55}Fe and ^{90}Sr radioactive sources. Neutron irradiation was found to have no sizable effects on the front-end electronics performance. This can be reasonably expected from CMOS devices, whose operation is based on the drift of majority carriers in a surface channel, resulting in a high degree of tolerance to bulk damage. Exposure to neutrons was instead found to affect mainly the charge collection properties of the sensors with a reduction in the order of 50% at the maximum integrated fluence. Fig. 6.46 shows the most probable value (MPV) of the ^{90}Sr spectra normalized to the pre-irradiation value as a function of the fluence for DNW MAPS with different sensor layout. A substantial decrease can be observed, to be ascribed to a degradation in the minority carrier lifetime. A higher degree of tolerance was instead demonstrated in monolithic sensors with high resisitivity (1 kΩ cm) epitaxial layer [70]. Actually, doping concentration plays a role in determining the equilibrium Fermi level, which in turn influences the effectiveness of neutron-induced defects as recombination centers [69].

6.13 Services, Utilities and E.S. & H issues - 4 pages

6.13.1 Service and Utilities

- Data and control lines
- Power
- Cooling water
- Dry air or nitrogen

6.13.2 ES&H Issue

Bibliography

[1] BABAR Collaboration (D. Boutigny et al.), *BaBar technical design report*. SLAC-R-0457.

[2] C. Bozzi *et al.* [BABAR Collaboration], "The design and construction of the BaBar silicon vertex tracker," Nucl. Instrum. Meth. A **447** (2000) 15.

[3] J. Walsh, *Performance with different SVT configurations*, http://agenda.infn.it/getFile.py/access?contribId=132&sessionId=19&resId=0&materialId=slides&confId=1165.

[4] B. Aubert *et al.* [BABAR Collaboration], "The BaBar detector," Nucl. Instrum. Meth. A **479**, 1 (2002).

[5] O. Long, BaBar Note #499,*An alternative algorithm for stand-alone SVT pattern recognition*, July 8, 1999

[6] N. Neri, *Tracking Performance with the SVT baseline configuration*, http://agenda.infn.it/getFile.py/access?contribId=162&sessionId=25&resId=0&materialId=slides&confId=1161.

[7] M. Rama , *Performance studies with different SVT and DCH configurations*, http://agenda.infn.it/getFile.py/access?contribId=161&sessionId=25&resId=2&materialId=slides&confId=1161.

[8] G. Simi, $B^0 \to K^0_S\pi^0$ *vs. SVT radius*, http://agenda.infn.it/getFile.py/access?contribId=164&sessionId=25&resId=3&materialId=slides&confId=1161.

[9] R. Andreassen, *Progress with charm mixing measurements at the 4S*, http://agenda.infn.it/materialDisplay.py?contribId=301&sessionId=34&materialId=slides&confId=1742.

[10] BaBar Analysis Document #707, *Final Report of the SVT Long Term Task Force*. February 24, 2004.

[11] I. Ripp-Baudot, *Update on activities in Strasbourg & tracking in high occupancy*, http://agenda.infn.it/getFile.py/access?contribId=63&sessionId=2&resId=2&materialId=slides&confId=4880.

[12] B. Schumm, BaBar Note #126, dE/dx *identification with a five layer silicon tracker*. February 15, 1994.

[13] Alexandre V. Telnov, BaBar Analysis Document #1500, *Detailed Track-Level* dE/dx *Calibration for the BABAR Drift Chamber and Silicon Vertex Tracker*. July 30, 2007.

[14] *FastSim* program, available online at: http://www.pi.infn.it/SuperB.

[15] M. Bona *et al.*, *SuperB: A High-Luminosity Heavy Flavour Factory. Conceptual Design Report*, arXiv:0709.0451v2 [hep-ex], INFN/AE-07/2, SLAC-R-856, LAL 07-15, also available at http://www.pi.infn.it/SuperB/CDR.

[16] G. Rizzo et al., "Recent Development on CMOS MAPS for the SuperB Silicon Vertex Tracker", *Proceedings of the 12th Pisa Meeting on Advanced Detectors, La Biodola, Isola dElba, Italy 2026 May 2012 to be published in Nucl. Instrum. Meth.*

[17] F. Giorgi et al., "The front-end chip of the SuperB SVT detector", *Proceedings of the 12th Pisa Meeting on Advanced Detectors, La Biodola, Isola dElba, Italy 2026 May 2012 to be published in Nucl. Instrum. Meth.*

[18] S. Bettarini et al., "The SLIM5 low mass silicon tracker demonstrator" *Nucl. Instrum. Meth. A* **623** *(2010) 942.*

[19] SLIM5 Collaboration - Silicon detectors with Low Interaction with Material, http://www.pi.infn.it/slim5/

[20] G. Rizzo for the SLIM5 Collaboration., "Development of Deep N-Well MAPS in a 130 nm CMOS Technology and Beam Test Results on a 4k-Pixel Matrix with Digital Sparsified Readout"', *2008 IEEE Nuclear Science Symposium, Dresden, Germany, 19-25 October, 2008*

[21] A. Gabrielli for the SLIM5 Collaboration, "Development of a triple well CMOS MAPS device with in-pixel signal processing and sparsified readout capability" *Nucl. Instrum. Meth. A* **581** *(2007) 303.*

[22] A. Gabrielli et al., "High efficiency readout circuits for large matrices of pixels" *Nucl. Instrum. Meth. A* **658** *(2011) 141.*

[23] F. Giorgi et al., "2D and 3D Thin Pixel Technologies for the Layer0 of the SuperB Silicon Vertex Tracker" *2011 IEEE Nuclear Science Symposium, Valencia, Spain 23-29 October, 2011*

[24] E. Paoloni et al., "Beam test results of different configurations of deep N-well MAPS matrices featuring in pixel full signal processing" *Nucl. Instrum. Meth. A (2010),doi:10.1016/j.nima.2010.06.325*

[25] L. Ratti et al. "Front-End Performance and Charge Collection Properties of Heavily Irradiated DNW MAPS" *IEEE Trans. Nucl. Sci. NS-57 (4) (2010) 1781*

[26] S. Zucca et al. "Characterization of bulk damage in CMOS MAPS with deep N-well collecting electrode" *IEEE Trans. Nucl. Sci. NS-PP (99) (2012) 1*

[27] Ray Yarema, et. al., 3D IC Pixel Electronics-the Next Challenge *TWEPP-08, CERN-2008-008, pp. 183-187, December 10, 2008*

[28] VIPIX Collaboration - Vertically Integrated PIXels, http://eil.unipv.it/vipix/

[29] G. Rizzo et al., "Thin Pixel Development for the SuperB Silicon Vertex Tracker" *Nucl. Instrum. Meth. A* **650** *(2011) 169.*

[30] F. Bosi et al., "Light prototype support using micro-channel technology as high efficiency system for silicon pixel detector cooling" *Nucl. Instrum. Meth. A* **650** *(2011) 213.*

[31] F. Bosi et al., "The micro-cooled light support of the pixel modules for the Super-B experiment", *Proceedings of the 12th Pisa Meeting on Advanced Detectors, La Biodola, Isola dElba, Italy 2026 May 2012, to be published in Nucl. Instrum. Meth.*

[32] M Boscardin et al., "Silicon buried channels for Pixel Detector Cooling", *Proceedings of the 12th Pisa Meeting on Advanced Detectors, La Biodola, Isola dElba, Italy 2026 May 2012, to be published in Nucl. Instrum. Meth.*

[33] K. Nakamura *et al.* [Particle Data Group Collaboration], J. Phys. G G **37**, 075021 (2010).

[34] V. Re *et al.*, IEEE Trans. Nucl. Sci. **53**, 2470 (2006).

[35] SLIM5 Collaboration, *Silicon detectors with Low Interaction with Material*, http://www.pi.infn.it/slim5/.

[36] G. Rizzo for the SLIM5 Collaboration, *Development of Deep N-Well MAPS in a 130*nm *CMOS Technology and Beam Test Results on a 4k-Pixel Matrix with Digital Sparsified Readout*, 2008 IEEE Nuclear Science Symposium Conference Record, Dresden, Germany, 19-25 October, 2008.

[37] A. Gabrielli for the SLIM5 Collaboration, *Development of a triple well CMOS MAPS device with in-pixel signal processing and sparsified readout capability*,Nucl. Instrum. Methods Phys. Res., Sect. A **581**, 303 (2007).

[38] M. Villa for the SLIM5 Collaboration, *Beam-Test Results of 4k pixel CMOS MAPS and High Resistivity Striplet Detectors equipped with digital sparsified readout in the Slim5 Low Mass Silicon Demonstrator*, Nucl. Instrum. Methods Phys. Res., Sect. A (2010) doi:10.1016/j.nima.2009.10.035

[39] E.Paoloni for the VIPIX collaboration, *Beam Test Results of Different Configurations of Deep N-well MAPS Matrices Featuring in Pixel Full Signal Processing*, Proceedings of the XII Conference on Instrumentation, Vienna 2010. To be published in Nucl. Instrum. Methods Phys. Res., Sect. A.

[40] I. PericĹ. Blanquart, G. Comes, P. Denes, K. Einsweiler, P. Fischer et al., *The FEI3 readout chip for the ATLAS pixel detector*, Nucl. Instrum. and Meth., vol. A565, pp. 178-187, 2006.

[41] P. Reiner, *The ATLAS pixel detector*, Nucl. Instrum. and Meth., vol. A579, pp. 664-668, 2007.

[42] D. Bortoletto, *The CMS pixel system*, Nucl. Instrum. and Meth., vol. A636, pp. 559-674, 2007.

[43] A. Kluge, G. Anelli, F. Antinori, A. Badala, A. Boccardi, G. E. Bruno et al., *The ALICE Silicon Pixel Detector: Electronics System Integration*, 2005 IEEE Nuclear Science Symposium Conference Record, pp. 761-764.

[44] M. Garcia-Sciveres, D. Arutinov, M. Barbero, R. Beccherle, S. Dube, D. Elledge et al., *The FE-I4 pixel readout integrated circuit*, Nucl. Instrum. and Meth., vol. A636, pp. S155-S159, 2011.

[45] F. Hügging, *The ATLAS Pixel Insertable B-layer (IBL)*, Nucl. Instrum. and Meth., vol. A650, pp. 45-49, 2011.

[46] C. Favaro, *A new CMS pixel detector for the LHC luminosity upgrade* Nucl. Instrum. and Meth., vol. A658, pp. 41-45, 2011.

[47] *Handbook of 3D Integration: Technology and Applications of 3D Integrated Circuits*. Edited by P. Garrou, C. Bower and P. Ramm. Wiley-VCH, Weinheim, 2008.

[48] A. Klumpp, R. Merkel, P. Ramm, J. Weber, R. Wieland, *Vertical System Integration by Using Inter-Chip Vias and Solid-Liquid Interdiffusion Bonding*, Jpn. J. Appl. Phys. vol. 43, pp. L829-L830, 2004.

[49] R.S. Patti, *Three-Dimensional Integrated Circuits and the Future of System-on-Chip Designs*, Proc. IEEE, vol. 94, no. 6, pp. 1214-1224, Jun. 2006.

[50] Y. Degerli, M. Besanon, A. Besson, G. Claus, G. Deptuch, W. Dulinski, et al., *Performance of a Fast Binary Readout CMOS Active Pixel Sensor Chip Designed for Charged Particle Detection*, IEEE Trans. Nucl. Sci., vol. 53, no. 6, pp. 3949-3955, Dec. 2006.

[51] A. Gabrielli, G. Batignani, S. Bettarini, F. Bosi, G. Calderini, R. Cenci et al., *Proposal of a Data Sparsification Unit for a Mixed-Mode MAPS Detector*, 2007 IEEE Nuclear Science Symposium Conference Record, vol. 2, pp. 1471-1473, Oct. 26 2007-Nov. 3 2007.

[52] M. Stanitzki, J.A. Ballin, J.P. Crooks, P.D. Dauncey, A.M.M. Magnan, Y. Mikami et al., *A tera-pixel calorimeter for the ILC*, 2007 IEEE Nuclear Science Symposium Conference Record, vol. 1, pp. 254-258.

[53] L. Ratti et al., "Design of Time Invariant Analog Front-End Circuits for Deep N-Well CMOS MAPS", *IEEE Trans. Nucl. Sci.*, vol. 56, no. 4, pp. 2360-2373, Aug. 2009.

[54] G. Traversi, "Charge Signal Processors in a 130 nm CMOS Technology for the Sparse Readout of Small Pitch Monolithic and Hybrid Pixel Sensors", *IEEE Trans. Nucl. Sci.*, vol. 58, no. 5, pp.2391-2400, Oct. 2011.

[55] S. Bettarini, L. Ratti, G. Rizzo, M. Villa, L. Vitale, J. Walsh et al., *The SLIM5 low mass silicon tracker demonstrator*, Nucl. Instrum. and Meth., vol. A623, pp. 942-953, 2010.

[56] L. Ratti, *Continuous Time-Charge Amplification and Shaping in CMOS Monolithic Sensors for Particle Tracking*, *IEEE Trans. Nucl. Sci.*, vol. 53, no. 6, pp. 3918-3928, Dec. 2006.

[57] G.Casarosa, C. Avanzini, G. Batignani, S. Bettarini, F. Bosi, M. Ceccanti et al., *Thin Pixel Development for the Layer0 of the SuperB Silicon Vertex Tracker*, 2010 IEEE Nuclear Science Symposium Conference Record, pp. 1901-1905.

[58] L. Ratti, L. Gaioni, M. Manghisoni, V. Re, G. Traversi, *Vertically integrated deep N-well CMOS MAPS with sparsification and time stamping capabilities for thin charged particle trackers*, Nucl. Instrum. and Meth., vol. A624, pp. 379-386, 2010.

[59] http://3dic.fnal.gov.

[60] L. Ratti, L. Gaioni, A. Manazza, M. Manghisoni, V. Re, G. Traversi, *First results from the characterization of a three-dimensional deep N-well MAPS prototype for vertexing applications*, Nucl. Instrum. and Meth., DOI: 10.1016/j.nima.2012.03.021.

[61] A. Ghetti, E. Sangiorgi, J. Bude, T.W. Sorsch, G. Weber, *Tunneling into Interface States as Reliability Monitor for Ultrathin Oxides*, IEEE Trans. El. Dev., vol. 47, no. 12, pp. 2358-2365, Dec. 2000.

[62] M. Garcia-Sciveres, D. Arutinov, M. Barbero, R. Beccherle, S. Dube, D. Elledge et al., *The FE-I4 pixel readout integrated circuit*, Nucl. Instrum. and Meth., vol. A636, pp. S155-S159, 2011.

[63] V. Re, M. Manghisoni, L. Ratti, V. Speziali, G. Traversi, *Total Ionizing Dose Effects on the Noise Performances of a 0.13 μm CMOS Technology*, IEEE Trans. Nucl. Sci., vol. 53, no. 3, pp. 1599-1606, Jun. 2006.

[64] L. Ratti, L. Gaioni, M. Manghisoni, G. Traversi, D. Pantano, *Investigating Degradation Mechanisms in 130 nm and 90 nm Commercial CMOS Technologies Under Extreme Radiation Conditions*, IEEE Trans. Nucl. Sci., vol. 56, no. 4, pp. 1992-2000, Aug. 2008.

[65] F. Faccio, G. Cervelli, *Radiation-Induced Edge Effects in Deep Submicron CMOS Transistors*, IEEE Trans. Nucl. Sci., vol. 52, no. 6, pp. 2413-2420, Dec. 2005.

[66] W.J. Snoeys, T.A.P. Gutierrez, G. Anelli, *A new NMOS layout structure for radiation tolerance*, IEEE Trans. Nucl. Sci., vol. 49, no. 4, pp. 1829-1833, Aug. 2002.

[67] L. Ratti, M. Manghisoni, V. Re, G. Traversi, S. Zucca, S. Bettarini, F. Morsani, G. Rizzo, *Front-End Performance and Charge Collection Properties of Heavily Irradiated DNW MAPS*, IEEE Trans. Nucl. Sci., vol. 57, no. 4, pp. 1781-1789, Aug. 2010.

[68] S. Zucca, L. Ratti, G. Traversi, S. Bettarini, F. Morsani, G. Rizzo, L. Bosisio, I. Rashevskaya, V. Cindro, *Characterization of bulk damage in CMOS MAPS with deep N-well collecting electrode*, Proceedings of the 12th European Conference on Radiation and Its Effects on Components and Systems (RADECS), 2011, pp. 297-304.

[69] G.C. Messenger, *A summary review of displacement damage from high energy radiation in silicon semiconductors and semiconductor devices*, IEEE Trans. Nucl. Sci., vol. 39, no. 3, pp. 468-473, Jun. 1992.

[70] M. Deveaux, J. Baudot, N. Chon-Sen, G. Claus, C. Colledani, R. De Masi et al., *Radiation tolerance of a column parallel CMOS sensor with high resistivity epitaxial layer*, 2011 JINST 6 C02004, DOI: 10.1088/1748-022/6/02/C02004.

[71] R. Yarema, *3D circuit integration for vertex and other detectors*, Proceedings 16th International Workshop on Vertex Detectors (VERTEX2007), Lake Placid (NY, USA), September 23 - 28, 2007, Proceedings of Science PoS(Vertex 2007)017.

[72] F.Bosi and M. Massa, *Development and Experimental Characterization of Prototypes for Low Material Budget Support Structure and Cooling of Silicon Pixel Detectors, Based on Microchannel Technology*, Nucl. Instrum. Methods Phys. Res., Sect. A (2010) doi:10.1016/j.nima.2009.10.138

[73] J. A. Ballin *et al.*, *Monolithic Active Pixel Sensors (MAPS) in a quadruple well technology for nearly 100% fill factor and full CMOS pixels*, Sensors **8**, 5336 (2008).

[74] N. K. Watson *et al.*, *A MAPS-based readout of an electromagnetic calorimeter for the ILC*, J. Phys. Conf. Ser. **110**, 092035 (2008).

[75] J. P. Crooks *et al.*, *A monolithic active pixel sensor for a tera-pixel ECAL at the ILC*, CERN-2008-008.